FACULTY
OF MATHEMATICS
AND PHYSICS
Charles University

DOCTORAL THESIS

Vladimir Pushkarev

Ultrafast photoconductivity and charge carrier transport in semiconductor nanostructures: a study by terahertz spectroscopy

Institute of Physics of the Czech Academy of Sciences

Supervisor of the doctoral thesis:	doc. RNDr. Petr Kužel, Ph.D.
Study programme:	Physics
Specialization:	Physics of Condensed Matter and Materials Research

Prague 2023

I declare that I carried out this master thesis independently, and only with the cited sources, literature and other professional sources. It has not been used to obtain another or the same degree.

I understand that my work relates to the rights and obligations under the Act No. 121/2000 Sb., the Copyright Act, as amended, in particular the fact that the Charles University has the right to conclude a license agreement on the use of this work as a school work pursuant to Section 60 paragraph 1 of the Copyright Act.

Prague, 7 January 2023 …….

Vladimir Pushkarev

Acknowledgements

There are a great many to whom I owe my thanks for their help and support in the preparation of this work.

Words cannot express my gratitude to my supervisor, Petr Kužel, for his professional guidance, encouragement and patience during my Ph.D. research. I am deeply indebted to him for introducing me to THz spectroscopy and sharing his knowledge and expertise in this field. He has always been there for me with support and advice. I deeply appreciate his editing, comments and discussions on this manuscript.

I also could not have undertaken this journey without my colleague and advisor, Hynek Němec, who generously provided me with experimental assistance and invaluable insights into charge transport in various materials. His great ideas have helped me to overcome many obstacles in interpretation of experimental data.

This work would not be possible without the cooperation with Tomáš Ostatnický, who provided the cutting-edge quantum mechanical calculations of electron mobility which he developed. His participation in the research played a decisive role in analysis of photoconductivity spectra.

I thank Daniel Hiller and Sebastian Gutsch for preparation of the silicon nanocrystal superlattices and Vlastimil Jurka, Vít Novák, and Jan Fábry, for a custom-built sample with GaAs nanobars. Special thanks go to Hartmut Roskos, Mark Thomson and Meng Fanqi for an access to multi-THz – mid-infrared pulsed spectroscopy and their professional experimental assistance. I would like to acknowledge Veronika Goian, for her assistance in steady-state infrared measurements and Fedir Borodavka, for sharing his experience in atomic force microscopy.

I am very grateful to Jiří Hlinka – the head of the Department of Dielectrics (Institute of Physics) – and all my colleagues at the Department for a friendly and helpful working environment.

Finally, my unbounded gratitude goes to my family for their constant support and inspiration.

Title: Ultrafast photoconductivity and charge carrier transport in semiconductor nanostructures: a study by terahertz spectroscopy

Author: Vladimir Pushkarev

Institute: Institute of Physics of the Czech Academy of Sciences

Supervisor of the doctoral thesis: doc. RNDr. Petr Kužel, Ph.D.

Abstract: The thesis is devoted to a study of charge transport in nanostructured systems by means of time-resolved terahertz spectroscopy. We address various aspects of electron confinement in such systems, and the role of depolarization fields on the effective photoconductive response of samples. Accurate evaluation of localized carrier properties has been achieved using quantum mechanical calculations of the mobility. Theoretical interpretation of the terahertz conductivity spectra is based on the solution of the wave equation for the terahertz wave in inhomogeneous photoexcited media described in terms of VBD effective medium model developed in our laboratory. This approach is employed for investigation of the terahertz photoconductivity in two types of nanomaterials: superlattices of Si nanocrystals prepared by thermal decomposition of SiO_x layers and lithographically prepared GaAs nanobars. Experimental spectra were measured at 300 and 20 K and for a wide range of photocarrier densities. A careful analysis of electron transport in Si nanocrystals showed a broad distribution of the nanocrystal sizes and its dependence on the silicon content. These results are also supported by time-resolved measurements in the far- and mid-infrared range. The investigation of the GaAs nanobars sample revealed a band bending close to the nanobar surface that has been confirmed using time-resolved terahertz near-field experiment.

Keywords: time-resolved terahertz spectroscopy, photoconductivity, charge transport and confinement, depolarization fields, effective medium theory.

Contents

Introduction

During the last decade, evolution of electronic and optoelectronic devices has been closely related to the progress in nanotechnology; in particular, semiconductor-based technology. Precise control of the component properties is often required at practically all steps of the device manufacturing. Despite a considerable number of existing experimental techniques and theoretical models aimed to characterization of nanomaterial structure, there is still a lack of understanding of the material electronic and optoelectronic properties on ultrafast timescale at the microscopic level, which is where the charge motion may play a decisive role.

In the case of bulk homogeneous semiconductors, the investigation of charge carriers transport inside a material is usually quite straightforward and does not require sophisticated experimental techniques and theoretical models. However, local properties of inhomogeneous materials and, in particular, of nanostructures might differ significantly from the apparent macroscopic ones, causing challenges in both experimental characterization and its theoretical interpretation. Detection of the electron transport in a single nanoparticle by means of the conventional DC electrical methods demands deposition of the electrical contacts on the nanometer scale, which is not an easy task; at the same time, these contacts may disturb the electron confinement and significantly influence its conductive response. On the other hand, results of DC measurements of long-range inter-nanoparticle transport in composite samples depend on the dielectric material connecting the nanoparticles. The optical (spectroscopic) methods enable contactless measurements, e.g., the sample is placed in the path of the electromagnetic radiation. However, analysis of the material spectral response is firmly limited by the corresponding frequency range: depending on the frequency-dependent skin effect and dimension of the studied sample, its characteristic dimensions can be sometimes considered as infinite for high frequencies, whereas, for the radiation wavelengths that are significantly larger than the dimensions of the structures, electromagnetic field may be treated as constant within a single nano-element. In both DC and optical measurements of the long-range charge transport, suitable dielectric mixing rules (effective medium theory) must be applied to retrieve the information of interest (which is basically the properties of the short-range transport) from the raw data. In order to perform such analysis, it is quite advantageous to have a broadband response available so as to select an appropriate effective medium model.

The local conductivity on the nanometer scale can be measured using conductive atomic force microscopy. Namely, the presence and absence of the percolation pathways through the sample thickness can be proved by this method [1]. However, it is difficult to apply this technique to some samples as for example layered nanocrystalline structures with insulating interlayers, which are extensively discussed in this manuscript. Based on the above, terahertz (THz) spectroscopy appears as a powerful tool for a contactless analysis of local features of the carrier motion in various ensembles of nanocrystalline networks. THz radiation, sensitive to the presence of the conduction band electrons, has been used to this purpose both in near-field and in far-field configurations. The former approach operates in a near-field scattering mode, which is ensured by an AFM tip acting as a local scatterer of the THz radiation

close to the probed nanostructure. It is possible to plot the time-dependent photoconductivity contrasts at the surface of a single nanocrystal or nanowire; however, in the current state-of-the-art, the technique does not allow to evaluate quantitatively broadband local conductivity spectra. Nevertheless, it opens a new way of characterization of a single nanowire or a single molecule transistors and similar electronic devices. The latter (far-field) method enables one to measure spectra of the complex dielectric response function of the composite material, i.e. averaged over a macroscopic ensemble of nano-objects. This has clear feedback to the applications: ensembles of nano-objects are used in the majority of electronic applications and the cheap fabrication methods usually do not offer the possibility to achieve the uniformity in the nanocrystal sizes and shapes. The THz photoconductivity measurements then combine several advantages of conventional electrical and optical methods, namely (1) experiments are done without electrical contacts, (2) measurements are phase-sensitive, i.e., both real and imaginary part of the conductivity are determined simultaneously, (3) the time resolution of the spectra is better than 1 ps.

In the *THz science and technology* group at the *Institute of Physics of the Czech Academy of Sciences* we seek for highly reliable fabrication methods providing nanoelements with well-defined monodisperse properties and crystal structure required for a more efficient advancement of the research. While chemical routes are cheap and suitable for mass production of a great variety of nanostructures, they usually lead to a wide spread of physical properties of nanoparticles including their size, shape, orientation, electrical conductivity, and connectivity at interfaces. Thus, under such conditions, it is usually very difficult to gain in-depth understanding of nanoscale conduction properties since some phenomena may be overlooked due to averaging of the response over the disordered ensemble [1,2]. For better control of the nanocrystal size, we used samples prepared by a superlattice approach to form layered silicon nanocrystal networks [3]; these are studied in chapter 4. However, as it will be shown latter, even with this preparation approach a considerable distribution of the properties still exist [4] that hinders detailed understanding of fine effects in the charge carrier mobility. Therefore, still moving towards regular sample properties, we combined the molecular beam epitaxy technique with electron beam lithography for the preparation of uniform GaAs nanobars introduced in chapter 5. Unique properties of the sample including precise control of the nanostructure geometry and alignment allowed an in-depth understanding of the carrier motion within a single nanostructure providing an access to band bending phenomenon close to the nanobar surfaces [5].

This work includes my original experimental results and also theoretical models developed or revised in our group; I applied these models to interpret the data. The structure of the thesis is the following: in chapter 1 we describe relevant spectral range and its applications; theoretical models of the charge carrier transport are presented in chapter 2. Chapter 3 describes in details the experimental setups employed in this work. Our study of the photoinduced electron mobility in superlattices of silicon nanocrystal networks in the THz and ultra-broad THz – mid-infrared frequency ranges is presented in chapter 4. Chapter 5 is devoted to the investigation of the THz mobility of the photoexcited electrons in GaAs nanobars, where the charge motion was probed in both far- and near-field regimes. Finally, we summarize main results of the thesis in Conclusion.

1. THz spectroscopy

1.1. THz spectral range

Traditionally, the THz spectral range is related to the frequency interval from 100 GHz to 3 THz. Figure 1 shows the THz spectral range in terms of various quantities and units (energy, temperature, wavelength, wavenumber), which are used in different contexts depending on the information of interest. The THz radiation has been applied to various fields of scientific investigations. As a vivid example, terahertz spectral range has received great interest in spectroscopy of the astronomical objects [6,7]. It is tied to the range of the black-body thermal radiation at a temperature of tens of Kelvins. Let us note that the cosmic background radiation has a characteristic temperature of about 3 K and this leads to further applications of the THz radiation in cosmology.

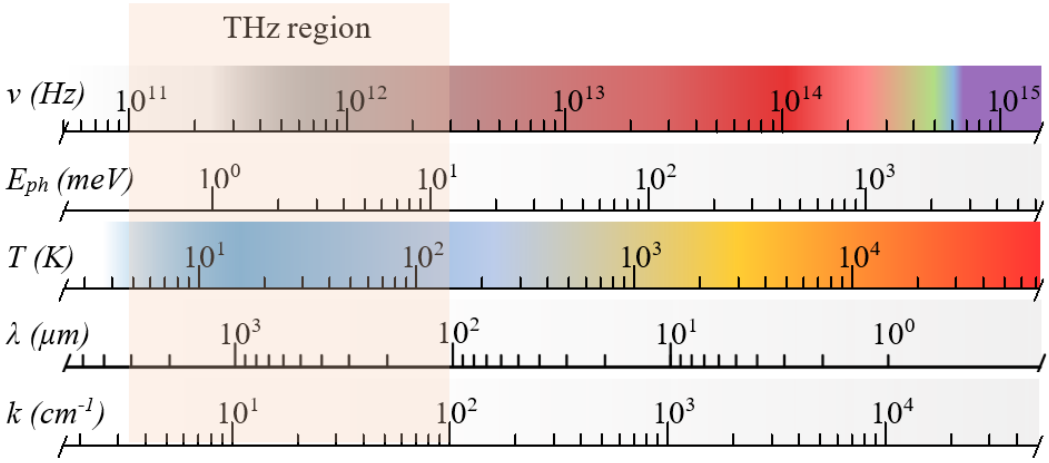

Figure 1. THz spectral range in different units representing frequency ν, photon energy $E_{ph}=h\nu$, temperature $T=E_{ph}/k_b$, wavelength λ and wavenumber k.

THz radiation is absorbed by soft vibrations and by librations or rotations of molecules in the polar solutions and in the gases. While this fact finds its use in the chemical analysis [8-10], it limits some potential applications. As an example, THz radiation, which is non-invasive and sensitive to the difference between the cancerous and non-cancerous cells, can penetrate only a few millimeters of tissues and barely reflect back. Nevertheless, the investigations in this area are being intensively conducted by various scientific groups over the world [11-14].

Regarding the solid-state research field, there is a number of phenomena in semiconductor and dielectric materials that possess resonances in the given spectral range. The metals are opaque for the THz waves due to strong absorption by free electrons. On the other hand, application of THz radiation allows careful characterization of the charge motion in the photoexcited or doped semiconductors (here we speak essentially about the free carrier densities roughly of 10^{14} – 10^{19} cm^{-3}) [15,16]. The THz photon enables an access to the tunneling [17,18] and scattering processes [19-21]; it is sensitive to excitons [22,23], and to either classical or quantum electron confinement in nanostructures [24,4]. It has been shown

that energy of the transient gap of some superconductors around their transition temperature corresponds to the THz frequency region [25-27]. The THz spectra are also quite important in the study of dielectrics since they feature low-frequency vibrational modes, which, in relation with structural phase transitions (e.g. in ferroelectric materials), are frequently called soft modes and are at the origin of structural instability [28,29]. As an aside, transparency of the most nonmetallic constructions for THz radiation has promoted a contactless non-invasive THz imaging in the investigations of the ancient arts [30] and in various security systems [31].

From the point of view of the physical phenomena used for the generation of coherent electromagnetic radiation, the terahertz range bridges the gap between two worlds: lying between microwaves and infrared frequencies it merges with the world of electronics from one side and with the optical one from the other (figure 1). Radio and microwave generation traditionally involves charge transport at a characteristic speed of electrons and consequently, achieving higher (THz) frequencies demand higher fields applied to smaller structures. Above 100 GHz this approach is hindered by parasitic capacitance and material electrical breakdown. From the optical side, radiative transitions between energy levels are typically used; however, decreasing the frequency down to 1 THz leads to a significant cutback of radiation brightness. Furthermore, the terahertz spectral lines correspond to energy levels separated by several meV and, therefore, the THz laser operation is easily disturbed by thermal fluctuations at room temperature.

Despite the described difficulties, many attempts have been made to fill this so called "terahertz gap". First significant results were achieved due to an implementation of backward-wave oscillators [32], which yield high intensity of coherent monochromatic THz waves. A qualitative step forward in the THz area was made in 1990s with the help of the ultrafast optoelectronics [33]. This led to the invention of the time-domain THz spectroscopy that provided the scientists with a high intensity pulsed coherent terahertz radiation and allowed a phase-sensitive "gated" detection technique. The time-domain THz spectroscopy is described in detail in the next section. Further techniques accessing the THz range became available after the year 2000; electron acceleration-based sources, such as synchrotron and free electron laser, are able to provide high intensity tunable THz radiation [34,35,36,37,38]. However, these beamlines are parts of large-scale facilities and can hardly provide an easy access to the experiment. The next approach that is worth to mention is a quantum cascade laser (QCL), which is based on the electron intersubband transition in multiple quantum well semiconductor heterostructures [39-41]. The QCL devices correspond to relatively small chips emitting narrow portion of the spectrum. However, several chips can be integrated in a single device to cover broader THz range. A major disadvantage of QCLs is the need of cryogenic temperatures for their operation, which makes them less suitable for applications.

1.2. Time-domain spectroscopy

Time-domain terahertz spectroscopy (TDS) is a technique based on the generation and detection of broad band THz pulses by means of femtosecond optical pulses. Interaction of the femtosecond optical pulse with the matter may result in a polarization or current surge producing the THz pulse via two approaches: nonlinear optics and photoconductive switching. The former one involves optical rectification [42] of the laser pulse inside a non-linear crystal

(ZnTe, GaP, InP, $LiNbO_3$, etc.) [43,44]. In this case the bandwidth of the THz pulse is mainly defined by the spectral density and time profile of the optical pulse and by the properties of the crystal (condition of phase matching between the optical and THz waves, phonon energy, second order nonlinear susceptibility of the material etc.). The latter one is based on a generation of picosecond current pulse in a biased semiconductor [45-47]. The bias field can be applied through an antenna structure to optimize the THz emission. The current surge is triggered by a femtosecond laser pulse that generates free carriers in the semiconductor wafer. In order to achieve emission in the THz regime, a high electron mobility and a short carrier lifetime are required. Therefore, apart from the peculiar electrode architecture, production of the semiconductor components of the photoswitch involves specific fabrication techniques [48]. Some of the most frequently used materials are GaAs, InP or Si based semiconductors.

Detection of the THz pulses in TDS is inherently based on the fundamentally same physical principles as used for the generation. An electric field of the freely propagating THz pulse is applied either to a non-linear crystal in order to induce (or change) its birefringence (linear electro-optic effect) or to a photoconductive switch in order to trigger a current pulse [49,50]. In both cases the measurable quantities are proportional to an instantaneous value of the THz electric field and depend on a simultaneous presence of the THz and optical pulses. Thus, by changing the time delay (figure 3) between the (picosecond) THz pulse and a (femtosecond) sampling optical pulse one directly measures the THz field evolution in time, so called wave form $E(t)$ (figure 2a). Such phase sensitive detection allows one to obtain complex spectra of the THz pulse $E(\omega)$ (figure 2b) via the Fourier transformation.

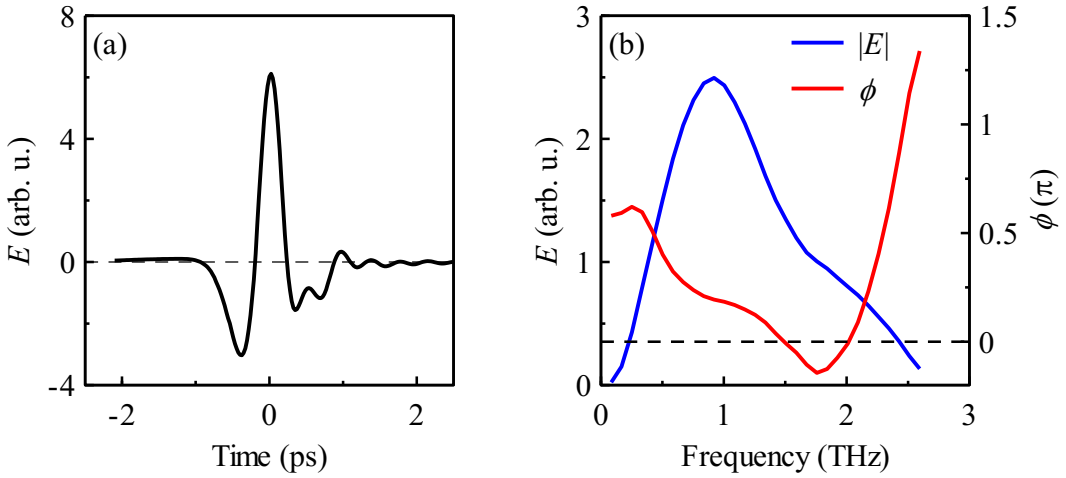

Figure 2. (a) Free space THz waveform $E(t)$; (b) its complex spectrum $E(\omega) = |E(\omega)|\, e^{-i\phi(\omega)}$.

The THz radiation propagating in free space is focused onto the sample and onto a detector by far infrared lenses or (paraboloidal or ellipsoidal) metallic mirrors. The spectroscopic measurements of samples in steady state then typically involve a so-called reference measurement (i.e. an experiment without the sample); this allows one to get rid of the instrumental functions of the experimental setup. Let us denote the reference waveform as $E_{ref}(\omega)$. Then the real and imaginary parts of the material refractive index N can be retrieved from a complex transmission function

$$T(\omega) = \frac{E(\omega)}{E_{ref}(\omega)}. \tag{1.1}$$

This approach has been sucesfully employed to characterize bulk [51,52,53] and thin films [54,55] materials.

1.2.1. Optical pump – THz probe (OPTP) spectroscopy

In the OPTP method THz radiation probes optically activated processes in a semiconductor material; the objective of this approach is to characterize a photoinduced change of the complex conductivity $\Delta\sigma$ of the sample [15]. This is obtained through a change of the THz waveform $\Delta E(t)$ due to the sample photoexcitation and requires introduction of an additional branch for the optical pumping beam (figure 3). Precise time synchronization between the THz and the optical pulses enables the time resolved measurements, i.e. ΔE is measured as a function of the pump-probe delay t^p. Together with a contactless nature of the approach, it makes this technique unique for the ultrafast conductivity investigation. Introduction of a negative delay of the pumping beam makes it possible to choose any particular time for the measurement of the THz field $\Delta E(t; t^p)$ with respect to the moment of excitation. A number of variable experimental parameters such as excitation wavelength, charge carrier density (via the pump pulse fluence) and sample temperature enables an access to complimentary information.

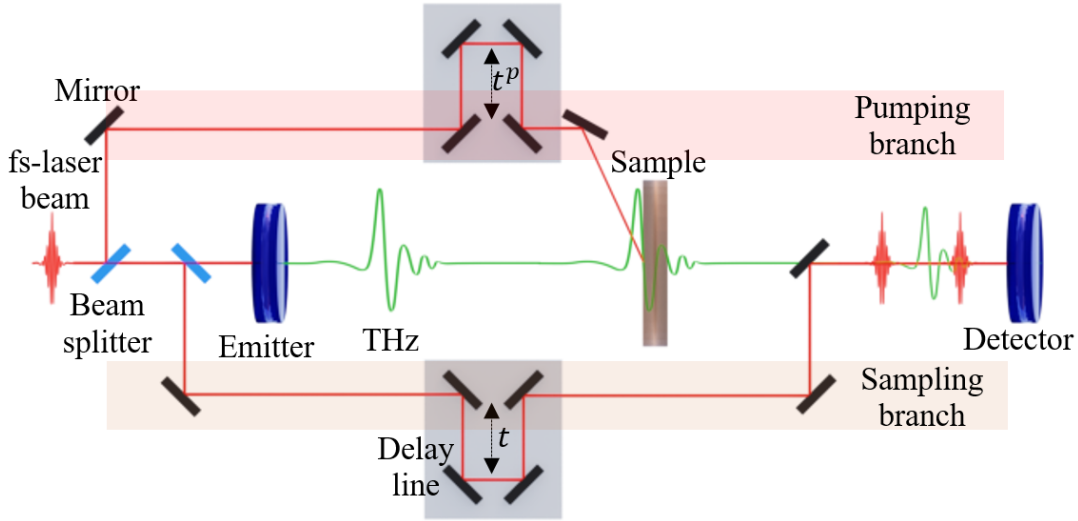

Figure 3. Principal scheme of the OPTP-TDS experiment.

Apart from the waveform measurements, the time resolved approach allows characterization of the carriers dynamic. For this purpose, the time delay τ between the THz and the sampling pulses is adjusted to a maximum of the transient wave form ΔE_{max}, whereas the scan of the pump-probe delay t depicts the time evolution $\Delta E_{max}(t)$ of the carriers transport (figure 4). This evolution involves various processes such as carrier generation, recombination, scattering, confinement, etc.

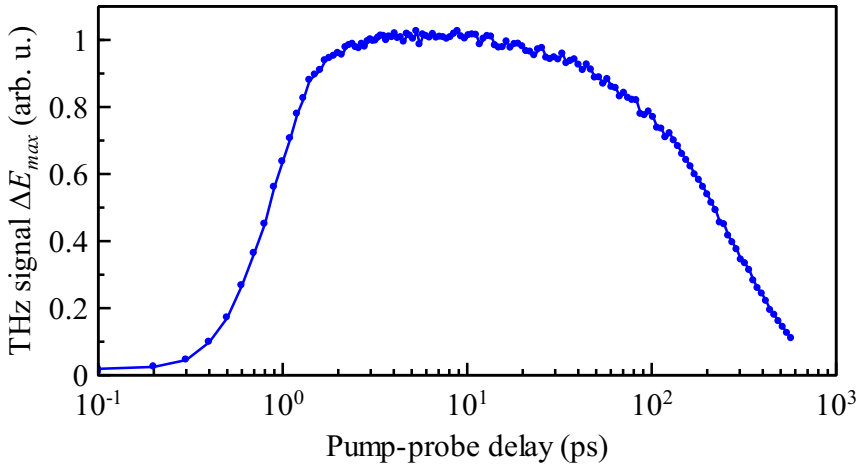

Figure 4. An example of pump-probe scan of the carrier dynamics measured in a thin film of GaInAs at 1.2μm excitation wavelength.

In the case of relatively slow relaxation processes, i.e., when the signal decay is on the time scale of several ps or slower, $\Delta\sigma$ might be considered as constant on a few-ps scale [56]. Such consideration is used for all studied samples in this work. On the other hand, when carriers exhibit ultra-fast (essentially sub-ps) [57,58] dynamics, specific analysis of the data must be used for the measurement interpretation [59,60].

1.2.2. Multi-THz Time Domain spectroscopy

As it was mentioned earlier in Sec. 1.2, the bandwidth and intensity of the THz pulse in TDS-THz system are limited by the properties of the THz emitter and detector material, in particular, by the existence of polar phonons in solid crystals in the range $\sim 5-12$ THz which strongly interact with THz waves. This can be overcome using the air (or a specific gas) as a medium for both generation and detection of the THz radiation. Indeed, very little dispersion of the air ensures convenient conditions for the optical-THz phase matching and the bandwidth of the THz pulse will thus be limited only by the bandwidth of the laser pulse.

Generation of the ultra-broadband THz pulses from the air plasma is based on a third-order ($\chi^{(3)}$) non-linear interaction between strongly focused fundamental optical wave and its second harmonic creating a short plasma filament in the centrosymmetric air medium [61-65]. This mechanism is often referred as two-color laser mixing process or four-wave rectification (in analogy to the second order optical rectification in non-centrosymmetric crystals). In spite of the higher-order nonlinearity involved here, quite strong THz fields (up to ~ 100 kV/cm) are typically achieved due to strong focusing.

A scheme of the principal experimental setup is shown in figure 5; a focused laser beam is frequency doubled using nonlinear (BBO) crystal positioned between the lens and the focal point. The co-propagating fundamental beam and its second harmonic (SH) create a plasma filament generating linearly polarized THz pulse.

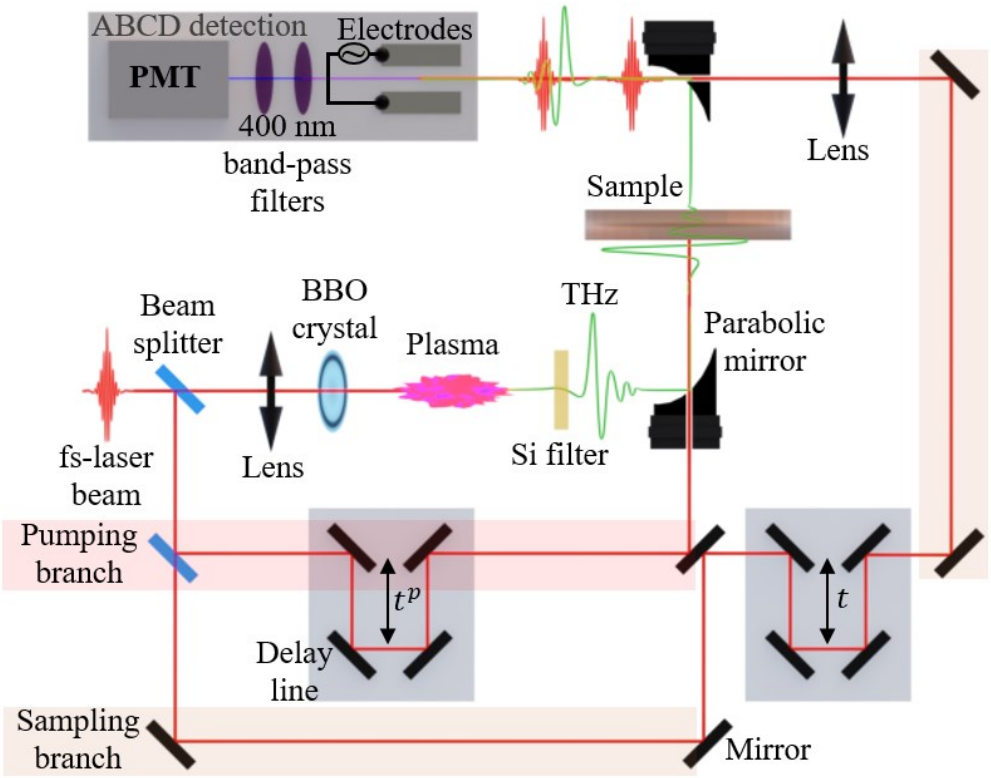

Figure 5. Scheme of the multi-THz TDS experiment with the optical-pump branch.

Detection of the ultra-broadband THz pulses, often referred as air-biased coherent detection (ABCD), is based on the *third-order* optical nonlinearity of the air induced by the THz field. The sampling and THz beams are focused to the same spot between needle electrodes. The field applied to the electrodes E_{ext} is parallel to the electric field of the THz beam E_{THz} and the voltage is switched between positive and negative values at a frequency synchronized with the laser repetition rate f_L (we use typically $f_L/10$). The process can be understood as electric-field-induced second harmonic generation of the sampling pulse in the air. The generated SH intensity is proportional to $(E_{ext} + E_{THz})^2$, the part of this intensity modulated at frequency f_L is then $2E_{ext}E_{THz}$ and this value (linear in E_{THz}) is delivered by the lock-in detection. Figure 6 shows THz signal (in time and frequency ranges) generated using the Ti:sapphire ultrafast regenerative laser amplifier (Spitfire ACE) with pulse duration ~40 fs. The method enables TDS measurements up to 20 THz.

In analogy to the OPTP-TDS technique described in 1.2.2, optical excitation of the sample can be introduced to the experiment enabling access to the complex photoinduced conductivity in the multi-THz range.

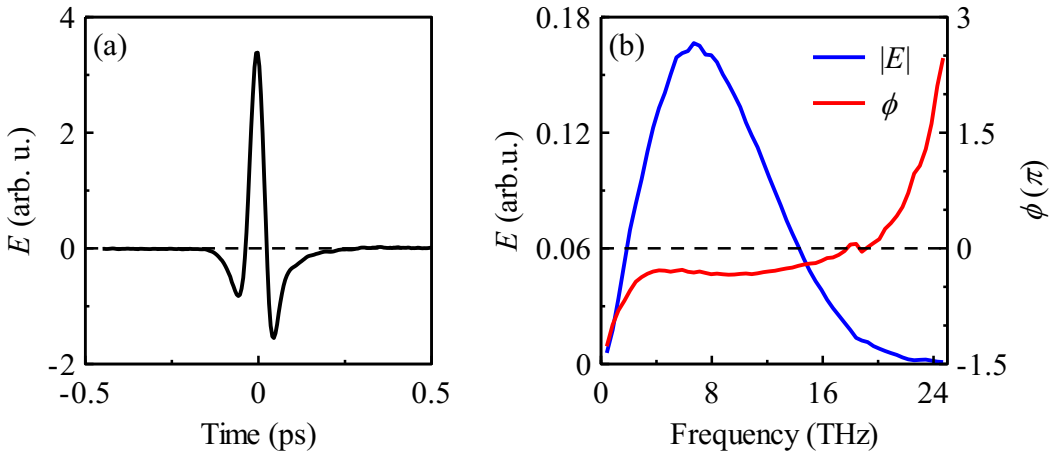

Figure 6. (a) Free space multi-THz waveform *E(t)*; (b) its complex spectrum $E(\omega) = |E(\omega)|\, e^{-i\phi(\omega)}$.

1.2.3. Multi-THz –mid-Infrared pulsed spectroscopy

Spectral bandwidth of the THz pulses generated in the air is essentially defined by the bandwidth of the optical pulses used for the generation. Thus, using the same principles as for the standard multi-THz approach, further broadening of the THz pulse spectrum can be achieved by means of spectral broadening of the initial laser beam. As it was shown in [66, 67], the compression of the laser pulse down to sub-20fs duration time gained the bandwidth of the signal above 100 THz. Coherent detection of such broadband THz signal is based on optical-THz sum-frequency generation (SFG) in $\chi^{(2)}$-crystal using original optical pulses. This technique is not phase-sensitive, however, as well as above-described THz and multi-THz techniques, it enables optical-pump – mid-infrared probe (i.e., time-resolved) measurements of the samples. In comparison with the conventional FTIR spectroscopy, pulsed SFG approach thus provides both spectral and temporal resolution of the infrared signal. We refer to this technique as the Multi-THz – mid-infrared (IR) pulse spectroscopy and its time-resolved variant (optical pump – mid-infrared probe) will be abbreviated as OPMIP.

1.2.4. Near-Field THz spectroscopy

Combination of the THz spectroscopy with the atomic force microscopic (AFM) technique enables THz measurements in the near-field regime (figure 7). AFM tip here acting as a scatterer of the THz pulses is oscillating at frequency f_T in a close vicinity to the surface of the probed structure. The scattered signal modulated at $n \times f_T$ (i.e., the tip frequency and its higher harmonics) is detected using lock-in amplifier. Scanning AFM configuration makes it possible to perform THz mapping of the surface of the investigated material. Thus, TDS THz approach allows local measurements of the scattered THz waveform. Further development includes implementation of the pumping branch into the experiment, enabling the measurements of the local carrier dynamics and time-dependent conductivity contrasts of the surface of the investigated structure. However, complex nature of the scattering processes makes it very difficult to evaluate quantitatively the local conductivity spectra.

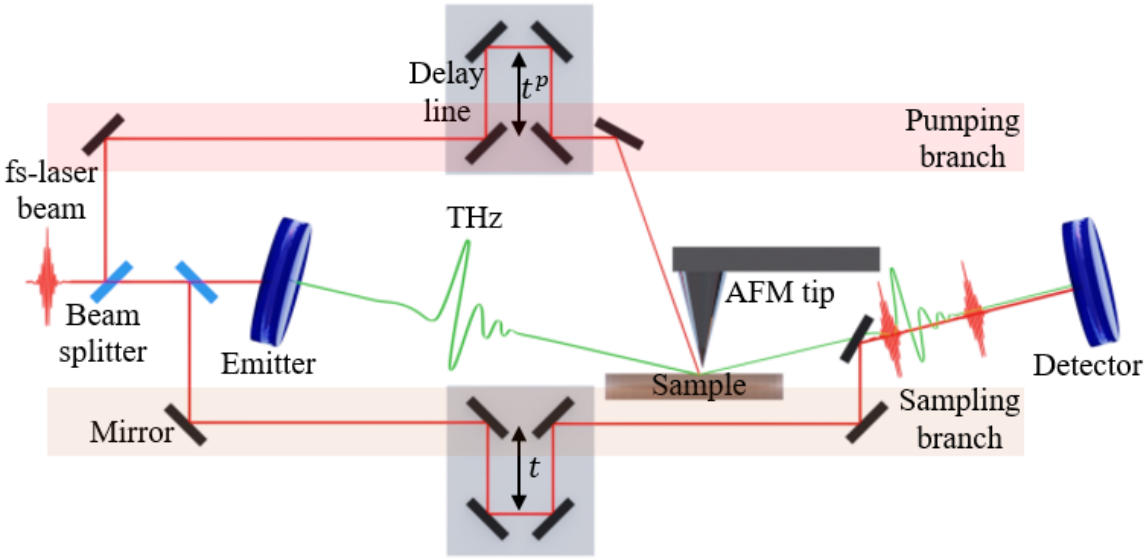

Figure 7. Scheme of the near-field THz experiment with the optical-pump branch.

2. THz response of photoexcited nanomaterials

In this chapter we describe a general approach to evaluation of the response of optically excited semiconductor materials to the THz broadband radiation. For this purpose, we solve the wave equation inside photoexcited plane-parallel sample (section 2.1). The excitation is represented by a photoconductivity contribution $\Delta\sigma$ which reflects the motion of charges submitted to the THz field.

Section 2.2 is devoted to the most frequently used approaches to model the photoconductivity $\Delta\sigma$. This modelling has two aspects: analysis of microscopic conductivity (response function of charge carriers) and the effect of depolarization fields (playing an important role in any inhomogeneous material). We introduce here the Drude model, the hoping conductivity model and the phenomenological Drude-Smith model. After that, along with classical Monte-Carlo simulations of the carrier motion on the microscopic scale, a new quantum mechanical model of the electron mobility in the terahertz frequency range is introduced in order to describe the charge quantum confinement in nanoparticles. The localized plasmon model is introduced afterward. Much attention in this work is devoted to the effective medium theory (dielectric mixing rules), which provides a physical background for the localized plasmon phenomenon, and which allows to distinguish between the charge confinement phenomena and the effects of the depolarization fields. This has a primary importance for our study.

Section 3.3 introduces the main results of the effective medium description into the wave equation solution by means of an effective $\Delta\sigma$ of the sample and provides ready-to-use formulas for the analysis of experimental transient transmittance and reflectance spectra.

Finally, section 3.4 provides a summary of the results and a recipe how to proceed in analysis of experimental data.

2.1. Wave equation

Evolution of the electromagnetic field propagating inside an isotropic neutral (electric charge density $\rho = 0$) medium can be described by the Maxwell's equations (ME). We write here the ME in the frequency domain for the component ω (i.e., $\boldsymbol{E}e^{-i\omega t}$):

$$\begin{aligned} \nabla \times \boldsymbol{E} &= i\omega \boldsymbol{B}\,, & \nabla \cdot \boldsymbol{B} &= 0, \\ \nabla \times \boldsymbol{H} &= \boldsymbol{j} - i\omega \boldsymbol{D}\,, & \nabla \cdot \boldsymbol{D} &= 0, \end{aligned} \tag{2.1}$$

and the constitutive relations:

$$\begin{aligned} \boldsymbol{D} &= \varepsilon\varepsilon_0 \boldsymbol{E}, \\ \boldsymbol{B} &= \mu\mu_0 \boldsymbol{H}, \\ \boldsymbol{j} &= \Delta\sigma \boldsymbol{E}, \end{aligned} \tag{2.2}$$

where ε, ε_0 and μ, μ_0 are the material and vacuum permittivity and permeability, respectively, $\boldsymbol{j}$ is the current density, $\boldsymbol{E}$ and $\boldsymbol{H}$ are the electric and magnetic fields, respectively, $\boldsymbol{D}$ is the electric and $\boldsymbol{B}$ is the magnetic induction. We consider non-magnetic media ($\mu = 1$) and also that any background conductivity of the sample (i.e., its part not related to optical excitation) is included in the complex permittivity ε through the equivalence $\varepsilon = i\sigma/\varepsilon_0\omega$. $\Delta\sigma$ has the meaning of the photoinduced conductivity (due to the pump pulse) and the current $\boldsymbol{j}$ is the related current driven by the field $\boldsymbol{E}$. Maxwell's equations result in the following expression for the electric field:

$$\nabla \times (\nabla \times \mathbf{E}) = \varepsilon\varepsilon_0\mu\mu_0\omega^2\boldsymbol{E} + i\mu\mu_0\omega\boldsymbol{j}\frac{\partial \boldsymbol{j}}{\partial t}. \tag{2.3}$$

Considering $\nabla \times (\nabla \times \boldsymbol{a}) = \nabla \cdot (\nabla \cdot \boldsymbol{a}) - (\nabla \cdot \nabla) \cdot \boldsymbol{a}$, and taking into account $\nabla \cdot \boldsymbol{E} = 0$ (isotropic medium is considered) we obtain the wave equation:

$$\nabla^2\boldsymbol{E} = -\varepsilon\varepsilon_0\mu\mu_0\omega^2\boldsymbol{E} - i\mu\mu_0\sigma\omega\boldsymbol{E}. \tag{2.4}$$

We are looking for the solution of the equation 2.4 in a form of a plane wave:

$$\boldsymbol{E}e^{-i(\omega t - \boldsymbol{k}\cdot\boldsymbol{r})}. \tag{2.5}$$

Thus, we can rewrite the expression for the wave equation as follows:

$$\nabla^2\boldsymbol{E} + k^2\boldsymbol{E} = -ik_0Z_0\Delta\sigma\boldsymbol{E}, \tag{2.6}$$

where the module of the wave vector is $k = \varepsilon\varepsilon_0\mu\mu_0\omega^2 \equiv \frac{\omega^2N^2}{c^2}$, $k_0 = \frac{\omega}{c}$, and the vacuum wave impedance $Z_0 = \mu_0 c$.

We further assume a propagation along *z*-axis and a linear polarization of the probing THz beam; then equation 3.6 becomes scalar. We denote by *E* the THz field propagating in the sample in equilibrium (i.e., it obeys equation 3.6 without the right-hand-side) and by ΔE its change due to the photoexcitation (figure 8). Thus, the wave equation 2.6 for the transient terahertz field ΔE can be written as follows:

$$\frac{d^2\Delta E}{dz^2} + k^2\Delta E = -ik_0Z_0\Delta\sigma(E + \Delta E). \tag{2.7}$$

The term at the right-hand side stands for the transient polarization of the sample expressed in the form of the photoinduced current. In principle the photoconductivity $\Delta\sigma$ and the transient field ΔE depend on frequency (ω), pump-probe delay (t^p), coordinate z and the pump-pulse fluence (or z-dependent photocarrier density). Throughout this work we do not explicitly denote these dependences in order to simplify the formulas. We write such a dependence just in cases when emphasis is needed.

Since in our experiments the time evolution of photoexcitation is slow on the THz pulse timescale (quasi-steady-state approximation), we can describe the dynamics in terms of time-dependent THz spectra: $\Delta\sigma(\omega, t^p), \Delta E(\omega, t^p)$. As it was mentioned before, the OPTP measurements allow changes of the pump-probe delay enabling probing of the sample photoexcitation dynamics. It should be noted that in a general analysis involving ultrafast (sub-ps) dynamics, two frequency variables ω and ω^p related to the gated detection of the THz pulse (time t) and to pump-probe delay (t^p) should be introduced and their mixing should be properly taken into account [59, 60].

The wave equation 2.7 is a non-linear partial differential equation (PDE), which can *only* be solved using numerical approach. However, its analytical solution, which often provides a better insight into the physics of the problem, is possible in the limit of the small signal $\Delta E \ll E$. Indeed, dropping ΔE term at the right-hand side leads to linearization of the PDE. Regarding the THz conductivity measurements of the semiconducting (nano-)materials, the low signal approximation is quite reasonable and may describe well a broad range of experimental conditions. Nevertheless, its validity must be carefully estimated for every particular measurement. Therefore, it is necessary to have both numerical and analytical model at hand. Depending on the experimental conditions we employ one or the other approach throughout this work.

2.1.1. Analytical solution of the wave equation

In the small signal limit ($\Delta E \ll E$) the wave equation becomes a linear inhomogeneous second-order partial differential equation. Its general solution ΔE is defined as follows:

$$\Delta E = \delta e^{ikz} + \gamma e^{-ikz} + \frac{Z_0}{2n}\left[e^{-ikz}\int_0^z \Delta\sigma E e^{ikz}\,dz - e^{ikz}\int_0^z \Delta\sigma E e^{-ikz}\,dz\right], \qquad (2.8)$$

where δ and γ are the arbitrary coefficients of the general solution ($\delta e^{ikz} + \gamma e^{-ikz}$) of the complementary equation.

Sample reflection and transmission of the THz field obey the standard Fresnel equations:

$$\begin{aligned} r_1 &= \frac{n - n_1}{n + n_1}, & r_2 &= \frac{n - n_2}{n + n_2}, \\ t_1 &= \frac{2n_1}{n + n_1}, & t_2 &= \frac{2n}{n_2 + n}. \end{aligned} \qquad (2.9)$$

t_i and r_i are the transmission and internal reflection coefficients at the input and output sample surfaces, respectively; n and n_i are the refractive indexes of the sample in equilibrium and of adjacent media (figure 8). Transient fields ΔE, ΔE_r and ΔE_t are transient fields induced by the photogenerated carriers ($\Delta\sigma$) inside the sample.

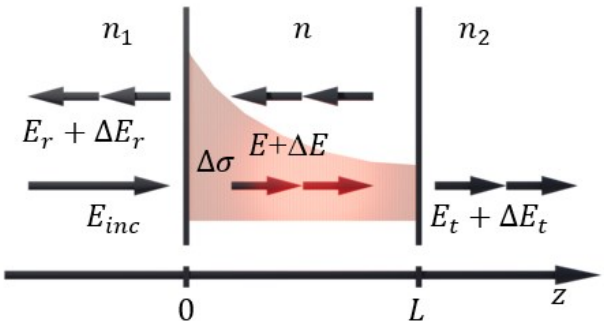

Figure 8. Scheme of the THz field propagation in the sample with thickness L upon photoexcitation with conductivity $\Delta\sigma$: E_{inc} is the incident field, E_r, E_t and E are the reflected field, transmitted field and field inside the sample, respectively. Similar notation is used for the transient fields ΔE_r, ΔE_t and ΔE.

The z-dependence of the transient conductivity $\Delta\sigma$ must be taken into account due to a possible strongly inhomogeneous distribution of the conduction band electrons along the sample, which depends on the sample optical properties and on the photoexcitation conditions.

Let us define a as a parameter that describes multiple internal reflections of the THz beam inside the sample (related to Airy function for Fabry-Pérot etalon):

$$a = \left(1 - r_1 r_2 e^{2ikL}\right)^{-1} \tag{2.10}$$

Thus, the THz field inside the sample in its equilibrium state can be written as:

$$E = E_{inc} t_1 a\left[e^{ikz} + r_2 e^{-ik(z-2L)}\right]. \tag{2.11}$$

The relations among the transmitted and reflected fields are defined via the continuity conditions at the sample interfaces:

$$\begin{aligned} \Delta E_r &= \Delta E(z=0), & \Delta E_t &= \Delta E(z=L), \\ \Delta H_r &= \Delta H(z=0), & \Delta H_t &= \Delta H(z=L). \end{aligned} \tag{2.12}$$

Putting the solution of the wave equation 2.8 into these boundary conditions we obtain solutions for the transient transmitted ΔE_t [68] and reflected ΔE_r [69] THz fields:

$$\Delta E_t = -\frac{Z_0 t_1 t_2 a^2}{2n} E_{inc}\, e^{ikL}\left[\left(1 + r_1 r_2 e^{2ikL}\right)\int_0^L \Delta\sigma \mathrm{d}z + r_1 \int_0^L \Delta\sigma\, e^{2ikz}\mathrm{d}z + r_2 e^{2ikL}\int_0^L \Delta\sigma\, e^{-2ikz}\mathrm{d}z\right], \tag{2.13}$$

and

$$\Delta E_r = -\frac{Z_0 t_1^2 a^2}{2n_1} E_{inc} \left[2r_2 e^{2ikL} \int_0^L \Delta\sigma \, dz + \int_0^L \Delta\sigma \, e^{2ikz} dz + \left(r_2 e^{2ikL}\right)^2 \int_0^L \Delta\sigma e^{-2ikz} \, dz \right]. \tag{2.14}$$

Both expressions consist of the same integrals describing the generation process of the transient wave ΔE under phase matched or non-phase matched regimes for the primary field E propagating inside the sample. At any place of the sample, the current $\Delta\sigma E$ generates a partial secondary THz wave ΔE in the forward or backward direction with respect to the direction of propagation of the wave E. The former case is phase-matched since both waves remain in phase and the secondary wave amplitude ΔE will linearly grow as a result of in-phase generation; the latter case is non-phase-matched.

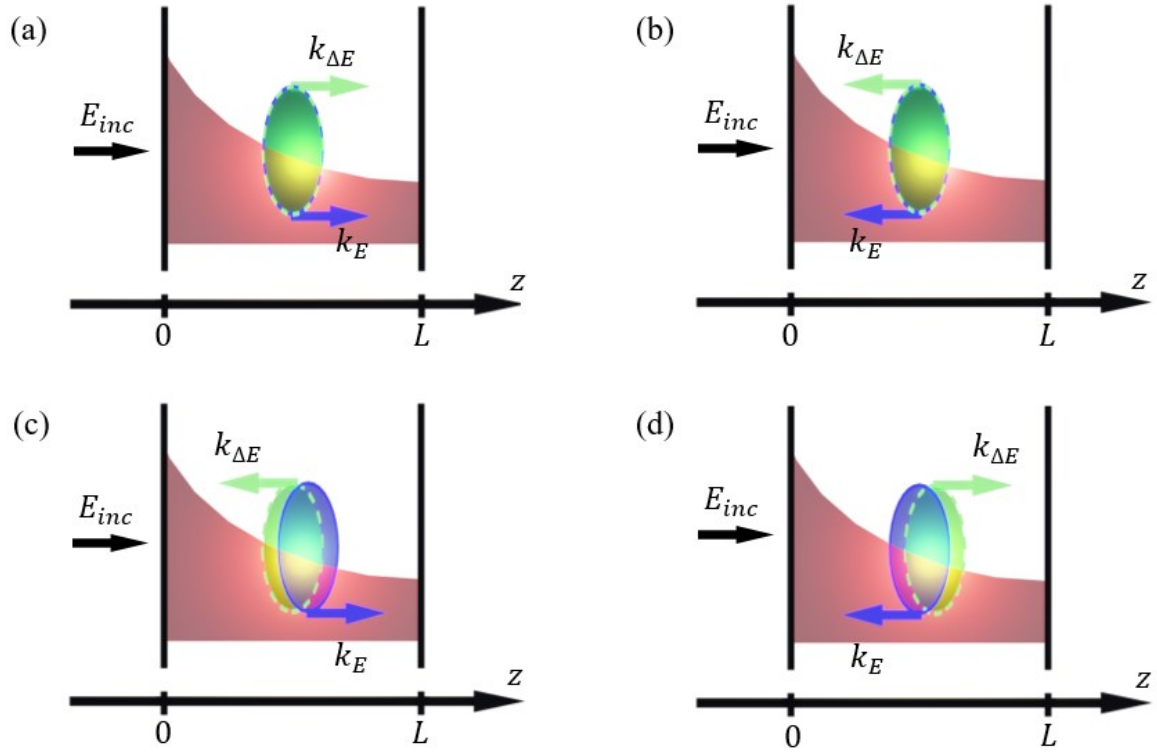

Figure 9. Schematic representation of the propagation of the primary E and transient THz ΔE fields inside the sample (the directions of their wave vectors k_E and $k_{\Delta E}$ are indicated): (a) and (b) – phase matching conditions, for the co-propagating E and ΔE; (c) and (d) – non-phase matching regime, when the transient THz field is emitted in the backward direction with respect to the propagation of E.

In particular, the first integral of both equations corresponds to the phase matched regime, when both fields co-propagate (either to the right or to the left as seen in figure 9a,b). Let us comment on this shortly. For example, the prefactor $2r_2 e^{2ikL}$ of this integral in the transient reflected field ΔE_r shows that this wave must experience a back-side reflection (r_2),

a phase change $2kL$ and that it is composed of 2 contributions (figure 9a and figure 9b). The second and the third integrals describe the non-phase matched generation as depicted in figure 9c and figure 9d, respectively. The second integral in 3.14 represents direct backward generation of ΔE (figure 9c) while the third one (figure 9d) requires a back-side reflection of both E and ΔE (term r_2^2) and a phase change in between $2kL$ and $4kL$. Similar reasoning can be made also for the transmitted wave ΔE_t to make this interpretation complete.

In the experiment the THz field measured for the sample in the equilibrium state (without optical excitation) is used as the reference signal. Thus, transient transmission and transient reflection functions can be found as follows:

$$\Delta T = \frac{\Delta E_t}{E_t}, \qquad \Delta R = \frac{\Delta E_r}{E_r}. \tag{2.15}$$

In the case of thin films, the general formulas 2.13 and 2.14 yield simple relations for the transient signals in terms of the sheet conductivity of the film. For example, for the transient transmission we obtain:

$$\Delta T = -\frac{Z_0}{n_1 + n_2} \int_0^L \Delta\sigma(z)\, dz \tag{2.16}$$

Unlike in the bulk homogeneous (semi-) conductor materials, in nanostructured samples (i.e., nanowires, quantum dots, polycrystals, etc.) with characteristic dimensions orders of magnitudes smaller than the wavelengths of the probing THz radiation, the characteristic distance of the electron transport may approach or exceed the nanocrystal size. Here we reason in terms of the diffusion and/or ballistic transport lengths that carriers can cover within one period of the probing radiation (~ ps). If these lengths exceed the nanocrystal size, it leads to a classical confinement of the charge carriers. If, moreover, the de Broglie wavelength is comparable to the mean free path of carriers a quantum confinement of carriers is expected. Both these conditions lead to a complicated material response requiring specific models for its interpretation.

2.2. Photoconductivity models

In this section we describe the carrier conductivity in terms of the microscopic mobility $\mu(\omega)$

$$\mu(\omega) = \frac{\sigma(\omega)}{e_0 N_e}, \tag{2.17}$$

which can be understood as the carrier response function (conductivity per single unit charge). Here e_0 is the elementary charge and N_e is the conductive charge carrier density.

2.2.1. Drude model

The model was developed in the beginning of the 20th century to describe charge transport in metals [70,71]. It considers the conduction electrons inside material as a free electron gas and thus adapts the kinetic theory to it; the model considers collisions of the free electrons with heavy particles (lattice ions, impurities) as the only relaxation mechanism. Then, the transport of a charge carrier with the effective mass m_{eff} is characterized in terms of the

relaxation time τ, i.e. time interval between two instant scattering events. In the framework of this description, the equation of charge motion in a time dependent electric field provides the following expression for the frequency dependent charge mobility:

$$\mu_{Dr}(\omega) = \frac{e_0\tau}{m_{eff}}\frac{1}{1-i\omega\tau}. \tag{2.18}$$

An example of the Drude spectrum of free electrons in GaAs is presented in figure 10. The model has been extensively applied to describe THz response of charge carriers in bulk semiconductors [51, 72, 73,74]. At a given carrier concentration n the Drude conductivity is given by the expression

$$\sigma_{Dr}(\omega) = \varepsilon_0\omega_p^2\frac{\tau}{1-i\omega\tau}, \tag{2.19}$$

where ε_0 is the vacuum permittivity and ω_p is called the plasma frequency. It is defined by the expression

$$\omega_p = \sqrt{\frac{ne_0^2}{m_{eff}\varepsilon_0}}, \tag{2.20}$$

and determines a frequency limit for the light that can propagate through a material: radiation with a frequency $\omega < \omega_p$ is reflected by the carrier plasma while for $\omega > (\omega_p + \frac{1}{\tau})$ the plasma becomes progressively transparent for the radiation.

2.2.2. Hopping model

The hopping conductivity may dominate over the band-like conductivity in disordered materials. In this case, in analogy with the Eyring's rate theory for ionic conductivity [75], conductivity can be well described by the charge hopping among localized states below the conduction energy band. Under an applied time-dependent electric field electrons might hop between two states by means quantum tunneling through an energy barrier. The Dyre's random free-energy barrier approach [76] is an example of the model employed to characterize a real systems behavior (figure 10) [56]. It defines the hopping conductivity

$$\mu_{hop}(\omega) = i\omega\mu_\infty\left[1-\frac{\ln\tau_{min}-\ln\tau_{max}}{\ln(1-i\omega\tau_{min})-\ln(1-i\omega\tau_{max})}\right]\frac{\ln\tau_{max}-\ln\tau_{min}}{1/\tau_{min}-1/\tau_{max}}, \tag{2.21}$$

where the distribution of the relaxation times is limited by the τ_{min} and τ_{max} values and μ_∞ is a high-frequency value of the mobility (i.e. a value at the saturation).

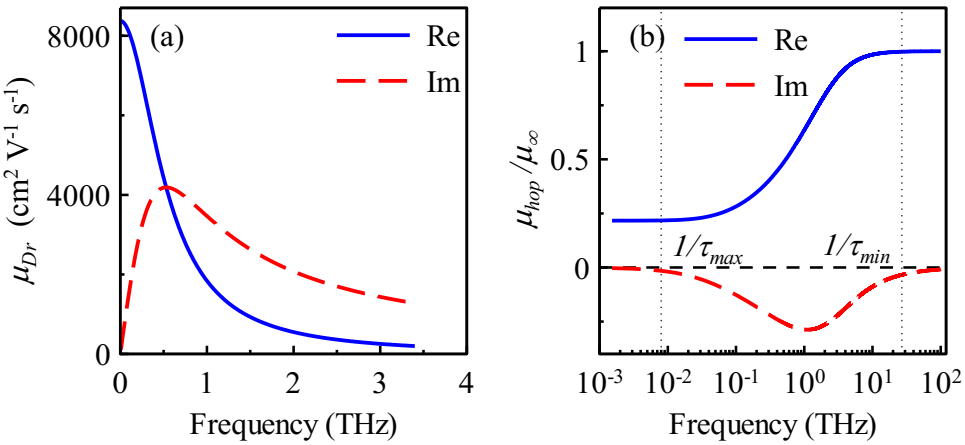

Figure 10 (a) calculated Drude mobility with parameters τ_s = 300 fs *and* m_{eff} =0.065 m_0; (b) Dyre's model of hopping conductivity with values τ_{min} = 50 fs and τ_{max}= 5 ps.

The frequency value at which the conductivity saturation starts usually lays above the THz region. The monotonic behavior of the Dyre's conductivity within the relaxation times interval (τ_{min},τ_{max}), as observed in figure 4(b), corresponds to a general assumption of the distribution of energy barriers with equal probability.

2.2.3. Drude-Smith model

The classical Drude model (3.2) cannot be directly applied to nanomaterials where the conductivity peak at is observed at non-zero frequency; indeed, such a behavior is a common feature of the carrier localization. Among different phenomenological attempts to describe the localized charge dynamics the most applicable modification was proposed by N. V. Smith in 1968 [77]. Trying to describe unusual optical properties of mercury, Smith suggested that electron backscattering is strong enough in the material to reverse the direction of the electron current and proposed a relevant current-current autocorrelation function. The final expression for the complex conductivity is then written as

$$\mu(\omega) = \mu_{0,DS}\frac{1}{1-i\omega\tau_{DS}}\left[1+\sum_{j=1}^{\infty}\frac{c_j}{(1-i\omega\tau_{DS})^j}\right], \qquad (2.22)$$

where $\mu_{0,DS}$ is a phenomenological mobility amplitude, τ_{DS} is a Drude-Smith relaxation time and c_j represents the part of an initial electron velocity that is preserved after jth collision. If we denote θ as an angle between the original electron velocity and its velocity after j collisions, then c_j corresponds to $cos\theta$. An isotropic scattering process yields $c_j = 0$. Smith finally proposed to truncate the sum (3.7) and to consider only a single anisotropic scattering event [78] and he got the perfect fit of the experimental data for the mercury. This single scattering approximation is usually presented as the well-known formula for the Drude-Smith mobility

$$\mu_{DS}(\omega) = \mu_{0,DS}\frac{1}{1-i\omega\tau_{DS}}\left[1+\frac{c_1}{1-i\omega\tau_{DS}}\right]. \qquad (2.23)$$

This model was extensively employed to interpret THz photoconductivity in various types of nanostructured materials [79-83]. The parameter c_1 determines the degree of the charge localization in the spectral representation (figure 11): $c_1 = 0$ corresponds to the classical Drude model (completely free charge carrier), whereas $c_1 = -1$ means the complete localization.

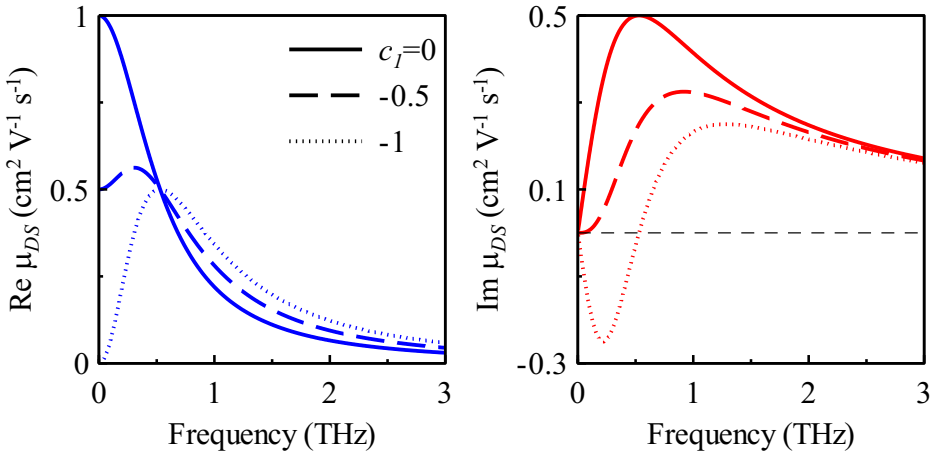

Figure 11 Real and imaginary parts of the Drude-Smith mobility at different values of c_1 with parameter $\tau_{DS} = 300$ fs and $\mu_{0,DS} = 1$.

Although the model is able to fit many experimental spectra in the classical THz spectral range (0.2-2.5 THz) and has been extensively used by several groups, it remains phenomenological and the results of the fit should be treated as such. E.g., it does not allow to distinguish between the charge carrier response function and the effective medium effects (described later in this thesis), both of which contribute to the spectral shape of the conductivity.

2.2.4. Semiclassical and Quantum calculations of the microscopic response function

In this chapter we describe two original approaches (semiclassical and quantum mechanical) introduced in our group and devoted to the quantitative evaluation of the localized carrier response by numerical calculations of the mobility $\mu(\omega)$. First, we deal with the carriers localized response related to the "classical" interaction of charges with the nanocrystal boundaries; indeed, the charge carrier transport in relatively large nanocrystals can be understood in the framework of the classical physics. However, a decrease of the nanocrystal size may result in a discretization and shift of electron energy levels leading to the so-called quantum confinement.

The first approach, described in detail in [84], is based on the *Monte Carlo* simulations of the classical thermal motion of free electrons inside a particle. The essential input parameters of the calculation are the density of carriers, shape and size of the nanocrystal, distribution function of the carrier velocity, carrier scattering time (electron mean free path) and the probabilities of electron transport to a neighboring nanocrystal and of its reflection and scattering on the nanocrystal boundary. Depending on the particular system and on the density of carriers (position of the Fermi level), either Maxwell-Boltzmann or Fermi-Dirac distributions can be applied. The spectrum of microscopic mobility is then defined via Kubo

formula by using the velocity autocorrelation function. In the case of small carrier densities described by the Maxwell-Boltzmann distribution, we obtain

$$\mu_{ij}(\omega) = -\frac{e_0}{k_B T}\int \langle v_i(0) v_j(t')\rangle e^{i\omega t'}\,\mathrm{d}t', \tag{2.24}$$

where

$$i, j = x, y, z. \tag{2.25}$$

v_i are components of the vector of carrier velocity at a given time t', k_B and T are the Boltzmann constant and the carrier temperature, respectively. The average value $\langle v_i(0) v_j(t')\rangle$ is calculated over an ensemble of simulated electron trajectories.

Figure 12 shows the microscopic conductivity in isolated cube-shaped GaAs nanocrystals at room temperature for the carrier concentration of 10^{16} electrons per cm^3. We observe that a decrease of the nanocrystal size (introduced as an input value of the simulations) leads to a transition from the Drude behavior to the localized response with the conductivity peak shifting to higher frequencies for smaller particles; in this case of isolated nanocrystals the DC mobility vanishes for particles of a finite diameter.

As we have shown in [4], for nanoparticles smaller than a particular size (defined by the material and by experimental conditions) semiclassical *Monte-Carlo* calculations are not able to provide reasonable agreement with experimental results. Also, the Monte Carlo calculations are not able to explain simultaneously the response at room temperature and at 10 K. The calculations overestimate the response compared to the experiment at low temperatures. This can be considered as a sign of the quantum nature of the charge confinement. Therefore, in order to evaluate the charge carrier mobility properly, the quantum mechanical approach must be applied.

However, the quantum Kubo formula (shown e.g., as equation 25 in [16]), which is widely used for electronic systems excited at optical frequencies, cannot be applied to the THz range since it features non-zero DC conductivity even for completely isolated nanocrystals. It follows that the whole low-frequency part of the response (i.e., for $\omega \lesssim \gamma$, where γ is the dephasing rate occurring typically in the THz or multi-THz spectral range) is not correctly predicted by the mentioned formula.

The drawback of the Kubo formula is overcome in an approach that was described in details in [85]. In a nutshell, the electron linear response to the probing (terahertz) electric field is described by two regimes: a coherent regime (electron is coherently excited by the THz field but no inelastic scattering event occurred, yet) and an incoherent regime (after the first inelastic scattering event). Unlike in bulk materials, the spatial distribution of the coherent electrons in nanostructures (i.e., in systems with broken translation symmetry) shifts with respect to the equilibrium distribution. The thermal equilibrium of the system is then achieved by the

diffusion (thermalization) current j_{th} which results from all inelastic scattering events of incoherent electrons leading to the equilibrium state.

$$j_{th} = D_{diff} \nabla n_{th}, \tag{2.26}$$

where D_{diff} is the diffusion coefficient rigorously related to the material parameters through the Einstein's relation and n_{th} is spatially inhomogeneous density of electrons. This thermalization current is not taken into account in the formula for the optical conductivity in [16]. Our model allows us to evaluate properly the carrier mobility function [85]:

$$\mu^{QM}(\omega) = \frac{1}{\mathcal{V}_{NC} N E} \int_{-\infty}^{+\infty} \mathrm{d}t \exp(-i\omega t) \times \left[\frac{1}{m_{eff}} \sum_{k,l} p_{kl} [\rho_C(t)]_{lk} + \int_{\mathcal{V}_{NC}} j_{th}(t, \mathbf{r}) \mathrm{d}^3\mathbf{r} \right], \tag{2.27}$$

where ρ_C is a density matrix component defining the coherent regime and k, l are multi-indices denoting eigenstates ($\mathcal{V}_{NC}$ is the nanocrystal volume, N is the density of carriers, E is a component of the probing electric field amplitude, p_{kl} denotes a component of the momentum operator).

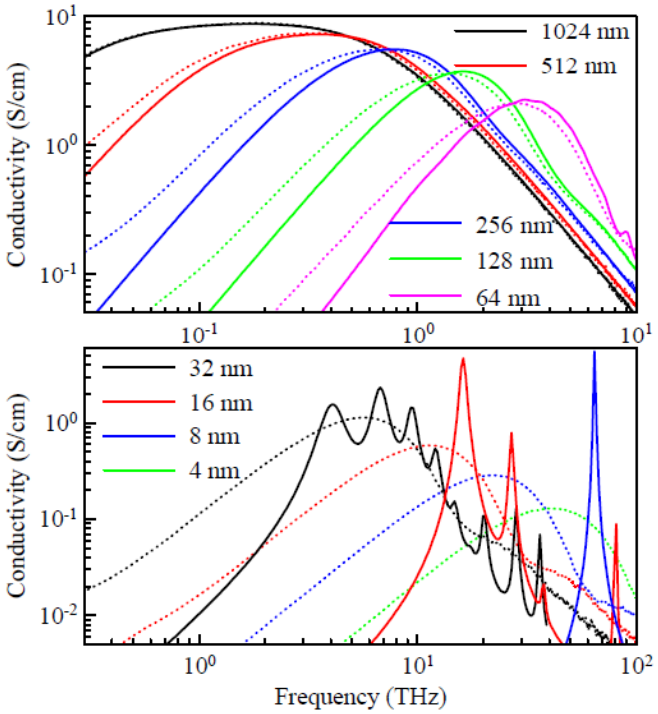

Figure 12 Quantum mechanical model (solid lines) and semiclassical *Monte-Carlo* calculations (dotted lines) of the conductivity of mutually isolated cube-shaped GaAs nanocrystals. T = 300 K and electron density $N = 10^{16}$ cm^{-3}, bulk scattering time in GaAs: 270 fs (figure 2 from [85]).

The comparison of the conductivity spectra calculated for different nanocrystal sizes by means of semiclassical *Monte-Carlo* simulations (dotted lines) and the quantum mechanical approach (solid lines) are presented in figure 12. The diffusion current is evaluated here from the diffusion equation for carriers where the diffusion coefficient is determined by the Einstein's relation ($D = k_B T/(m_{eff}\gamma)$). We observe an excellent agreement between the quantum and classical results for large nanocrystals; for a crystal size of 1024 nm the quantum and classical curves exactly coincide. If the nanocrystal size a is decreased the classical model predicts a monotonous blueshift of the conductivity peak and no sharp spectral lines are observed.

The quantum approach shows a qualitatively similar behavior down to sizes of about 60 nm. However, below this size (which corresponds to the situation where the nanocrystal size is comparable to the mean free path of electrons inside nanocrystals) signatures of transitions between the quantum levels start to appear and the overall shape of the quantum conductivity differs significantly from the classical one. Clearly, the classical calculations fail for these sizes where the quantum interferences dominate over the carrier scattering.

2.2.5. Localized plasmon and Effective medium theory

2.2.5.1 Localized plasmon

An electric field applied to nanocrystals with free carriers (more precisely, with conduction band electrons or valence band holes) leads to separation of the positive and negative charges inside the material. In this case the motion of electrons and holes driven by the probing (THz) electric field is constrained by the nanocrystal boundary and the electrostatic force pulls charges back towards their original positions. This can be understood as an effective restoring force acting on the charge carriers and, consequently, their dispersive response can be described by the damped harmonic oscillator formula [86]:

$$\sigma(\omega) = -i\omega \frac{F}{\omega_0^2 - \omega^2 - i\omega\gamma}, \tag{2.28}$$

where $F$is the oscillator strength and γ is the damping rate. A transverse (localized plasmon) resonance occurs at the frequency ω_0 which is proportional to (and smaller than) the plasma frequency ω_p of the charges. This approach is called the localized plasmon (LP) model (figure 13). It has been extensively employed to characterize the (THz) (photo-)conductivity of the materials consisting of conductive inclusions in insulating matrix. The ratio between the plasma and LP frequencies ω_p/ω_0 depends on the geometry of the conductive particles and on the dielectric properties of the materials. For high frequencies ($\omega \gg \omega_0$) LP model reduces to the Drude one.

In spite of its simplicity, interpretation of the conductivity spectra in terms of the LP model does not provide complete information about physical properties of the studied system. Indeed, along with the dielectric properties of the components, both magnitude of the carrier mobility and amplitude of the screening field collectively generated by the separated charges are entangled into the single parameter F. More explicit description of the system can be obtained via rigorous interpretation in terms of the depolarization fields. The related approach

is called effective medium approximation and it provides the mixing rules for the dielectric properties of the material compounds.

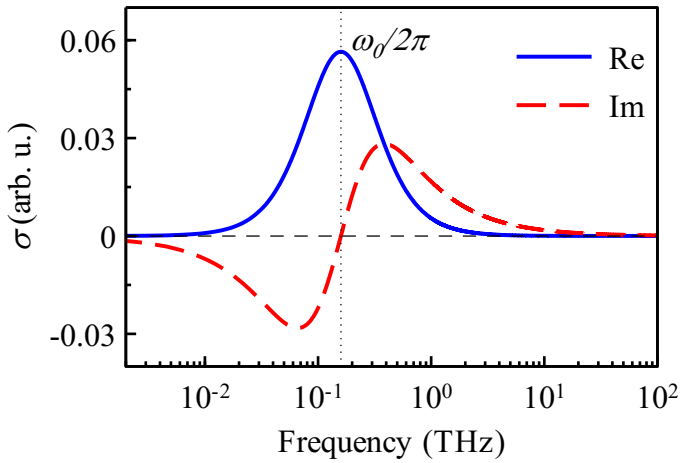

Figure 13. Localized plasmon model of the conductivity: $F = 1/\varepsilon_0$, $\omega_0/2\pi = 1$ THz and $\gamma/2\pi = 2$ THz.

2.2.5.2 Effective medium approximation

Nanostructured materials usually consist of several dielectric/semiconducting media. The response of a macroscopic composite system to the probing THz radiation can be described as a response of a homogeneous material with an effective permittivity ε_{eff}. Effective medium approximation (EMA) involves various models that allow one to find a correlation between this effective permittivity and the dielectric (or conductive) properties of each individual component. Usually, the system under investigation is made of (semi-)conducting (nanoscaled) inclusions dispersed in some insulating medium (referred to as the matrix). For a two-component system let us denote ε_m and ε_p the permittivities of the matrix and of the inclusions, respectively. Then, the main objective of the EMA is to find the form of a function $f_{eff}(\varepsilon_m, \varepsilon_p, ..)$, so that

$$\varepsilon_{eff} = f_{eff}(\varepsilon_m, \varepsilon_p, ..). \tag{2.29}$$

An important assumption of the effective medium approximation is that the size of the inclusions must be significantly smaller than the wavelength of the probing radiation (which is fulfilled for the THz probing of nanostructures). In this case, the electromagnetic field is approximated as homogeneous in each individual nanocrystal (inclusion). The separation of the positive and negative charges under the applied electric field produces depolarization fields *inside* the inclusions, which screen the field E applied to the sample. Carriers inside the inclusions then move in response to the local field $E_{loc}$and not in response to the applied field (E_{THz}in our experimental case). Effective medium theories then evaluate the relation between E_{THz} and E_{loc} and thus the relation between the microscopic (local) and the measured effective dielectric properties of the composite.

From the point of view of the field distribution in the composite material, it is fair to say that a system of an inclusion with the permittivity $\varepsilon_1/\varepsilon_2$ in vacuum is equivalent to a system of an inclusion with the permittivity ε_1 in a matrix with a permittivity ε_2. We assume here an

isotropic case where all the quantities can be treated as scalars. In the following chapters we review the basic effective medium theories (EMTs) and describe the model that we use for evaluating the spectra of the THz photoconductivity.

2.2.5.3. Maxwell-Garnett EMT model

One of the oldest effective medium theory is the *Maxwell-Garnett* model (MG) [87,88], which describes one component inclusions randomly dispersed in a matrix. An important assumption of the model is that the distance from one particle to another is much larger than the particle size. It corresponds to the case of non-percolated inclusions in a percolated matrix. The relation among the effective and local dielectric properties is defined using the so-called MG shape factor K and the filling factor of the inclusions s as follows:

$$\varepsilon_{eff} = \varepsilon_m \frac{\left(\varepsilon_p(1+Ks) + \varepsilon_m K(1-s)\right)}{\varepsilon_p(1-s) + \varepsilon_m(K+s)}. \tag{2.30}$$

The parameter K reaches large values for the oblong structure when the field is parallel to its long dimension. MG model can be well applied to the composites with small values of s. This model is relatively simple and widely used to describe composites, where the component 1 is non-percolated.

Upon photoexcitation the permittivity of the inclusions changes due to the photoconductivity. The effective permittivity than changes in an analogous manner:

$$\varepsilon_p \rightarrow \varepsilon_p + \frac{i\Delta\sigma_p}{\omega\varepsilon_0} \quad => \quad \varepsilon_{eff} \rightarrow \varepsilon_{eff} + \frac{i\Delta\sigma_{eff}}{\omega\varepsilon_0}. \tag{2.31}$$

Our aim is to find the relation between the effective photoconductivity $\Delta\sigma_{eff}$ and the local phoetoconductivity $\Delta\sigma_p$. Let us make these substitutes in 2.30:

$$-\frac{i\Delta\sigma_{eff}}{\omega\varepsilon_0} = \varepsilon_m \frac{\varepsilon_p(1+Ks) + \varepsilon_m K(1-s) + \frac{i\Delta\sigma_p}{\omega\varepsilon_0}(1+Ks)}{\varepsilon_p(1-s) + \varepsilon_m(K+s) + \frac{i\Delta\sigma_p}{\omega\varepsilon_0}(1-s)} - \varepsilon_{eff}, \tag{2.32}$$

which yields

$$\Delta\sigma_{eff} = \Delta\sigma_p \frac{\varepsilon_m(1+Ks) + \varepsilon_{eff}(1-s)}{\varepsilon_p(1-s) + \varepsilon_m(K+s) + \frac{i\Delta\sigma_p}{\omega\varepsilon_0}(1-s)} = \Delta\sigma_p \frac{A}{B + \frac{i\Delta\sigma_p}{\omega\varepsilon_0}}. \tag{2.33}$$

where we denote $A = \varepsilon_m(1+Ks)/(1-s) + \varepsilon_{eff}$ and $B = \varepsilon_p + \varepsilon_m(K+s)/(1-s)$. Thus, in the case of the Drude conductivity (equation 2.18) in the inclusions, the equation 2.33 leads to the following expression for the effective conductivity:

$$\Delta\sigma_{eff} = i\varepsilon_0\omega\frac{A\omega_p^2}{B}\frac{1}{\frac{1}{B}\omega_p^2 - \omega^2 - i\omega/\tau}. \quad (2.34)$$

Note that this expression corresponds to the localized plasmon model (equation 2.28). The restoring force corresponds to the screening of the applied field while the carrier scattering time defines the damping of the system. The advantage of this approach, however, is that all the parameters are defined via the dielectric and geometrical properties of the system and the photocarrier density is explicitly included in the expression for the plasma frequency. equation (3.31) then predicts how the localized plasmon scales with the pump beam fluence.

2.2.5.4. Bruggeman EMT model

Another EMT, which can be applied to the systems of two either percolated or non-percolated components, is the *Bruggeman* model [89]. This approach considers both components as inclusions of a medium 1 (ε_1) and a medium 2 (ε_2) dispersed in a matrix of the effective medium (ε_{eff}). In contrast to the MG model, such consideration treats the components 1 and 2 symmetrically and leads to the following expression for the effective permittivity:

$$s\frac{\varepsilon_1 - \varepsilon_{eff}}{\varepsilon_1 + K\varepsilon_{eff}} + (1-s)\frac{\varepsilon_2 - \varepsilon_{eff}}{\varepsilon_2 + K\varepsilon_{eff}} = 0. \quad (2.35)$$

The *Bruggeman* model is able to take into account the percolation thresholds of both components. The disadvantage of this approach is that the percolation thresholds are mathematically bond to some particular values of the filling fraction *s* for a given shape of inclusions. It excludes the possibility to tune the filling fraction corresponding to the threshold.

2.2.5.5. Bergman EMT model

The two models described above can be found as specific cases of the most general *Bergman EMT* for two-component systems. *Bergman* theorem overcomes the limits of the *Maxwell-Garnett* and *Bruggeman* theories, being able to describe composites with complex percolation pathways and with variety of shapes of the inclusions by means percolation strength parameters V_m and V_p of the two components and by the so-called spectral function $v(N)$ [90]:

$$\varepsilon_{eff} = V_m\varepsilon_m + V_p\varepsilon_p + \int_0^1 \frac{v(N)\varepsilon_m\varepsilon_p}{N\varepsilon_p + (1-N)\varepsilon_m}\mathrm{d}N. \quad (2.36)$$

$V_m$and V_p have the meanings of volume filling fractions of the percolated parts of the matrix and inclusions, respectively. The integral over a variable N $(0 < N < 1)$ describes the contribution of the non-percolated inclusions of all possible shapes. The spectral function then has a meaning of the relative weight of various shapes of inclusions. Hence, the normalization conditions of the spectral function *v(N)* and the filling fraction *s* with respect to the total volume of the sample must be fulfilled:

$$V_m + V_p + \int_0^1 v(N)\mathrm{d}N = 1,$$

$$V_p + \int_0^1 (1-N)v(N)\mathrm{d}N = s, \tag{2.37}$$

$$V_m + \int_0^1 Nv(N)\mathrm{d}N = (1-s)$$

The spectral function $v(N)$ characterizes the density of the non-percolated inclusions with different shapes and does not depend on their dielectric properties. The parameter *N* is related to the shape factor of the inclusions. Indeed, if the permittivity $\varepsilon_p$or ε_m is negative, then the denominator vanishes for a particular value of *N*, which, in fact, corresponds to a localized plasmon resonance condition for an inclusion characterized by *N*. The spectral function *υ(N)* then plays a role of an oscillator strength distribution for inclusions of various shapes.

Despite the ability of the *Bergman* theory to describe two-component materials with any complex morphology, the model in its general form is quite rarely employed to analyze experimental data. It is due to the fact that the correct form of the spectral function of real composites with a continuous distribution of the *N* factor is hard to obtain. An important approximation of the *Bergman* model, which can be applied to a large class of composites, is an assumption of a single dominant depolarization factor $n(v(N) = v_i\delta(N-n))$, which yields

$$\varepsilon_{eff} = V_m\varepsilon_m + V_p\varepsilon_p + v_i\frac{\varepsilon_m\varepsilon_p}{n\varepsilon_p + (1-n)\varepsilon_m}. \tag{2.38}$$

The next chapter is devoted to the EMT approach based on this approximation. It was developed in our group and it is extensively used in this work for characterization of the photoinduced conductivity of the samples.

2.2.6. VBD EMT model

From the practical point of view, it is useful to have an EMT that is applicable to both non-percolated and percolated samples with complex morphology and that is able to describe complex percolation pathways. The model must also satisfy specific requirements related to an applied experimental technique. In particular, OPTP THz spectroscopy (1.2.1) demands the following properties of the model:

- effective permittivity/conductivity dependence on the photoexcitation density must be carefully taken into account;
- it should cover various experimental situation, i.e., both thin and thick samples with the different optical penetration depth;
- transient THz signal should obey the wave equation (2.6);
- the model must consider an in-depth profile of the photoexcitation $\Delta\sigma_{eff}(z)$.

Using the numerical approach, it was shown in [2] that for a broad geometrical variety of the structures the photoinduced conductivity can be well described by means of the *Bergman* EMT (section 2.2.5.5) in approximation of a dominant peak for one depolarization factor N_i (equation 2.38). In brief, finite element method for solving quasi-static Maxwell equations was employed to calculate numerically an electric field E distribution over some given unit cell consisting of nanoparticles in an insulating matrix with external electric field applied in a particular direction. The calculations were performed for the nanoparticles forming structures of various geometry i.e., both regular (spherical) and irregular particles with a different number, shape and length of the percolation pathways (figure 14).

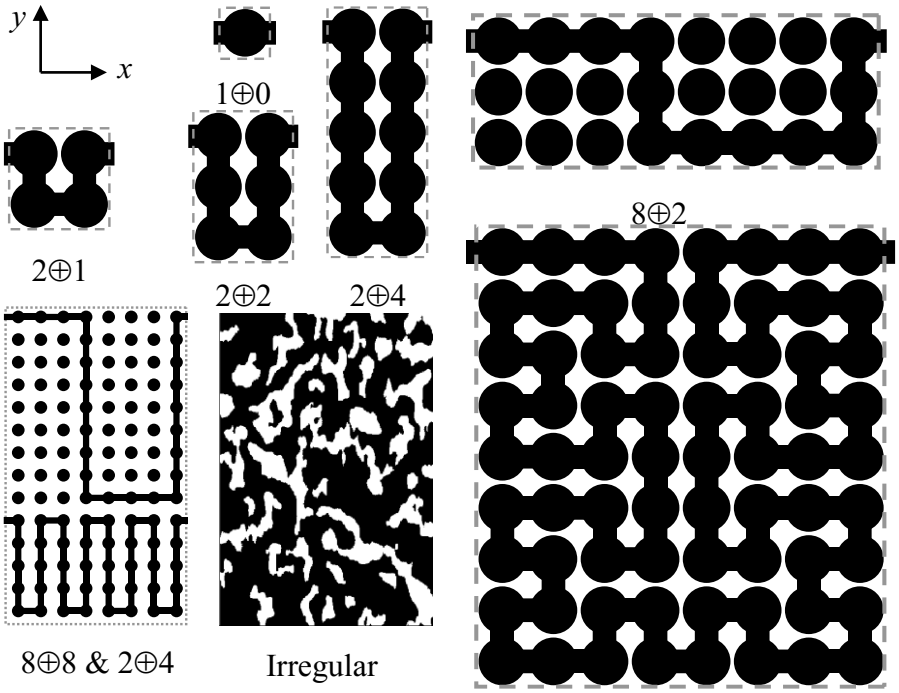

Figure 14. Examples of the unit cells of simulated structures; white part corresponds to the dielectric matrix; black color illustrates particles (Selected from figure 1 in [2]).

In terms of the effective medium, the electrostatic energy integrated over the volume of the unit cell for the calculated distribution of the electric field $\boldsymbol{E}(x, y)$ should correspond to the energy of the associated effective medium described by ε_{eff} and a homogeneous field obtained as an average over the unit cell. Thus, the following averaging over the volume of the unit cell V must hold:

$$\frac{1}{2V}\iint_V \varepsilon_{mic}(x,y)E^2(x,y)\mathrm{d}x\mathrm{d}y = \frac{1}{2V}\varepsilon_{eff}\left[\iint_V E(x,y)\mathrm{d}x\mathrm{d}y\right]^2. \tag{2.39}$$

Depending on the value of the coordinates x and y, $\varepsilon_{mic}(x,y)$ describes the microscopic permittivity of the particles ε_p or of the matrix ε_m. The effective (macroscopic) permittivity is presented by the calculated parameter ε_{eff} at the right-hand side. Photoexcitation of the nanoparticles was modeled by addition of the imaginary parameter $i\Delta\varepsilon''_{mic}$ with a subsequent calculation of $\Delta\varepsilon_{eff}$ as a function of "photoexcitation" $i\Delta\varepsilon''_{mic}$.

Based on the above, a general EMT model for the photoexcited semiconductor-based nanostructures was proposed in our group by Ivan Rychetský, Hynek Němec and Petr Kužel [2,68] as a specific case of the *Bergman* model for a single dominant depolarization factor (equation 2.38). It has been shown that the photoinduced (transient) effective permittivity $\Delta\varepsilon_{eff}$ can be defined by a simple expression as:

$$\Delta\varepsilon_{eff} = V\Delta\varepsilon_{mic} + \frac{B\Delta\varepsilon_{mic}}{1 + D\Delta\varepsilon_{mic}} \tag{2.40}$$

and, taking into account 2.31, in terms of the conductivity as:

$$\Delta\sigma_{eff} = V\Delta\sigma_{mic} + \frac{B\Delta\sigma_{mic}}{1 + \frac{iD\Delta\sigma_{mic}}{\omega\varepsilon_0}}. \tag{2.41}$$

These simple expressions constitute the relation between the effective (experimentally measured) and microscopic response of the sample via three parameters characterizing sample morphology: Vstands for the percolation strength (from 2.38), B and D characterize the inductance and capacitance of the non-percolated part of the sample. It has been shown that this so-called VBD model is able to describe behavior of the numerically calculated function $\Delta\varepsilon(i\Delta\varepsilon''_{mic})$ for the majority of the simulated cases (different geometry of the structures). The function $\Delta\sigma_{mic}$ defines the transient contribution to the conductivity of the photoconductive (nano)inclusions due to optical excitation, respectively.

Note the similarity of equation 3.38 with the Maxwell-Garnett expression 3.33. For the samples with isolated inclusions and a single shape factor parameter K the *VBD* model, in analogy with the *Bergman* theory, reduces to the *Maxwell-Garnett* model with the parameters V, B and D defined as:

$$\begin{aligned} V &= 0, \\ B &= \frac{\varepsilon_m(1 + sK) - \varepsilon_{eff}(1 - s)}{\varepsilon_m(1 + sK) - \varepsilon_p(1 - s)}, \\ D &= \frac{(1 - s)}{\varepsilon_m(s + K) + \varepsilon_p(1 - s)}. \end{aligned} \tag{2.42}$$

Note also that for very weak photoexcitation of the sample (small $\Delta\sigma_{mic}$) the D-term in the denominator of (2.41) can be negligible and, in this case, $\Delta\sigma_{eff} \propto \Delta\sigma_{mic}$. In other words, for sufficiently small photoexcitation the depolarization fields are very weak and the effective THz response of the sample approaches the microscopic response function of charge carriers; this is a very important point in our studies.

The VBD model can be interpreted in terms of the equivalent electric circuit. The model is discussed in [68,2] and it is based on the representation of conductive inclusions in the insulating matrix by the equivalent *RC* branches (figure 15): in the direction of the applied (static) field gaps between the inclusions are represented by the capacitor C_{np}(defined by the geometry and permittivity of the matrix), while R_{np} and R_p correspond to the resistance across the non-percolated and percolated conductive elements (related to the real part of microscopic

(photo)conductivity). The admittance of the circuit then corresponds to the effective (photo)conductivity $\Delta\sigma_{eff}$.

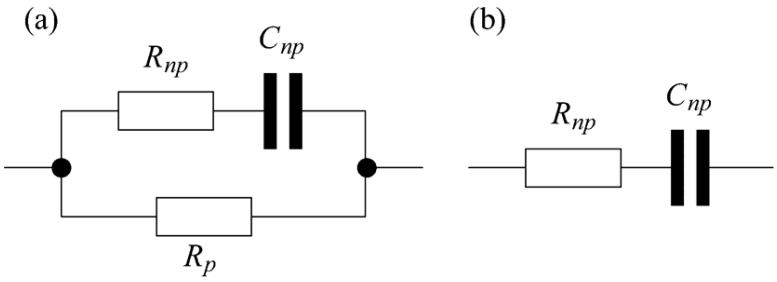

Figure 15 Examples of two the simplest electric circuits that may represent structures (a) with and (b) without percolation (figure 3 in [2]).

2.3. Solution of wave equation in nanomaterials

Solution of the wave equation 2.7 with the photoinduced conductivity $\Delta\sigma$ defined via the VBD EMT model directly provides the relation between the experimentally measured THz signal and microscopic properties of nanomaterials, which is one of the main objectives of our work. Regarding the microscopic response, the microscopic conductivity $\Delta\sigma_{mic}$ is proportional to the microscopic mobility function μ, which we define as a single carrier response function to the local electric field E_{loc}. Also, $\Delta\sigma_{mic}$ is proportional to the number of free carriers N_e. In the case of photoexcited electrons, N_e depends on the photoexcitation fluence ϕ and decays exponentially inside the sample along the direction of the optical beam propagation z following the Lambert-Beer absorption law for the pump beam. Note that the dependence of μ on the carrier density does not affect general consideration of the EMT approach. An expression for the frequency dependent microscopic conductivity function is then, in most general experimental cases, given by the expression:

$$\Delta\sigma_{mic} = e_0\xi\mu\ \phi\ \alpha_{loc}e^{-\alpha z} = \Delta\sigma_0 e^{-\alpha z}, \tag{2.43}$$

where ξ is a quantum yield of the mobile charge generation (how many photons generate one electron), α_{loc} is the optical absorption coefficient of semiconductor inclusions and α is the effective optical absorption of the sample. The exponential term in 2.43 describes the optical excitation of the sample co-propagating with the transmitted THz probing beam.

2.3.1. Transient Transmission function

The effective conductivity described by the VBD model 2.41 is defined as a linear combination of the terms corresponding to the percolated and non-percolated parts of the system. Therefore, it is convenient to present separately the corresponding solutions of the wave equation since these solutions are quite complex. The analytical approach described in the section 2.1.1 provided us with the solutions for the transient transmitted (ΔE_t) and reflected (ΔE_r) THz fields. Thus, defining the photoconductivity $\Delta\sigma$ in the equation 2.13 via 2.41 and 2.43, the percolated (ΔE^P) and non-percolated (ΔE^{NP}) parts of the transient transmission function (equation 2.15) can be calculated (equations 22 and 30 in [68]) as follows:

$$\frac{\Delta E_t{}^P}{E_t} = -\frac{Z_0}{2n}\frac{\Delta\sigma_0}{\alpha}aV \times \left[\left(1 + r_1 r_2 e^{2ikL}\right)\left(1 - e^{-\alpha L}\right) + r_1\frac{1 - e^{2ikL}e^{-\alpha L}}{1 - 2ik/\alpha} + r_2\frac{e^{2ikL} - e^{-\alpha L}}{1 + 2ik/\alpha}\right], \tag{2.44}$$

$$\frac{\Delta E_t^{NP}}{E_t} = -\frac{Z_0}{2n}\frac{\Delta\sigma_0}{\alpha}aB \times \left[\left(1 + r_1 r_2 e^{2ikL}\right)\frac{Ln(1 + Y_0) - Ln\left(1 + Y(L)\right)}{Y_0} + r_1\left\{F(1 - 2ik/\alpha\,, Y_0) - e^{2ikL}e^{-\alpha L}F(1 - 2ik/\alpha\,, Y(L)\,)\right\} + r_2\left\{F(1 + 2ik/\alpha\,, Y_0)e^{2ikL} - e^{-\alpha L}F(1 + 2ik/\alpha\,, Y(L)\,)\right\}\right], \tag{2.45}$$

where

$$Y(z) = Y_0 e^{-\alpha z} = i\frac{D}{\omega\varepsilon_0}\Delta\sigma_0\, e^{-\alpha z} \tag{2.46}$$

and F introduces the Gaussian hypergeometric function [91]:

$$F(\kappa, Y) = \frac{{}_2F_1(1, \kappa, 1 + \kappa; -Y)}{\kappa}. \tag{2.47}$$

Depending on the optical thickness of samples, general formulas (2.44) and (2.45) might be significantly simplified as it was shown in [68].

The macroscopic THz response of the materials depends on the photoexcitation fluence ϕ. Therefore, it has been shown [68, 2] that it is convenient to express experimental output of the OPTP measurements in the form of a so-called normalized transmission function:

$$\Delta T_{norm} = -\frac{n_1 + n_2}{Z_0}\frac{1}{e_0\phi}\frac{\Delta E_t}{E_t}. \tag{2.48}$$

For percolated samples or for a sufficiently low density of the charge carriers in non-percolated samples this function has meaning of the microscopic mobility μ.

2.3.2. Transient Reflection function

Following the same considerations as in the previous section, the solution of the wave equation for the transient reflection function ΔR (2.15) for the case of the effective conductivity described by the VBD model was presented in [69], where, according to the experimental geometry, the exponential decay of the photoinduced conductivity was also described as in 2.43 (copropagating pumping and THz beams). In the current work we would like to present the expression related to the THz reflectivity measurements of silicon nanocrystals

superlattices described in section 4. In that study the sample was optically excited from the backside, i.e. the photoexcitation beam co-propagates with the reflected probing THz beam. The corresponding decay of the microscopic photoconductivity function reads:

$$\Delta\sigma_{mic} = e_0 \xi \mu \, \phi \, \alpha_{loc} e^{-\alpha(L-z)} = \Delta\sigma_0 e^{-\alpha(L-z)}, \tag{2.49}$$

where L is the sample thickness. This leads to the following solution for the percolated ΔR^P and non-percolated ΔR^{NP} parts of the transient reflectivity function:

$$\begin{aligned}\frac{\Delta E_r^P}{E_r} = &-\frac{Z_0 t_1^2 a}{2n_1(r_2 e^{2ikL} - r_1)} \frac{\Delta\sigma_0}{\alpha} V \\ &\times \left[\frac{1}{2ik/\alpha + 1} \left(e^{2ikL} - e^{-\alpha L}\right) + 2r_2 e^{2ikL}(1 - e^{-\alpha L}) \right. \\ &\left. + \frac{\left(r_2 e^{2ikL}\right)^2}{-2ik/\alpha + 1} \left(e^{-2ikL} - e^{-\alpha L}\right) \right],\end{aligned} \tag{2.50}$$

$$\begin{aligned}\frac{\Delta E_r^{NP}}{E_r} = &-\frac{Z_0 t_1^2 a}{2n_1(r_2 e^{2ikL} - r_1)} \frac{\Delta\sigma_0}{\alpha} B \\ &\times \left[2r_2 e^{2ikL} \left(\frac{Ln(1 + Y_0)}{Y_0} - \frac{Ln\left(1 + Y(L)\right)}{Y_0} \right) \right. \\ &+ \{e^{2ikL} F(1 + 2ik/\alpha, Y_0) - e^{-\alpha L} F\left(1 + 2ik/\alpha, Y(L)\right)\} \\ &+ \left(r_2 e^{2ikL}\right)^2 \{e^{-2ikL} F(1 - 2ik/\alpha, Y_0) \\ &\left. - e^{-\alpha L} F\left(1 - 2ik/\alpha, Y(L)\right)\} \right].\end{aligned} \tag{2.51}$$

2.4. Summary

Since chapter 3 is quite long, we provide here a short recapitulation of the main results and we propose a scheme (protocol) for the data measurement and analysis following these findings. We used this scheme for data acquisition and handling throughout this thesis.

First, the transient data are acquired and we evaluate the experimental spectra $\Delta E_t/E_t$ and $\Delta E_r/E_r$ for the transmission or reflection experiment, respectively. In the case of the transmission experiment in a thin film, the quantity ΔT_{norm} is evaluated using equation 2.48 since this quantity was shown to be comparable to the mobility. Importantly, ΔT_{norm} is measured for a broad range of pump fluences ϕ (carrier concentrations N_e), typically over 2 or 3 orders of magnitude. As it has been pointed out above, the effective THz response of the sample approaches the microscopic response function for sufficiently small photocarrier concentrations.

The interpretation starts with a suitable choice of the microscopic mobility model, equations 2.18–2.27. In this work we use the Drude model of the microscopic mobility (section

2.2.1) for the response associated to charge carriers moving freely, whereas either Monte-Carlo or Quantum calculations of the microscopic mobility (section 2.2.4) are employed in the case of the carrier confinement.

The microscopic mobility is introduced into the right-hand-side of the wave equation through the VBD formula (equation 2.41); the corresponding small-signal ($\Delta E \ll E$) analytical solutions of the wave equations have been presented as equations 2.44, 2.45 for the transmission experiment and 2.50, 2.51 for the reflection experiment. The theoretical spectra $\Delta E_t/E_t$ or $\Delta E_r/E_r$ are finally fitted to the experimental ones. Alternatively, in the cases where the small-signal condition cannot be achieved in the experiment over the whole spectral range, we calculate numerical solution of the wave equation (2.7) and this numerical solution is fit to the experimental data.

The described strategy allows us to evaluate carefully the charge transport within a sample and/or a single nanostructure. In addition, it enables an access to the parameters of the sample morphology such as the size of structures, their shape and mutual disposition. A deep understanding of the THz photoconductive response may be achieved by combination of several THz techniques (section 1.2) with electron and atomic force microscopy (section 3).

3. Experimental setups

In our investigations we employed several THz systems based on the various THz generation and detection principles (section 1.2) and various laser sources. Since the majority of these systems is custom-built, we provide their detailed description and characteristics in this chapter. Apart from the THz experiments, some supporting experiments have been carried out using commercial devices: Fourier transform infrared spectrometer (FTIR) *BRUKER IFS113v* was used for the analysis of the mid-infrared response of Si nanocrystal superlattices reported in section 4; scanning electron microscope (SEM) FEI Quanta 3D FEG and atomic force microscope (AFM) Asylum Research Cypher S were employed for the morphology characterization of the GaAs nanobars described in section 5; for optical microscopy of our samples we used optical polarization microscope Leica DM2700 M equipped with Leica DMC2900 camera.

3.1. Setup for Optical Pump – THz probe experiment

A scheme of the experimental setup used for OPTP spectroscopy is shown in figure 16. A Ti:sapphire regenerative amplifier (Spitfire ACE, Spectra-Physics/Newport) is used as a laser source of the experiment with 1 mJ pulse energy, 5 kHz repetition rate, ~ 40 fs pulse length and central wavelength λ = 800 nm. The fundamental beam is split into three beams by means of 800 nm beam splitters: ~ 0.3 mJ pulses are used for THz generation (probing beam) and detection (sampling beam); the remaining part serves for the photoexcitation of the sample (pumping beam).

Generation of the THz pulses is performed via optical rectification of the probing beam pulses in a 1 mm thick nonlinear (110)-ZnTe crystal. The generated linearly polarized divergent THz beam is collected using elliptical aluminum mirror and focused onto the sample position. Then, by means of a second elliptical mirror, it is focused onto another 1 mm thick ZnTe crystal used as a sensor. The THz part of the experimental setup is enclosed in an aluminum vacuum chamber in order to avoid absorption of the THz radiation on water vapor. The chamber is evacuated to a pressure of about 1 mbar using a primary vacuum pump. The sample is attached to the front side of a metal holder with a circular aperture. It is positioned either directly inside the vacuum chamber or inside a continuous-flow optical cryostat (Oxford Optistat) introduced into the vacuum chamber for the measurements at the low temperature.

The sampling beam is sent to the sensor crystal collinearly with the THz beam by means of a THz transparent pellicle mirror. The birefringence of the non-linear crystal, induced by the THz pulses through the linear electro-optic effect, is proportional to the instantaneous value of the THz electric field. Thus, simultaneous presence of the THz and sampling pulses results in a polarization change of the sampling beam. Subsequently, the polarization of the optical pulses is transformed into the circular/elliptical one by means of a Babinet-Soleil compensator acting as a quarter-wave plate. The Wollaston prism splits the sampling beam into orthogonal linearly polarized components. The difference between the intensities (I_P and I_S) of these two components, measured by two photodiodes, is linearly proportional to the value of the THz

field inside the sensor crystal which was sampled by the optical pulse. Phase-sensitive synchronized detection is accomplished by utilizing a lock-in amplifier and an optical chopper introduced into the probing beam path. The signal-to-noise ratio is further increased by employing a gated integrator for the processing of the signal from the photodiodes. The time delay of the sampling pulse with respect to the THz pulse is controlled by a delay line with a 3 fs resolution time. The basic characteristics of our OPTP THz setup are summed up in a table 1.

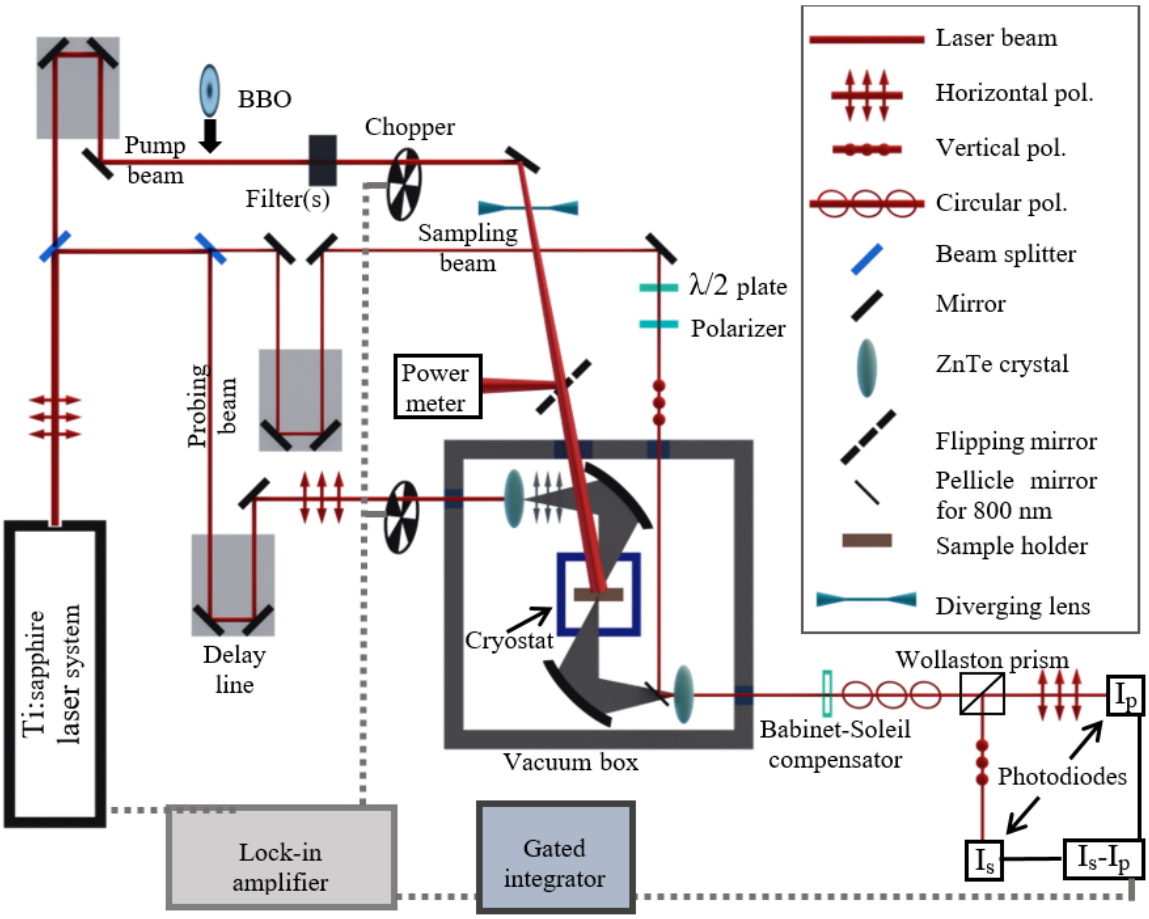

Figure 16. Scheme of the OPTP experimental setup.

Depending on the material, the photoexcitation of the sample may be performed using the photons at the fundamental wavelength (800 nm) as well as photons converted to higher harmonics. Either single or a sequence of two phase matched BBO crystals is introduced to generate the second or third harmonic, respectively.

The angle of incidence of the pumping beam on the sample plane is about 10 degrees. The beam is defocused via a CaF_2 plano-concave lens in order to achieve nearly homogeneous excitation density of the sample measured area. The excitation power is controlled via variation of the neutral density filters and variable polarizing attenuator. The power of the pumping beam is measured with a power meter; in situ power measurements are quite complicated in the vacuum chamber conditions. Therefore, the pumping beam may be deflected to the power meter outside the chamber using the flipping mirror. However, due to the different path distances of the divergent beam and absorption by the employed windows, this approach

requires preliminary measurements of the proportionality coefficient between the beam power at the power meter position and at sample surface. The photon fluence incident on the front surface of the sample is then defined by the following expression:

$$\phi = P_{inc}/(\frac{hc}{\lambda} f_{rep} \pi r^2), \tag{3.1}$$

where P_{inc} is the average power of the beam incident on the sample surface, h is the Plank constant, f_{rep} is the repetition rate and r is the radius of the sample holder aperture.

The scan range of a time delay line used for the excitation beam is 1000 ps with the time resolution of 3 fs. Modulation of the excitation beam (i.e. introducing the optical chopper in the beam path) allows direct measurement of the transient THz signal ΔE.

Spectral range (THz)	Spectral resolution (THz)	Temperature range (K)	Peak THz field (kV/cm)
0.2 – 2.4	0.1	4 – 320	∼ 5

Table 1. Characteristics of the OPTP experimental setup.

3.2. Setup for Optical Pump – Multi-THz probe experiment

Our optical pump – multi-THz TDS setup is driven by the same laser source as the OPTP experiments described in the previous section. (Ti:sapphire regenerative amplifier Spitfire ACE, Spectra-Physics/Newport; 1 mJ pulse energy, 5 kHz repetition rate, ~ 40 fs pulse length, and the central wavelength λ = 800 nm). The custom-built spectrometer utilizes two-color mixing in plasma and the ABCD detection scheme (section 1.2.2).

The output of the femtosecond amplifier (about 400 μJ) is focused with a lens (f = 150 mm) and this convergent beam passes through a frequency doubler (200-μm-thick β-BBO), a 700-μm-thick α-BBO time plate (with fine orientation tuning in order to achieve a phase match of 800 and 400 nm waves at the common focal point) and a dual wavelength 800+400 nm half-wave plate (DWHW). The generated horizontally polarized multi-THz beam is focused on the sample position using an ellipsoidal mirror. Subsequently, using a pair of parabolic mirrors, it is focused collinearly with another 800 nm beam (<100 μJ) to a spot between two 1-mm-thick electrodes with a gap of 1 mm between them. The electrodes are supplied with 1.5 kV bias pulses at 500 Hz synchronized with the laser pulses, which superimpose to the THz field. A generated second harmonic (400 nm) is sent into an avalanche photodiode and detected using a lock-in amplifier synchronized with the bias pulses. This provides a signal directly proportional to the THz field. The THz part of the experiment is enclosed into dry air atmosphere. The sample is attached to the front side of a metal holder with a circular aperture.

The part of the fundamental beam used for the sample photoexcitation undergoes the power adjustments via neutral density filters and the variable polarizing attenuator. Its power is measured directly at the sample holder position. A sequence of the BBO crystals may be introduced into the beam path in order to use higher harmonics for optical excitation. The angle of pumping beam incidence on the sample plane is about 10 degrees. The time delay of the

optical beam is controlled by a delay line with the scan range of 660 ps and with the time resolution of 3 fs.

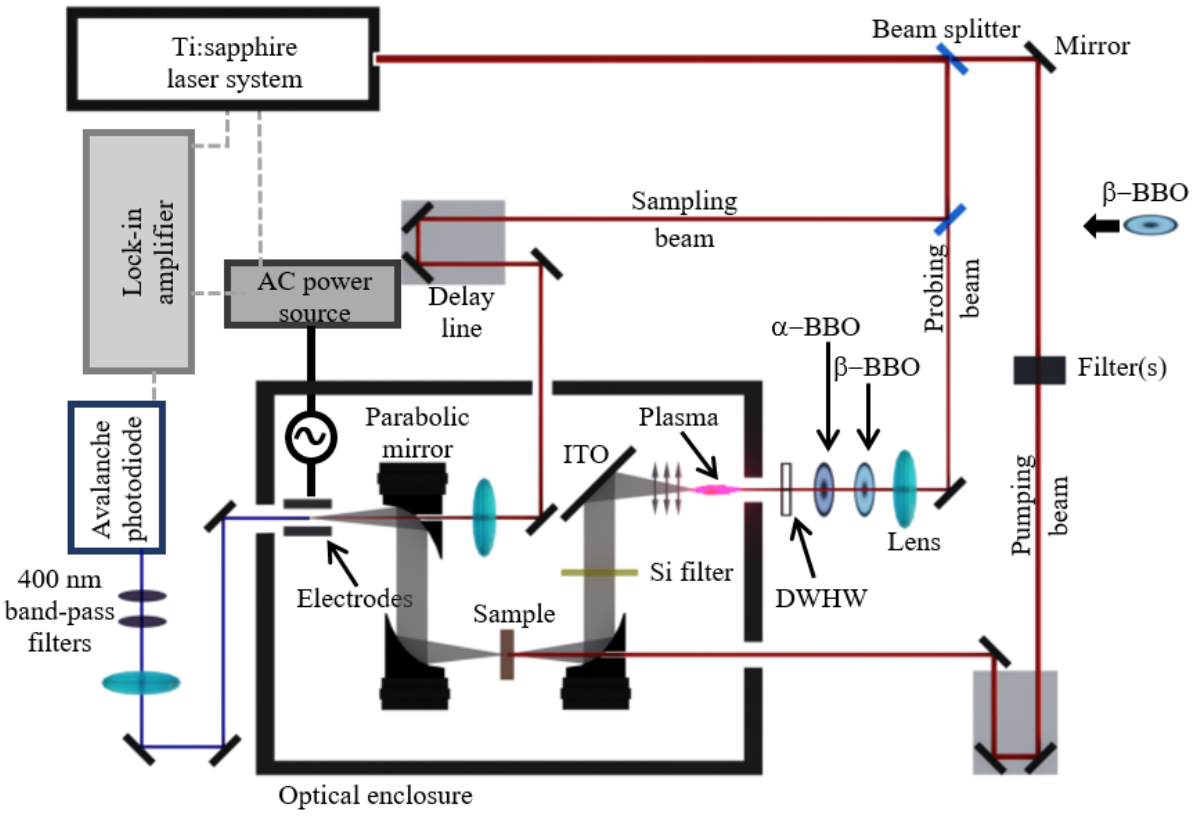

Figure 17. Scheme of the optical pump – multi-THz TDS experimental setup. In the picture ITO is an indium–tin–oxide-coated glass.

Spectral range (THz)	Spectral resolution (THz)	Temperature range (K)	Peak THz field (kV/cm)
1 – 20	0.1	300	~ 70

Table 2. Characteristics of the optical pump – multi-THz experimental setup. Peak THz field at sample position is about 70 kV/cm, at the detection position (between the electrodes) it is 120 kV/cm.

3.3. Setup for Multi-THz –mid-Infrared pulsed experiment

In our investigations we used the experimental setup for the multi-THz – mid-infra-red pulsed spectroscopy shown on figure 18 (built in the group of prof. Dr. Hartmut Roskos in Goethe University, Frankfurt). The experimental system is based on the Ti:sapphire regenerative amplifier (Clark-MXR CPA-2101) with 1 mJ pulse energy, 1 kHz repetition rate, ~ 150 fs pulse length and central wavelength λ = 775 nm. Laser pulses used for the THz generation (probing beam) undergo spectral broadening via a commercial hollow-core fiber compressor (Femtolasers KALEIDOSCOPE, containing Ar at 3.5 atm, length 1 m) followed by a sequence of negative-dispersion mirrors in order to obtain sub-20 fs duration. Subsequently, the obtained optical pulses are focused through the 150 μm thick β-BBO crystal

in order to achieve coherent generation of broadband multi-THz pulses (15 – 120 THz) via two-color air plasma laser mixing process (section 1.2.2).

A normal incidence reflection geometry for the THz probe pulse on the sample is used; the THz radiation reflected from the sample surface passes through a Si beam splitter and it is focused collinearly with a sampling pulses on a 0.5 mm thick (100)-oriented ZnTe crystal used for optical-THz sum-frequency generation (SFG). An SFG spectrogram is measured by a commercial spectrometer (Ocean Optics, QE65000). The THz part of the experiment is enclosed into dry air atmosphere. The sample is attached to the front side of a metal holder with a circular aperture.

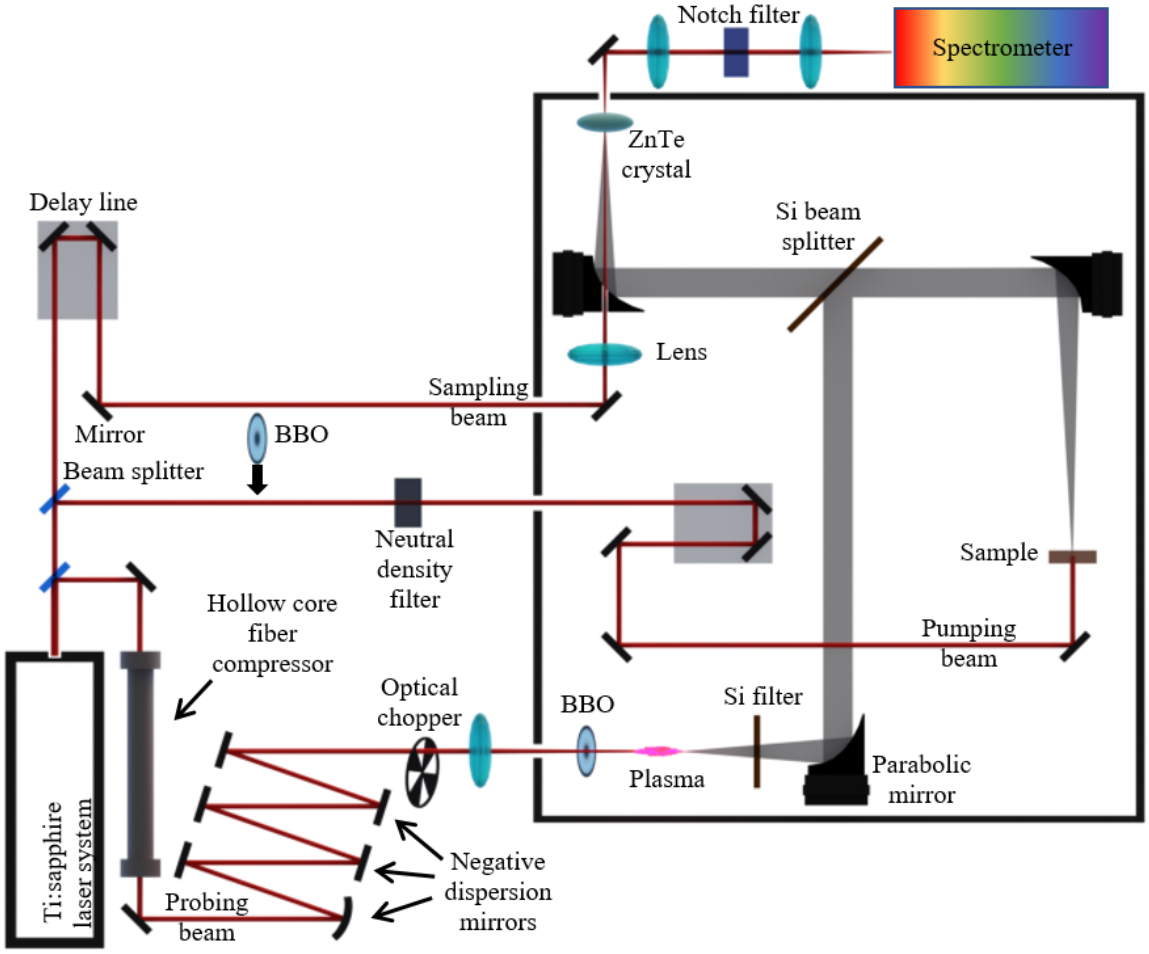

Figure 18. Scheme of the experimental setup for the multi-THz – mid-infra-red pulse spectroscopy.

The part of the fundamental beam used for the sample photoexcitation undergoes the power adjustments via neutral density filters. Its power is measured outside the enclose. Therefore, preliminary measurements/calculations of the coefficient of proportionality between the incident beam powers at the power meter position and sample surface are required. A sequence of BBO crystals may be introduced into the beam path in order to use higher harmonics for optical excitation. The pump pulses are controlled by the time delay line and delivered to the back face of the sample with a counterpropagating THz pulses.

3.4. THz Scanning Near-Field Optical microscope (THz-SNOM)

In our laboratory we use commercial THz scanning near-field microscope neaSNOM (NeaSpec) for the investigation of local conductivity. The system operates with broadband THz pulses (0.2 to 1.5 THz) scattered on a PtIr AFM tip (40 nm radius) oscillating at a particular frequency, roughly $50 - 100$ kHz. The common setup for steady-state imaging involves THz generation and detection in InGaAs photoconductive antennas driven by femtosecond Er-doped fiber laser (Menlo systems, central wavelength 1560 nm). We introduced an additional optical branch at 780 nm (second harmonic of the fundamental fiber laser output) serving for the photoexcitation of the sample using an SHG module (MenloSystems, 50 nJ pulse energy, 100 MHz repetition rate, <100 fs pulse length). The basic scheme of the experiment is shown in figure 19.

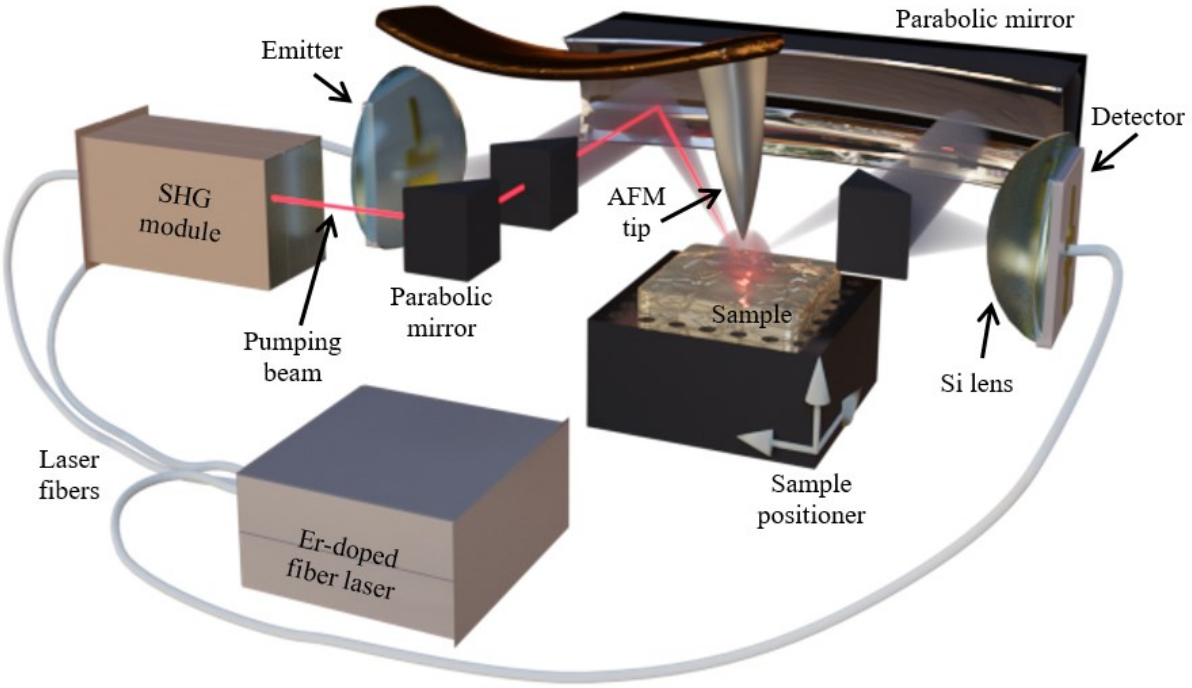

Figure 19. Scheme of the THz scanning near-field microscope neaSNOM (NeaSpec).

4. THz photoconductivity in Si nanocrystals networks

Silicon nanocrystals (NCs) [92] possess properties that find applications in various fields including photovoltaics [93], optoelectronics [94], and biosensing [95]. Deep understanding of the charge carrier transport in NCs and NC networks, namely in correlation with technological steps during the material preparation (including post-growth treatment like passivation of interfaces), can further increase their application potential.

The Si NCs prepared by thermal decomposition of silicon rich SiO_x layers have been extensively studied in the past by THz spectroscopic techniques. The THz conductivity spectra of thick layers (~0.2–1 μm; $0.2 \leq x \leq 1.4$) containing randomly distributed Si NCs were investigated previously by other groups and the results were interpreted within the framework of phenomenological Drude-Smith model [80,96,97]. Note that those thick-layer samples were characterized by a broad size distribution and by a complex NCs networking in all three dimensions. A better control over the NC size and filling fraction is obtained in multilayers composed of ultra-thin SiO_x/SiO_2 bilayers where Si NCs are formed in the Si-rich layers by thermal decomposition of SiO_x [98,99]; nevertheless, it has been shown by THz conductivity measurements [24] that even in this case non-negligible amount of NCs aggregate to larger clusters with electrical connectivity depending on the fabrication conditions.

In this chapter we study the charge carrier transport in Si NCs networks with various degrees of percolation prepared by thermal decomposition of SiO_x/SiO_2 bilayers. It turns out that the THz conductivity behavior at low temperatures (LTs) can be explained only by assuming the quantum behavior of electrons inside NCs. Indeed, quantum effects like discretization of energy levels and the corresponding appearance of resonances in the mid-infrared spectra are expected in nanometer-sized NCs. For this reason, interpretation of the experimental data within the framework of classical theories without direct incorporation of quantum effects may be questionable. Therefore, the quantum model of NC conductivity in the THz spectral range [85] was introduced and used for the first time to interpret the experimental data. Our advanced analysis based on the EMT then allows us to determine microscopic parameters of the samples, namely the distribution of sizes of NCs that participate to the conductive response of SiO_x layers. We show and justify that such conductivity-weighted distribution may differ from the size distribution obtained e.g. by standard analysis of transmission electron microscopy images.

Basically, spectroscopy in the standard THz range (up to 3 THz) is not sensitive to the transport of charge carriers in NCs with sizes comparable to the layer thicknesses (i.e. typically of 4–5 nm), which are supposed to be formed in the samples, too. Therefore, in this chapter I also introduce our ongoing investigation of the conductive response of the sample in broader frequency range using the multi-THz – mid-infrared pulsed spectroscopy method described in section 1.2.3. This technique provides us with a possibility to study the total contribution of the ensemble of nanocrystals with sizes down to $\sim 4-5$ nm to the measured photoconductivity.

Namely, it enables accessing the conductivity resonances of confined photoexcited electrons in such small NCs occurring in mid-infrared range whereas the conventional THz spectroscopy can detect only weak tails of these resonances.

The structure of this chapter is the following. Section 4.1 provides detailed description of the sample preparation procedure and of their structure and morphology provided by transmission electron microscopy. An investigation of the photoconductive response of the NCs in the THz spectral range measured via OPTP method (section 1.2.1) is described in section 4.2. Here we keep the analysis and interpretation of the results on the level as it has been published in [4]; the conclusions are also drawn here within this framework. However, after that publication a significant theoretical and experimental progress has been achieved in our group. The theoretical progress and its impact on the THz results in Si NCs is presented in section 4.3, and, finally, section 4.4 treats the results obtained in an ultrabroadband THz –multi-THz – mid-infrared spectral range.

4.1. Samples: preparation and preliminary characterization

In this work we study a set of superlattices composed of 100 bilayers consisting of a 4.5 nm thick layer, which contains Si NCs in SiO_2 environment, and of a 4 nm thick isolating layer of SiO_2 (figure 20). The samples were prepared via the superlattice approach [3] using nitrogen-free SiO_x plasma enhanced chemical vapor deposition (PECVD) [100,101]. In a nutshell, PECVD technique was employed for deposition of a periodic SiO_x/SiO_2 structure on a fused silica substrate (figure 21a) with SiH_4 and O_2 used as precursor gases. Subsequently, the structure underwent a thermal annealing at 1100°C for 1 hour in pure N_2 which induced phase separation between silicon and silicon dioxide in the silicon-rich layers and the crystallization of Si NCs (figure 21b). All samples were finally annealed at 500°C in a pure H_2 atmosphere to passivate the dangling bonds at the Si/SiO_2 interfaces.

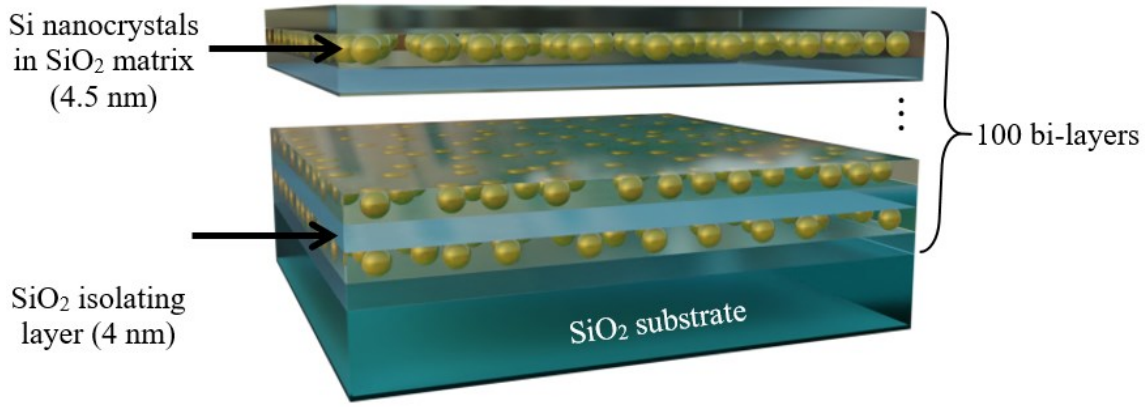

Figure 20. Principal scheme of the investigated samples.

Adjustment of the precursor gas flow ratio in the PECVD process allowed reaching a wide variety of the silicon oxide composition (we focused on samples with x = 0.7, 0.5, 0.3, and 0.0): the amount of Si excess in the initial SiO_x layers controls the size of Si NCs as well as their volumetric filling factor s within each layer. The sample with x = 0.0 corresponds to a polycrystalline silicon layer.

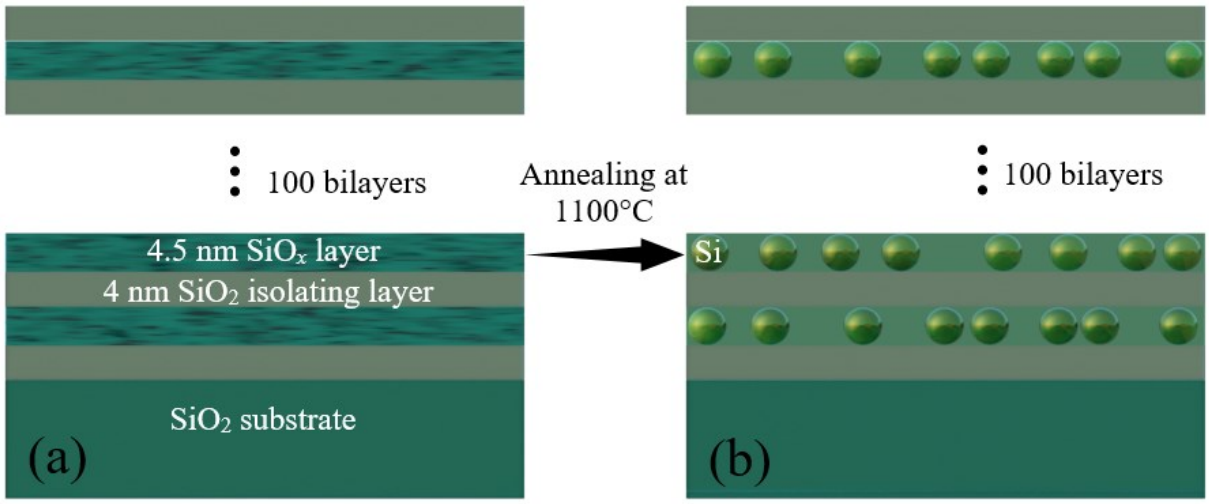

Figure 21. Scheme of the periodic structure: (a) SiO_x/SiO_2 superlattice prepared by PECVD; (b) silicon nanocrystals in SiO_2 matrix produced by thermal decomposition of silicon rich SiO_x layers.

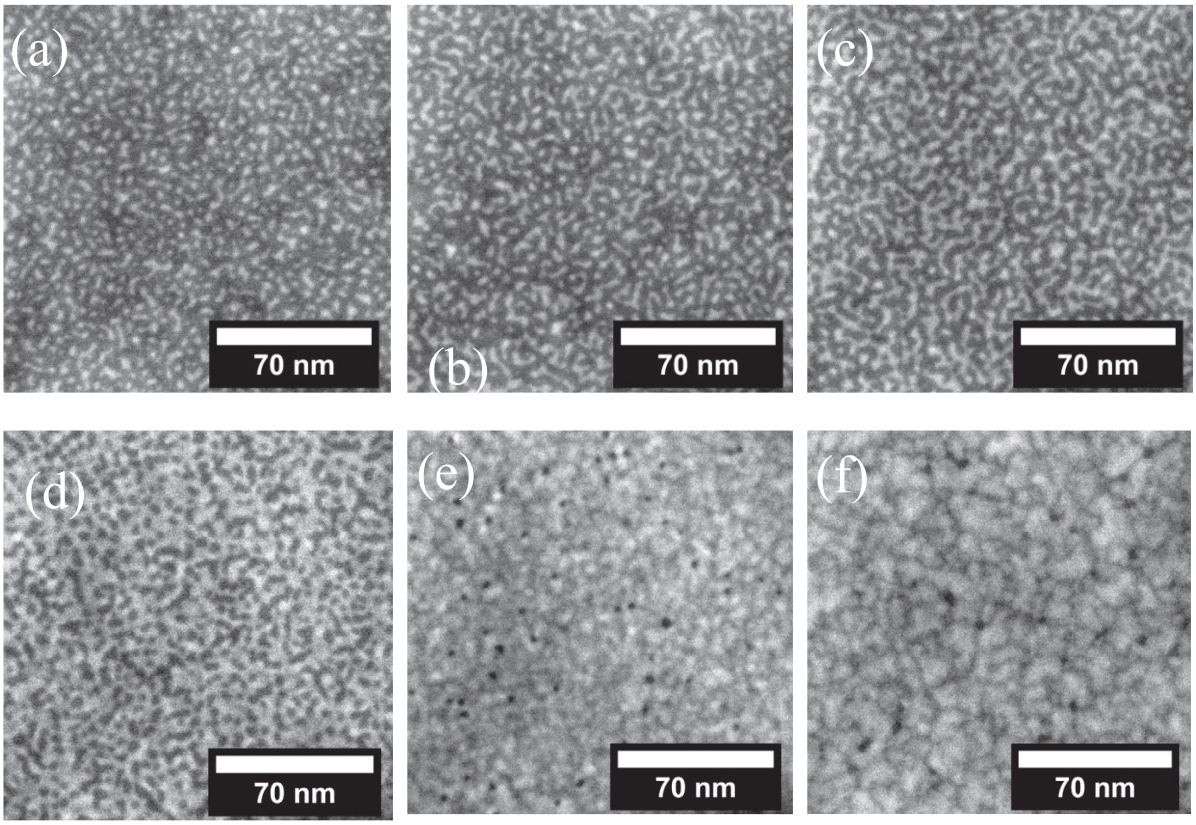

Figure 22. Plane-view EF-TEM images of samples with 6 different SiO_x stoichiometries: (a) $SiO_{1.0}$, (b) $SiO_{0.9}$, (c) $SiO_{0.7}$, (d) $SiO_{0.5}$, (e) $SiO_{0.3}$, (f) $SiO_{0.0}$. The images are energy-filtered at 17 eV (5 eV slit), with the white areas representing Si concentration (figure 1 from [101]).

Selected properties of the samples published previously or measured in this work are summarized in table 3. The size distribution of nanocrystals and the Si NCs filling factor in our samples were determined by plane-view energy-filtered transmission electron microscopy (EF-TEM) [101]. The average size of nanocrystals in sample $SiO_{0.7}$ as determined by EF-TEM is

5.0 ± 1.5 nm in relation with the nominal thickness of SiO_x layers. EF-TEM images indicate that silicon in the samples $SiO_{0.5}$, $SiO_{0.3}$ and $SiO_{0.0}$ is percolated and the average size of Si NCs is thus an undefined quantity from this point of view (figure 22).

Sample	$x = 0.0$	$x = 0.3$	$x = 0.5$	$x = 0.7$	Comment
Si areal fill fraction s_A (%)	~100	~100	63	38	from EF-TEM [101]
Si volumetric fill fraction s (%)	99 -	84 -	- 42	- 25	†from measured optical absorption $s = 2/3\ s_A$
n of NC layers at 400 nm	5.4	4.1	2.4	2.0	*from effective medium calculations
α at 400 nm (cm^{-1})	8.6×10^4	3.7×10^4	0.72×10^4	0.35×10^4	*from effective medium calculations
α at 400 nm (cm^{-1})	12×10^4	5.5×10^4	1.7×10^4	0.30×10^4	from optical absorbance measurements (Fig.23)
s_{coh} (%)	54	22	14	1.2	fit of THz data
s_{inc} (%)	44	29	3	< 0.1	
K_{inc}	≳ 20	2	2	-	
μ_{RT} ($cm^2V^{-1}s^{-1}$)	30	18	15	-	
μ_{LT} ($cm^2V^{-1}s^{-1}$)	10	10	6	-	
conductive NCs (%)	~100	60	40	< 5	$=(s_{coh}+s_{inc})/s$

Table 3. Summary of sample properties from the literature and from optical and THz measurements presented in this work. †The volumetric filling fraction s was calculated from the areal filling fraction ($s = 2/3\ s_A$) for samples with $x = 0.5, 0.7$. For sample $SiO_{0.3}$ the value was chosen in order to match the experimental and theoretical absorbance in figure 23. For $SiO_{0.0}$ the value should be close to 100%: for $s = 99\%$ we obtain again a good match between the experimental and theoretical absorbance. *The procedure of calculation of effective refractive index n and absorption coefficient α in the optical range was described in [24]; to this aim, the complex refractive index of pure Si at 400 nm was taken from [102]: α_{Si} = 9.5×10^4 cm^{-1}, $n_{Si} = 5.55$.

On the other hand, we show in section 4.4 that the THz photoconductivity spectra of all samples strikingly depend on the pump fluence (i.e., on the photocarrier concentration). It has been shown and extensively discussed that such a finding is a fundamental signature of a significant contribution to the conductivity of inclusions that are not electrically percolated [24, 2, 68, 103]. This apparent discrepancy between TEM and THz measurements will be thoroughly discussed in this study. At this point we just wish to stress the reason why we

systematically develop here a description in terms of the quantum confinement of photocarriers in isolated NCs.

Optical absorbance at the pump wavelength is an important parameter for the analysis of transient THz spectra. In figure 23 we show the absorbance of our samples at 400 nm and we compare it with effective absorbance of the Si/SiO_2 mixture calculated using Maxwell-Garnett effective medium approximation (equation 2.30) and the transfer-matrix formalism for layered structures [104]. To this aim we used the intrinsic optical properties of silicon (absorption coefficient $\alpha_{Si} = 9.5 \times 10^4$ cm^{-1}, refractive index $n_{Si} = 5.55$) [102] and of fused silica [105]; the following permittivity terms were substituted into 2.30:

$$\varepsilon_p = \varepsilon_{Si}(400\text{ nm}) = \left(n_{Si} + i\frac{\lambda}{2\pi}\alpha_{Si}\right),$$

$$\varepsilon_m = \varepsilon_{SiO2}(400\text{ nm}) = 2.15, \qquad (4.1)$$

$$\varepsilon = \varepsilon_{eff}(400\text{ nm}) = \left(n + i\frac{\lambda}{2\pi}\alpha_{eff}\right).$$

For the given sizes of NCs the effective medium approach can be safely applied in the optical range. There is a reasonable agreement between the experiment and the calculation, which corroborates the view that the samples are composed mainly of Si and SiO_2 and they are free of extrinsic absorption. From this analysis we also conclude that the quantum yield ξ of the photogeneration of mobile carriers is close to 1 in these samples.

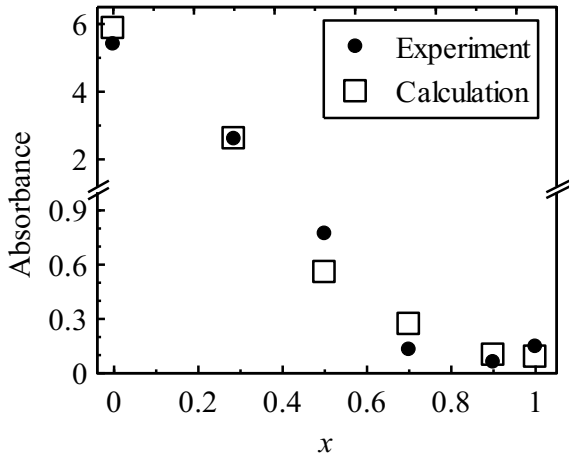

Figure 23: Calculated and measured optical absorbance of various Si NC samples at 400 nm defined as $-\ln(I_s/I_{sub})$ where I_s is the transmitted light intensity through the sample (including all internal reflections in the layered structure) and I_{sub} is the transmitted intensity through the bare substrate.

4.2. THz Photoconductivity

Measurements of the transient THz photoconductivity spectra (optical pump – THz probe experiments) were performed using the experimental setup for time-resolved THz spectroscopy described in section 3.1. A part of the output laser beam was frequency doubled to 400 nm (3.1 eV) and subsequently used for the sample photoexcitation. Considering the

energy gap of silicon ($E_g = 1.12\ eV$ [106]), we assume that photocarriers in the nanocrystals are generated via single-photon absorption mechanism. Homogeneous excitation across the sample was achieved by defocusing of the beam to an area significantly larger than the 3-millimeter diameter of the aperture of the metallic sample holder; the pump beam fluence was controlled over nearly three orders of magnitude using a combination of neutral density filters and a variable attenuator based on a thin film polarizer. The THz pulses impinged on the sample under normal incidence, thus probing the charge transport in the plane of the sample. The experiments were performed at 20 and 300 K.

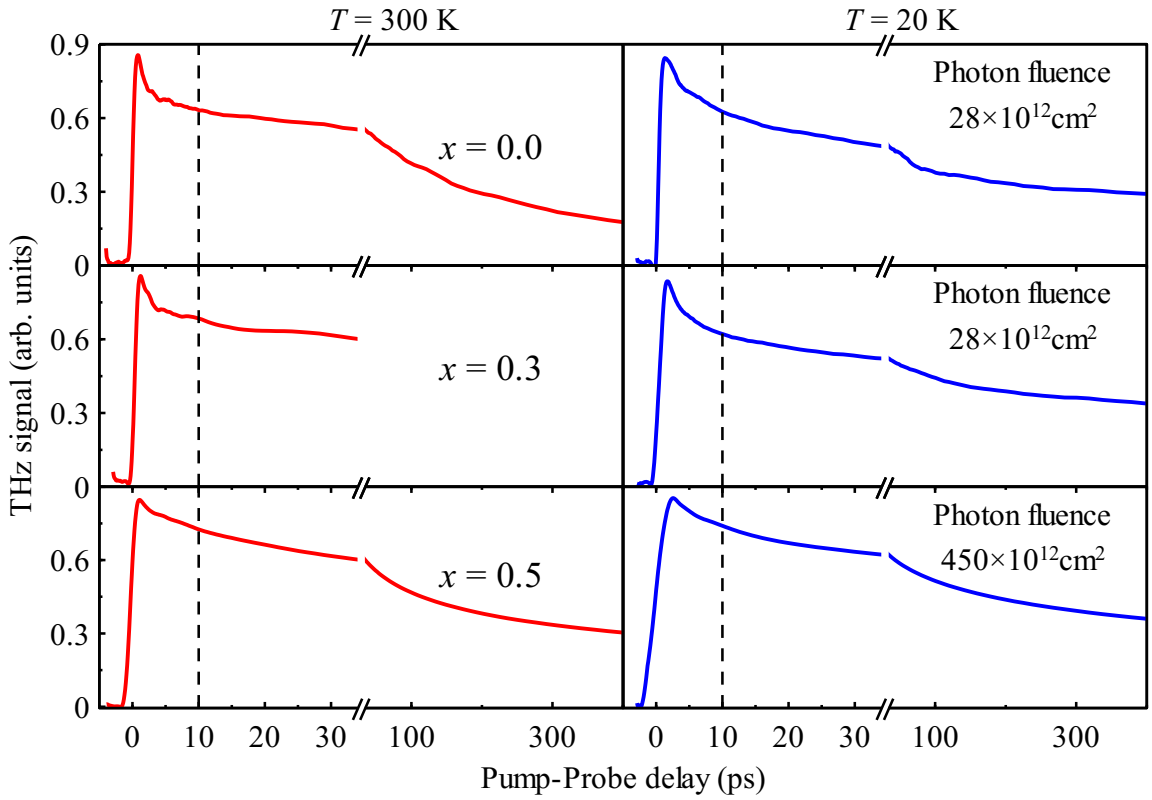

Figure 24. THz conductivity dynamics of photoexcited carriers in the samples $SiO_{0.0}$, $SiO_{0.3}$ and $SiO_{0.5}$. Dashed line at 10 ps shows the pump-probe delay at which THz photoconductivity spectra were measured.

Figure 24 shows the THz kinetics with the rise and decay of the transient THz signal after photoexcitation. After a small initial faster decrease of the signal, a slower decay on the timescale of ~150 ps at room temperature (RT) and of ~90 ps at LT is observed. We measured the photoconductivity spectra at a pump-probe delay of 10 ps (figure 24) where the signal decrease is already quite slow and the sample is in a quasi-steady state. This time delay is also significantly shorter than the excitation formation time [107]; for this reason, we do not consider the electron-hole interaction in our analysis, and we interpret the results in the frame of conduction band carrier motion.

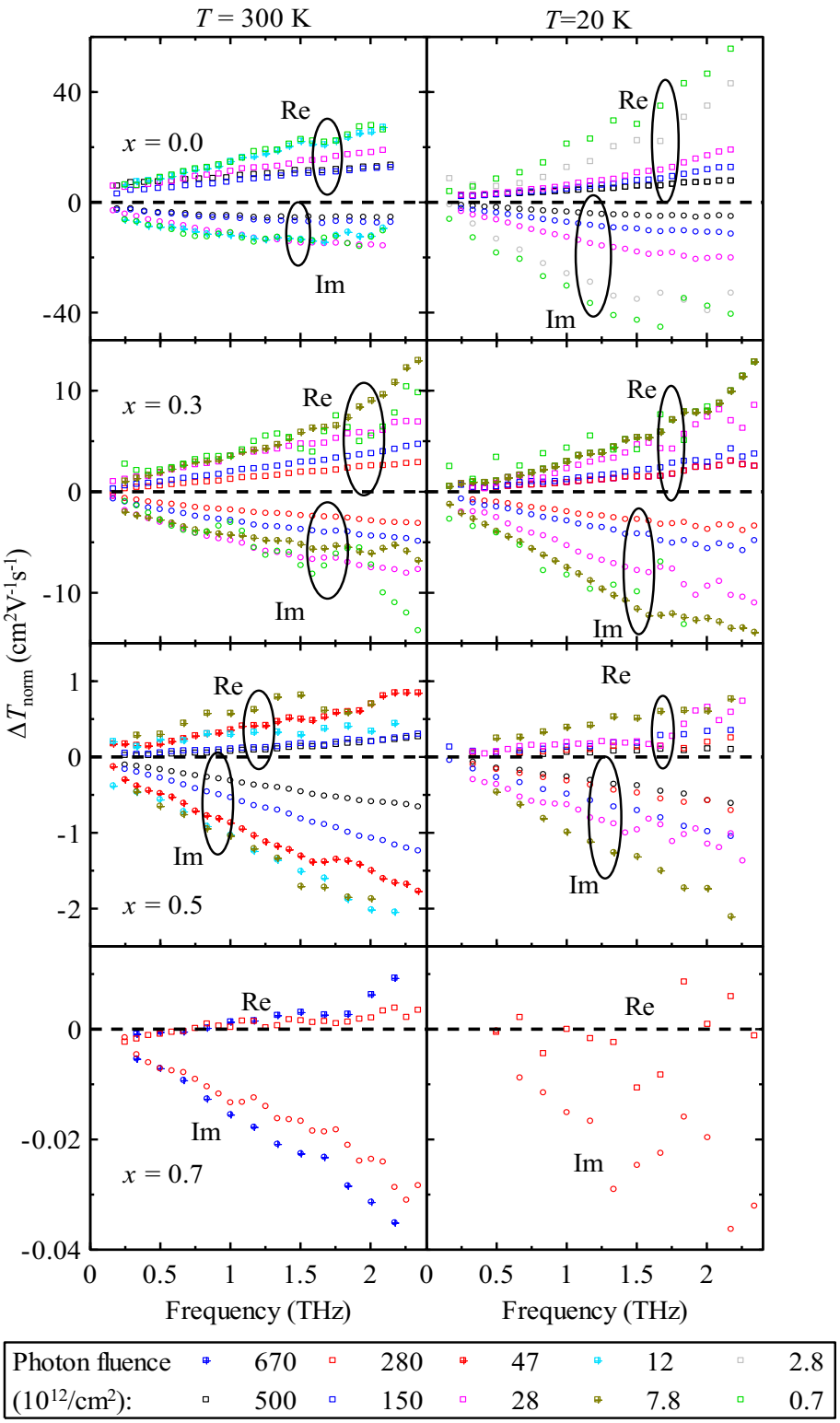

Figure 25. Measured normalized transient transmission spectra for samples 0.0, 0.3, 0.5 and 0.7 at room temperature and 20 K; pump–probe delay: 10 ps.

Our first attempt was to assess the confinement effect using semiclassical Monte-Carlo simulations (section 2.2.4) as it was done in the case of similar Si NC multilayers [24], where entirely non-percolated samples were studied, and the model provided very nice quantitative agreement with the experiment at RT by using nominal sample parameters (i.e., without

fitting.) However, this approach fails in a comparative analysis of the photoconductivity spectra of our Si NCs at room temperature and 20 K. On the one hand, the morphology of the sample does not change with temperature; therefore, the effective medium model, which is used to assess the depolarization fields effect, should be temperature independent. On the other hand, the semiclassical Monte-Carlo simulations predict quite dramatic changes in the microscopic conductivity and consequently in the THz transmission spectra: e.g., higher values of the microscopic mobility and a significant redshift of the conductivity peak of confined carriers have been previously predicted for band-like transport in microcrystalline silicon upon cooling [56]. However, such effects are not confirmed experimentally: in fact, the spectra measured at 20 and 300 K do not differ much.

For this reason, we employed quantum mechanical calculations of the THz conductivity (section 2.2.4). At room temperature, the quantum model provides the same spectra as the semiclassical approach but the results significantly differ at low temperatures. Namely, the quantum calculations are able to reproduce the experimental photoconductivity spectra.

4.2.1. Quantum Mobility Evaluation

Let me point out that the quantum mechanical model of THz mobility described in the section 2.2.4 was still under development during this study and that it was used for the first time for evaluation of the experimental results. In this first quantum mechanical model, an instantaneous charge carrier thermalization was implicitly considered after the first inelastic scattering event. In the language of section 2.2.4 this assumption corresponds to the limiting case of diffusion coefficient $D_{diff} \to \infty$ in the formula 2.26 and leads to overestimation of the thermalization current j_{th}.

In the calculations of quantum mechanical conductivity spectra we considered NCs in the form of rectangular boxes with dimensions $a_x \times a_y \times a_z$ and an infinite confining potential. Assumption of the infinite depth of the potential well is best justified by comparing the electron band offset between Si and SiO_2 (~3.1 eV) and the energy of electron states that contribute to the THz response (well below 0.5 eV). The choice of the particular shape of the confining potential allowed us to perform complex numerical calculations within a reasonable time: indeed, the shape of real NCs in the sample is irregular and we expect that the differences in the response of NCs of different shapes do not exceed the experimental error as long as their characteristic dimensions and symmetries are similar. We checked this assumption numerically by comparing the rectangular and spherical confining potentials. The dimension a_z is perpendicular to the layers and it is constrained by the sample geometry to values smaller than the nominal layer thickness of 4.5 nm. Consequently, to calculate spectra of NCs larger than 4 nm, we assume that a_x and a_y can take any required values, while a_z is fixed to 4 nm. The calculations of eigenstates of unperturbed Hamiltonian take into account the anisotropy of the conduction band minima in the *L*-valey of silicon (effective masses: $m_1 = m_2 = 0.19\ m_0, m_3 = 0.97\ m_0$; here m_0 denotes the free electron mass). The position of the strongest resonance in the microscopic mobility spectra depends on the temperature and electron density in the NC since they determine which dipole transition between the energy levels becomes the most pronounced. At low electron density (less than one electron per NC), the largest contribution comes from the transition from the ground to the first excited state, thus resulting

in a resonance at frequency $3\hbar^2\pi^2/2m_1a_x^2 \approx 240$ meV (57 THz) for NC size a_x = 5 nm and ≈59 meV (14 THz) for a_x = 10 nm. For a_x = 20 nm the above formula yields the transition between the lowest levels at ≈15 meV (3.6 THz); however, this value is smaller than the thermal energy k_BT at room temperature and thus the mobility spectrum for such large NCs cannot be determined merely by the lowest resonance frequency value.

The mean carrier concentration (10^8 cm^{-3}) used in the calculations corresponds to less than one photoelectron per NC. In this case, the vast majority of NCs is either unexcited or occupied by a single electron, therefore the Pauli exclusion principle has a negligible influence and the thermal Fermi-Dirac distribution of electrons can be approximated by the Maxwell-Boltzmann distribution function, as we verified for our particular system. In this regime, the mobility is independent of the carrier concentration.

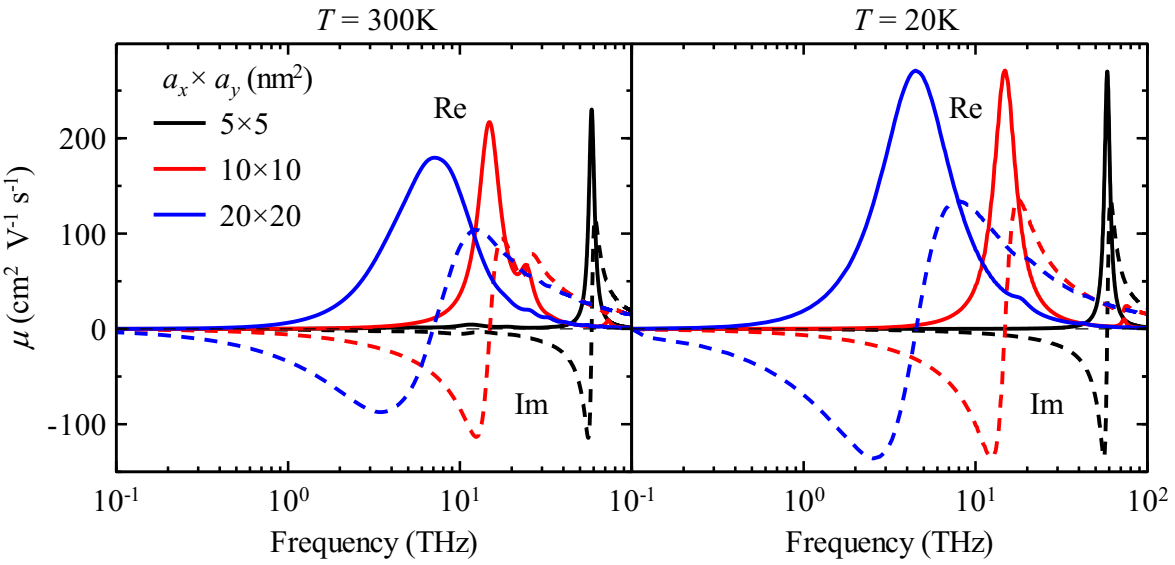

Figure 26. Examples of THz – mid-infrared mobility spectra calculated by the quantum mechanical approach for Si NC sizes $a_x \times a_y$ of 5 × 5, 10 × 10, and 20 × 20 nm^2 (a_z = 4 nm); dephasing time $1/\gamma$ = 60 fs. Full lines: real part, dashed lines: Imaginary part.

In figure 26 we present examples of calculated microscopic mobility spectra in the THz – mid-infrared range. Clearly, we observe a dependence of the spectrum on the NC size. The main part of the signal (peaks corresponding to transitions between quantum energy levels) occurs in the mid-infrared frequency range for the NC sizes considered; the THz range contains essentially tails of these signals. Figure 27a shows the dependence of the real part of the calculated mobility on the NC size for three particular frequencies in the THz range, which is accessible by our experiment. From these plots we can conclude that the mobility values start to decrease significantly for NC sizes below 20 nm.

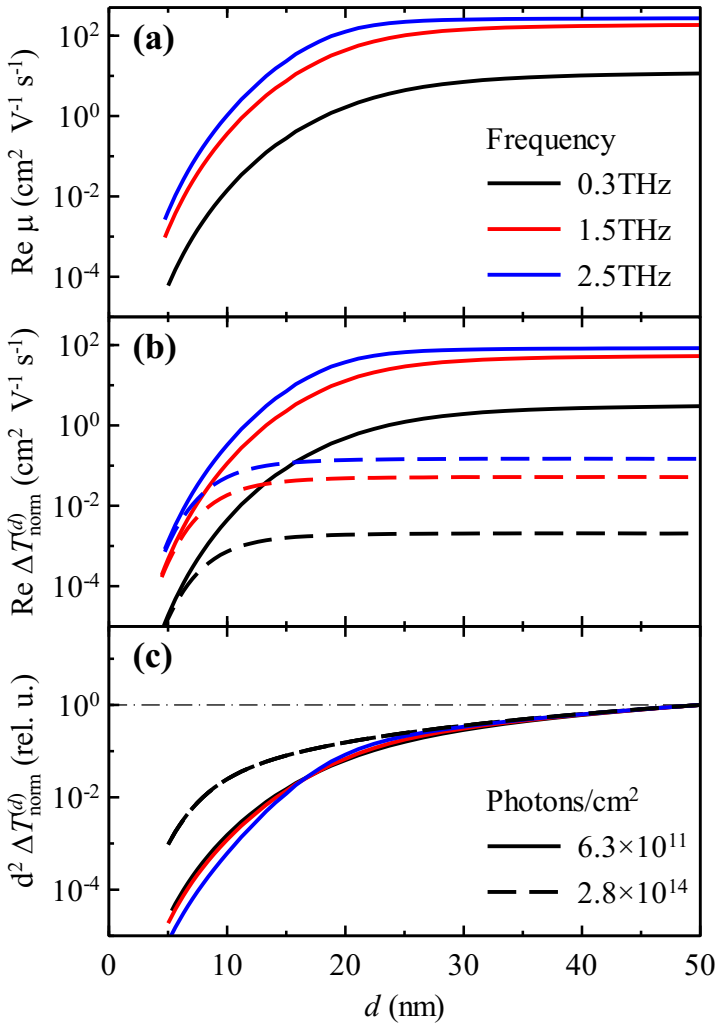

Figure 27. (a) Real part of quantum mechanical mobility in Si NCs as a function of the NC in-plane size d ($a_x = a_y = d$, $a_z = 4$ nm) at 3 different frequencies at 20 K. (b) Real part of normalized transient transmission ΔT_{norm} calculated from the data of the plot (a) with the help of equation (4.2) using typical parameters of our samples at two excitation fluences. (c) Weighted transient transmission $d^2 \times \Delta T_{norm}$ in relative units (with respect to this quantity calculated for NCs with $d = 50$ nm); it represents the real part of the THz signal per single NC with the given size.

4.2.2. Transient THz transmittance

Here we take into account the contribution of depolarization fields to the measured (effective) photoconductive sample response by using VBD EMT model (section 2.2.6). For a thin film sample containing both percolated and non-percolated photoconducting parts the expressions 2.44 and 2.45 for the transient transmitted function can be simplified, and ΔT_{norm} is related to the photoconductivity as follows [68]:

$$\Delta T_{\text{norm}}(d) = \left[V(1 - e^{-\alpha L}) + B\frac{\ln(1 + Y_0(d)) - \ln(1 + Y_0(d)e^{-\alpha L})}{Y_0(d)}\right]\frac{\alpha_{loc}\xi\mu(d)}{\alpha}. \quad (4.2)$$

The first term at the right-hand-side describes the percolated part (from equation 2.44) and the second term describes the non-percolated part (form equation 2.45). The variable d in equation 4.2 denotes the dependence of this theoretical quantity on the dominant size of NCs through the confinement effects encoded into the microscopic mobility μ. The meaning of all other symbols and quantities is explained in equations (2.43) and (2.46). Finally, in order to take into account the distribution of NC sizes in the sample, we define the weighting of the signals coming from various NCs by their volume [24, 103]:

$$\Delta T_{\mathrm{norm}} = \frac{\int_{d1}^{d2} \Delta T_{norm}(d)\, w(d)\, \mathrm{d}d}{\int_{d1}^{d2} w(d)\, \mathrm{d}d}, \tag{4.3}$$

where $w(d)$ is the volumic density of NCs with the size d. Equations 2.48 and 4.3 constitute the link between the measured and calculated quantities.

Equation 4.3 is quite complex and it is expected that the distribution of NC sizes may influence significantly the shape of the measured THz spectra. In the following discussion we attempt to clarify the main trends in the variation of several important quantities with the NC size. In figures 27b and 27c, we demonstrate the sensitivity of the standard THz spectroscopy to the conductivity processes in variously sized Si NCs. Figure 27b shows the normalized transmission $Re(\Delta T_{\mathrm{norm}}(d))$ calculated for the case when NCs with the given dimensions ($a_x = a_y = d$, $a_z = 4$ nm) have the same total volume in the sample independently of their size d. At low pump fluences (i.e., under conditions for which the depolarization fields are negligible) this quantity follows the behavior of the microscopic mobility μ plotted in figure 27a. At high pump fluences (dashed lines in figure 27b), owing to the depolarization field effects, the drop in the normalized transmission observed for small NC dimensions ($d < 20$ nm) is less pronounced. It means that the range of a good experimental sensitivity is broadened and its lower end is shifted down to about 10 nm size (note that ΔT_{norm} is a quantity normalized by the pump fluence; the raw measured signal $\Delta E_t/E_t$ will be appropriately up-scaled by the value of ϕ for high fluences). The imaginary parts (not shown in the figures) are negative but exhibit analogous decrease of the absolute value for decreasing nanoparticle size. In figure 27c, we plot the calculated product $d^2 \times \Delta T_{\mathrm{norm}}(d)$ as a function of NC size d normalized with respect to 50-nm-sized NCs. This weighted transient transmission function compares the signal from samples with the same number of NCs with the given size. In other words, the plot represents (in relative units) the THz photoconductivity signal per single NC. A dramatic decrease of the signal with the NC size in our quasi-two-dimensional (2D) system (which is enhanced due to the proportionality to d^2) is clearly observed. In standard disordered 3D nanostructures, the signal of individual NCs is proportional to $d^3 \times \Delta T_{\mathrm{norm}}(d)$, i.e., its decrease towards small NCs will be even faster.

4.2.3. Fitting model

The multilayer samples, where the NC size is imposed by the layer thickness to some extent, offer a priori a better control over the NC size than other 3D samples. However, it has been shown previously that the photoconductivity experiments detect also larger Si clusters in

these samples and, consequently, that a significant distribution of sizes does exist [24]. In this work we assume a continuous distribution of NC sizes following the log-normal law:

$$f_{LN} = \frac{1}{d\delta\sqrt{2\pi}} e^{-\frac{(\ln d/d_0)^2}{2\delta^2}}, \quad w(d) = d^2 f_{LN}(d), \tag{4.4}$$

where d is the in-plane diameter of the NCs, δ and d_0 define the width and the peak position of the distribution, respectively, and w is the volumic density of NCs entering equation 4.3.

In practice, mobility spectra of electrons for NC sizes between $d_1 = 4$ nm and $d_2 = 100$ nm were calculated using quantum mechanical approach with a 1 nm step in order to create a database of spectra densely covering the investigated range; subsequently, the mobility data were interpolated to obtain quasi-continues series of data as required for the fitting with integral equation 4.3. The quasi-continuous database of $\mu(\omega)$, was prepared for 300 K and 20 K and for several dephasing times $1/\gamma$ in the range 30–120 fs. $\Delta T_{\mathrm{norm}}(d)$ was evaluated using equation 4.2 with the values of absorption coefficient α obtained from absorbance measurements (table 3) and assuming no percolation, $V = 0$. The parameters B and D of the effective medium model are related to the sample morphology and they are defined by formulas 2.42 with the shape factor $K_{\mathrm{coh}} = 2$ and a filling fraction denoted s_{coh}. This term describes mostly coherent motion of electrons in NCs that dominantly contribute to the conductivity.

In addition to the coherent term, we consider that an additive incoherent contribution might exist. This contribution would take into account the conductivity of possibly existing very large Si NCs and/or some percolation paths, which are predicted by TEM measurement in samples with $x \leq 0.5$. The incoherent character of this term (dominated by the scattering or other mechanism hindering coherent long-range transport) is inferred from the shape of experimental spectra (see figure 28): (*i*) the real part of the conductivity in Si rich samples does not vanish at low frequencies, which implies the existence of a long-range conduction; (*ii*) for example, in polycrystalline Si layers with nearly micrometer-sized grains, the character of the coherent response would be Drude-like with a higher magnitude and a significantly decreasing real part with frequency [108], which is clearly not the case here. As the character of the motion of these charge carriers is unknown, we assume here the simplest case of constant value of the real part of the mobility μ_{RT} for the room temperature and μ_{LT} for the low temperature. These inclusions are characterized by a filling fraction s_{inc}.

It has been shown that NCs with diameter $d \approx 4$ nm and smaller do not contribute to the response in the THz range. Hence the filling factor $s_{\mathrm{coh}} + s_{\mathrm{inc}}$ represents the part of Si NCs that can be detected by THz conductivity measurements. This sum can be smaller than the nominal value s presented in table 3; consequently, s_{coh} and s_{inc} are used as fitting parameters.

In total we have 6 fitting parameters for each sample: s_{coh}, s_{inc}, μ_{RT}, μ_{LT}, δ and d_0, which should describe the complex spectra at both 300 K and 20 K and for a set of pump fluences spanning over nearly three orders of magnitude. We also tried to free the shape factor of inclusions participating to the incoherent contribution K_{inc}, which, in the case of sample $SiO_{0.0}$, significantly improves the fit when its value differs from 2. Consequently, we include also this possibility in our discussion.

4.2.4. Results and Discussion

The comparison between the experimental spectra and their global fits using the model described above (equation 4.3) can be seen in figure 28 for four samples ($SiO_{0.0}$, $SiO_{0.3}$, $SiO_{0.5}$, and $SiO_{0.7}$); the measured signal for sample $SiO_{0.7}$ was very weak; therefore we were able to carry out experiments with the highest excitation fluence only.

An increase of the signal amplitude with an increase of Si content (decrease of values x) is due to a better connectivity of NCs leading to a larger average size (clustering) of NCs. The larger size has a consequence in larger values of the quantum mobility in the THz range. Indeed, figure 28b shows the NC size distribution defined by equation 4.4, which follows from the fits. Clearly the distribution of conductive NCs shows a significant shift of its maximum towards smaller sizes when the Si content in the layers is decreased (from top to bottom of figure 28b). The other parameters provided by the fitting procedure are summarized in table 3.

The THz spectra below 3 THz do not depend much on the dephasing factor γ. Note that the dephasing time $1/\gamma$ at room temperature in high quality Si single crystals reaches about 200 fs [109], while in polycrystalline Si films it may decrease typically down to about 60 fs [108], or to ~35 fs in the case of silicon-on-sapphire [80]. We verified that the spectra can be fitted with quite similar sets of parameters for the scattering times $1/\gamma$ ranging between 50 and 120 fs; however, for the scattering times of 30 fs or shorter the quality of the fit becomes significantly worse. This is in agreement with our hypothesis of essentially coherent contribution of confined charge carriers in Si clusters described by the quantum model of the mobility.

At first glance the comparison of EF-TEM images and size distributions (see [101]) with the size distributions inferred from THz spectra may seem problematic. However, we think that they both present valuable and complementary tools of analysis of the behavior of the nanostructures. The TEM images provide information regarding the shape and size of inclusions, which are statistically most frequently encountered in the sample. However, their electrical connectivity cannot be determined from TEM images, and the percolation or non-percolation of the system is only inferred from a geometrical proximity of several inclusions. In contrast, the THz spectroscopy provides a statistical image of inclusions that carry the conductivity of the sample. On the one hand, very small inclusions feature a stronger confinement and a small volume per inclusion, which may both lead to a very low contribution to the conductivity of such NCs; on the other hand, the carrier transport in the parts, which are considered to be percolated in TEM images, may be hindered by defects or internal structure of these parts.

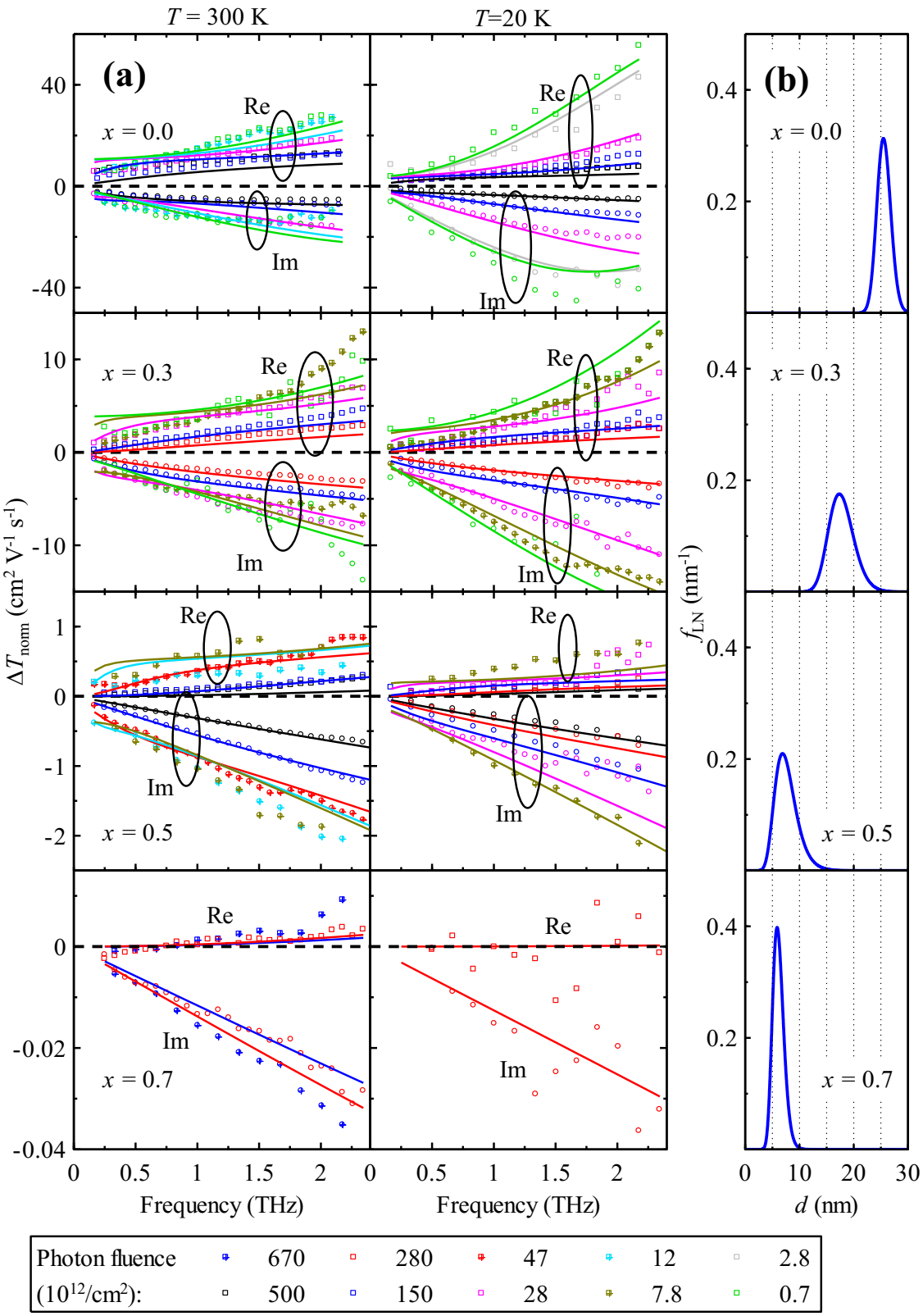

Figure 28. (a) Normalized transient transmission spectra for samples 0.0, 0.3, 0.5 and 0.7 at room temperature and 20 K; pump–probe delay: 10 ps. Symbols: experimental data, lines: global fits of the data by equation 4.3; pump fluences are indicated in the legend. (b) Size distributions of NCs participating to the conductivity as obtained from the fits of experimental spectra.

The sample with $x = 0.0$ was reported to be percolated from the point of view of TEM [101]. However, at THz frequencies it behaves like a polycrystalline Si such that the electrons feel an average confinement on the order of 25 nm. This can be put into contrast with recent measurements of polycrystalline Si samples with the grain size of about micrometer, where the Drude-type response is clearly observed without any significant pump fluence dependence of the carrier mobility [108]. This means that in our current NC sample quite large energy barriers separate the crystal grains on 25 nm spatial scale and that the electrons cannot move freely among them. Note that in the related TEM image shown in figure 22f many contrasted objects with a typical size of the order of 25 nm can be really identified. The inclusion of the incoherent conductivity term in this sample systematically leads to large values of the shape factor (K_{inc}> 20), which represent a percolation of the system or a sample morphology close to the percolation. This behavior could have been equivalently accounted for by a non-zero percolation strength term V.

In samples with $x = 0.3$ and 0.5 the distribution of conductive NCs progressively shifts to lower values and also the volumetric filling fraction of the NCs participating to the THz conductivity drops to about 60–40%. The conductivity is essentially carried by NCs with the size distribution around 17 nm for $x = 0.3$ and around 7 nm for $x = 0.5$. There is still some non-negligible proportion of large NCs, which may be close to conductive percolation. Note that the width of the size distribution of sample $SiO_{0.3}$ is the largest, which means that in such a sample (nearly completely percolated from the point of view of TEM measurements) a rich variety of inclusion sizes and shapes can really develop. The size distribution becomes narrower again for $x = 0.7$, where the THz signal becomes quite weak as we approach the nominal size of NCs of 4.5 nm and crystals larger than 10 nm practically do not exist within the whole volume of the sample.

As to the incoherent contribution to the conduction, which has been tentatively included in the fitting procedure to take into account better the experimental data in the lowest-frequency region; indeed, the fits without this additional contribution would overestimate the real part of the measured mobility. However, adding further parameters or particular models, able to describe the mentioned mobility decrease, would not lead to better understanding of underlying processes and, therefore, we did not attempt this procedure.

4.2.5. Conclusion

Our analysis was focused on samples with variable and technologically controlled content of silicon in quasi-two-dimensional layers.

We show that a careful analysis, based on formulas rigorously derived from the wave equation for THz waves in inhomogeneous photoexcited media, can provide a detailed picture of the NC conductivity, which is complementary to a large extent to images obtained by TEM. In particular, we were able to show that a broad distribution of nanocrystal sizes exists in the sample and that the average size in this distribution varies with the Si content in the layers. Clustering of small NCs occurs in samples with higher Si content and such clusters contribute the most to the THz conductivity.

Sample $SiO_{0.0}$ with the largest Si content is close to the percolation and the conductivity signal is driven by electrons in grains with a typical dimension of 25 nm; such objects are observed in TEM images. With decreasing content of Si, the size of NCs with the dominant contribution to the conductivity progressively decreases, and for a clearly non-percolated sample $SiO_{0.7}$ the size of conducting NCs measured by THz spectroscopy becomes comparable to the thickness of SiO_x layers. This also proves the good control of the nanocrystalline size for oxygen rich samples.

4.3. Improvement of the quantum mobility data

In this section we improve and sharpen the fitting results presented above; this was enabled by the development of a consistent quantum mechanical theory of the THz conductivity as it has been described in section 2.2.4. In contrast to the calculations presented in the previous section and in [4] the thermalization current j_{th} introduced in equation 2.27 is properly taken into account in the mobility spectra presented in this section. In addition, the density of carriers n_e used for these calculations (10^{16} cm^{-3}) was chosen much closer to our experimental values compared to the previously used value (10^{8} cm^{-3}). Figure 29 depicts the mobility function calculated for the different NC sizes using the proper quantum model of the mobility in comparison with our former calculations shown in section 4.2 and in figure 26.

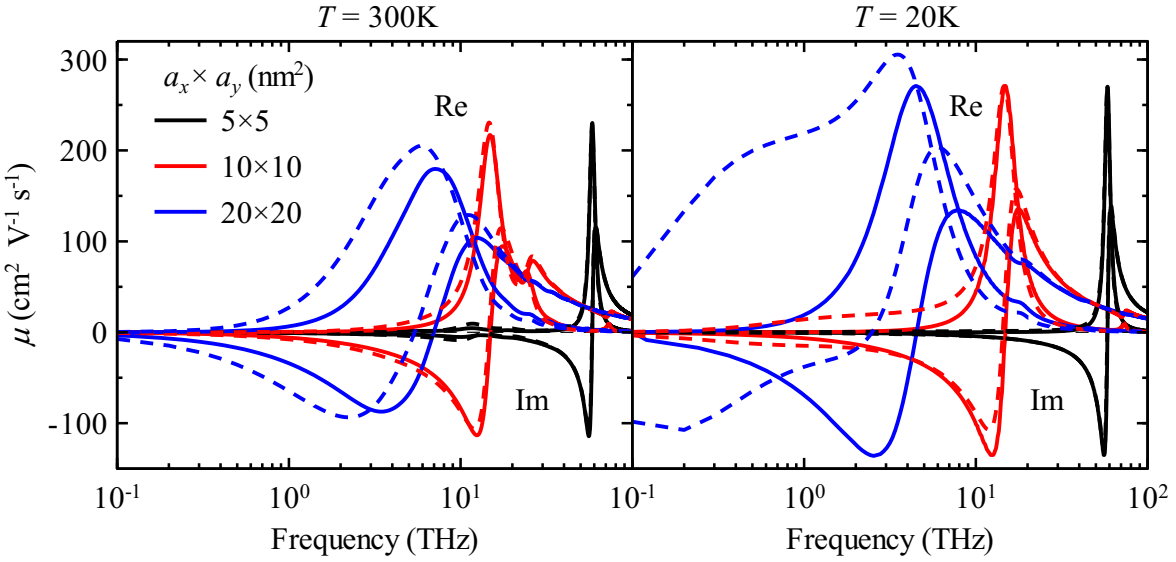

Figure 29. Examples of THz – mid-infrared mobility spectra calculated by the full quantum mechanical approach for Si NC sizes $a_x \times a_y$ of 5 × 5, 10 × 10, and 20 × 20 nm^2 (a_z = 4 nm); dephasing time 1/γ = 60 fs. Full lines: our first model used in Sec. 4.2, with $D_{diff} \to \infty$ (equation 2.26) and $n_e = 10^8\ cm^{-3}$; dashed lines: calculations with the properly introduced j_{th} (equation 2.26) and $n_e = 10^{16}\ cm^{-3}$. The thermalization current j_{th} predominantly contributes in the classical THz spectral range.

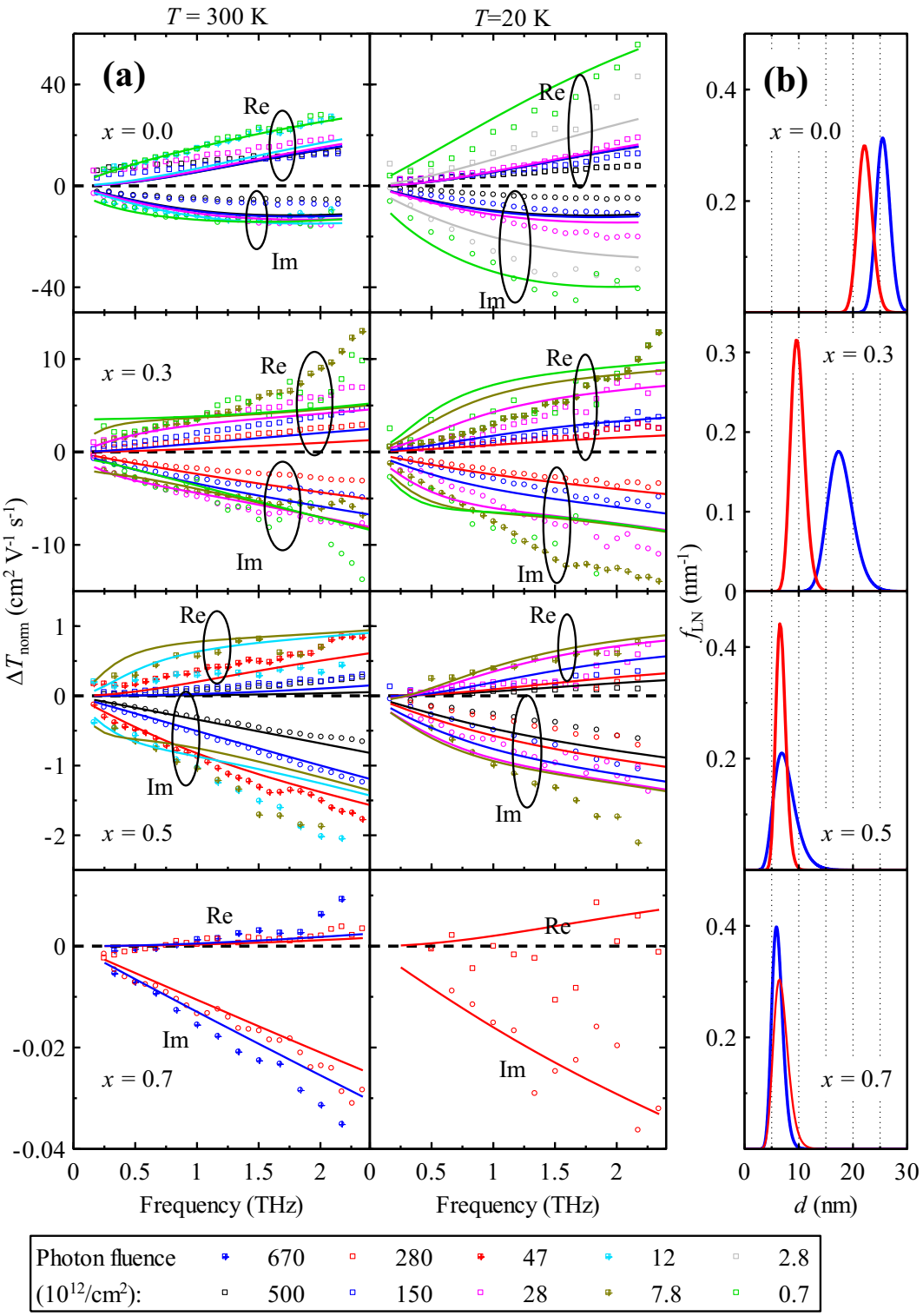

Figure 30. (a) Normalized transient transmission spectra for samples 0.0, 0.3, 0.5 and 0.7 at room temperature and 20 K; pump–probe delay: 10 ps. Symbols: experimental data in the THz range (same data as in figure 28), lines: global fits of the data by equation 4.3 using full quantum calculations of the mobility with the properly introduced j_{th} (equation 2.26) and $n_e = 10^{16}\ cm^{-3}$. (b) Red lines: Size distributions of NCs participating to the conductivity as obtained from the fits of experimental spectra; blue lines: show the results of modeling with our first quantum-mechanical model presented in Sec. 4.2; these distributions are also shown in figure 28.

Interpretation of the THz response of the sample x = 0.0 is now reconsidered to some extent due to the contribution of the thermalization current j_{th} to the quantum mobility spectra. Namely, percolation of the NCs exhibiting the coherent character of conductivity (described by s_{coh}) is being considered, i.e. normalized transmission function ΔT_{norm} is defined using essentially the first term in equation 4.2 based on the expression 2.44, while previously merely non-percolated contribution was assumed. Such consideration may seem controversial at first glance: on the one hand, percolation implies that conduction band electron can move freely among the structures without feeling any confinement. On the other hand, the quantum model yields the localized response of the carriers in NCs of given sizes (figure 30b). However, the polycrystalline nature of the Si NC layer in this sample (s_{total} = 99 %) suggests low energy barriers between the individual NCs and, plausibly, presence of dead layers of NCs. Thus, proposed interpretation in terms of the percolated layer using EMT can be justified. This interpretation is also used and justified in the following chapter. In addition, this assumption is in agreement with the simplified model of the incoherent mobility contribution where low energy barriers hinder coherent long-range transport.

The difference in the mobility spectra results in changes of the distribution function gained from the fitting of the THz photoconductivity spectra (figure 30). The final (corrected) values of the fitting parameters are summarized in table 4.

Sample	x = 0.0	x = 0.3	x = 0.5	x = 0.7
s_{coh} (%)	36	50	13	1.0
s_{inc} (%)	17	18	2	< 0.1
K_{coh}	-	1.4	2	1.9
K_{inc}	<0.1	2	2	1.9
μ_{RT} ($cm^2V^{-1}s^{-1}$)	570	30	38	-
μ_{LT} ($cm^2V^{-1}s^{-1}$)	3500	-	-	-

Table 4. Summary of sample properties from the fit of the THz spectra.

4.4. Multi-THz – mid-Infrared Photoconductivity

Comparative studies of charge carrier transport involving both the THz and multi-THz – mid-infrared frequencies have been only rarely carried out [110]. The complex properties of our samples (including substrates) in this spectral range imply an overlap of several phenomena inevitably occurring at these probing frequencies: (1) phonons in the fused silica substrate, in interlayers and in the matrix separating Si NCs in Si-rich layers, (2) optical interference of the mid-infrared waves within the multilayer, (3) quantum confinement of the photo-carriers within NCs and (4) the effective medium properties of photoexcited nanostructured layers (manifesting themselves through the plasmon resonance). The issues (1) and (2) do not need to be considered at all in the standard THz range since they are negligible below ~ 3 THz. Mapping and analyzing the interplay of all the above-mentioned phenomena has not been systematically performed so far in the literature and, in this sense, we present here a pioneering work in the field of the ultra-broadband THz – mid-infrared spectroscopy.

4.4.1. Steady-state measurements

Some of the sample properties contributing to the above-described phenomena can be determined independently in the ground state of the samples; this significantly reduces the number of free parameters for the final fitting of the pump-probe spectra. The aim of the following steady-state results discussed in this paragraph is thus to determine the microscopic and effective properties of the samples as much as possible prior to the interpretation of the pump-probe measurements. We start with an analysis of the ground state reflectivity spectra of the samples and of the bare substrate. These data yield parameters of phonons in SiO_2 and also some essential parameters for the employed EMT calculations.

The FTIR spectra of the bare substrate and of the samples measured using a standard FTIR spectrometer Bruker are shown in figure 31a and b, respectively. The bare substrate spectra in figure 31a are fit with a sum of 4 damped harmonic oscillators representing vibrational modes. These fits provide spectra of the complex refractive index n_{SiO2} of the substrate, figure 32a.

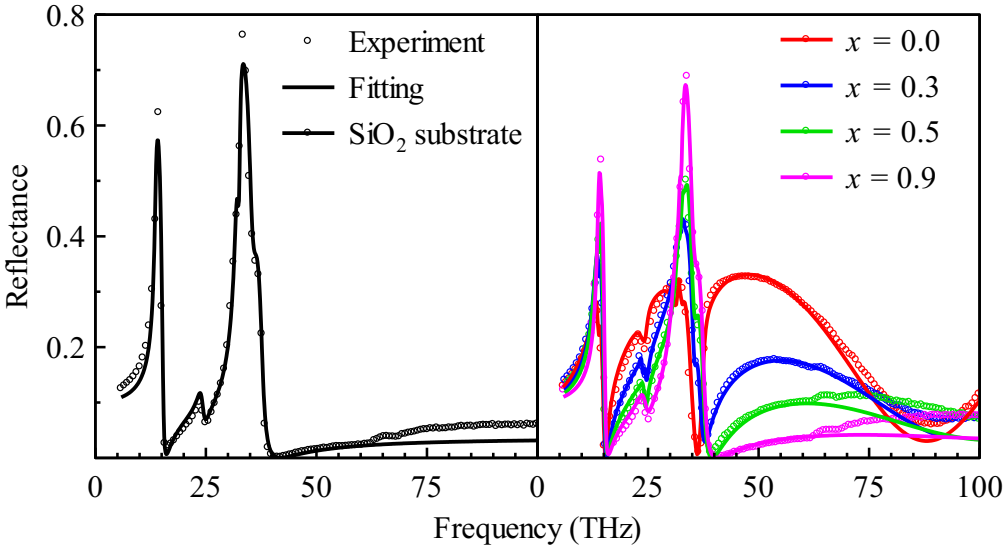

Figure 31. The ground-state power reflectance spectra and their fits for the substrate (a) and samples (b). Note that with decreasing content of Si the sample spectra approach those of the bare substrate (this is apparent namely for the sample with $x = 0.9$).

An appropriate carefully conceived model should be considered for the interpretation of the FTIR spectra of unexcited samples shown in figure. 31b. The samples consist of SiO_2 substrate, SiO_2 isolating layers and layers with Si NCs in SiO_2 environment (figure 20). The following items are considered:

- *Multilayer thickness.* The optical thickness of individual layers is much smaller than the multi-THz wavelength, therefore the whole multilayer structure can be described as an effective homogeneous medium. On the other hand, the total optical thickness of the multilayer (~ units of micrometers) is not significantly smaller than the probing wavelength (3.5–30 μm); therefore, the Fabry-Pérot interferences within the multilayer should be carefully taken into account. In other words, while previously (in section 4.2) we used the nominal multilayer thickness of $L = 850$ nm for the analysis of THz data, here, at shorter

wavelengths, the interference effects clearly appear in the spectra and the thickness mismatch would lead to a wrong or unsuccessful fit. For this reason, in the fits of the steady-state spectra, we finely tuned the total thickness L via adjustments of the bilayer thickness (increasing/decreasing of the thickness of isolating SiO_2 interlayer and Si NC layer by a tiny amount).

- *SiO_2 in interlayers.* Due to the fabrication method and thin film character of the interlayers, various strains and structural and compositional variations may develop during the deposition process and high-temperature annealing. The phonon spectrum of fused silica interlayers thus can slightly differ from the spectrum of the substrate; we thus allowed to vary the parameters of the vibrational modes in the interlayers to some extent with respect to the substrate values (namely the damping of the modes by < 10 %, and the frequency of the modes by < 1%). The resulting refractive index of SiO_2 in interlayers is denoted as n'_{SiO2}.
- *Layers with Si NCs and SiO_2 matrix.* The complex refractive index $n_{\mathrm{Si\text{-}eff}}$ of individual Si-rich layers in the ground state (which contain Si NCs and SiO_2 matrix) is modeled by the MG EMT model (section 2.2.5.3). Here, we consider the refractive index of the NCs: n_{Si} = 3.41 (note that the spectrum of n_{Si} near 18 THz can be slightly influenced by two-phonon processes [111,112] but we neglected this phenomenon in the current model). The FIR spectrum of the oxide, n''_{SiO2}, can be again modified compared to the one of the substrate due to the strains in thin films and due to structural and stoichiometric defects formed during the thermal decomposition. For the sample x = 0.0, $n_{\mathrm{Si\_eff}}$ is simply equal to n_{Si}. For oxygen richer samples we used the MG formula with the filling fraction value s as previously determined from the THz data and with the shape factor K_{MG} as a fitting parameter (indeed, the high-frequency FIR response depends quite significantly on K_{MG}, compared to the one in the standard THz range).
- *Effective refractive index of the multilayer.* The multilayer structure is formed by plane parallel bilayers with refractive indices n'_{SiO2} (for SiO_2 interlayers) and $n_{\mathrm{Si\text{-}eff}}$ (for layers containing Si NCs and SiO_2 matrix). An effective medium plane parallel capacitor model is then appropriate for the evaluation of the effective refractive index of each bilayer, hence of the whole multilayer.

The fitting model of the steady state spectra features a large number of parameters, however, most of them is related to the SiO_2 compound and they are determined by the peculiar features close to the vibration resonances. Note that it is not possible to carry out a successful fitting model without considering differences in the vibration spectra of various SiO_2 components. Besides these material constants, we use only L (multilayer thickness) and K_{MG} (shape factor in MG model of the Si NC layer) as free and independent parameters for each sample. The values of all these parameters were then kept unmodified for the fitting of the pump-probe spectra.

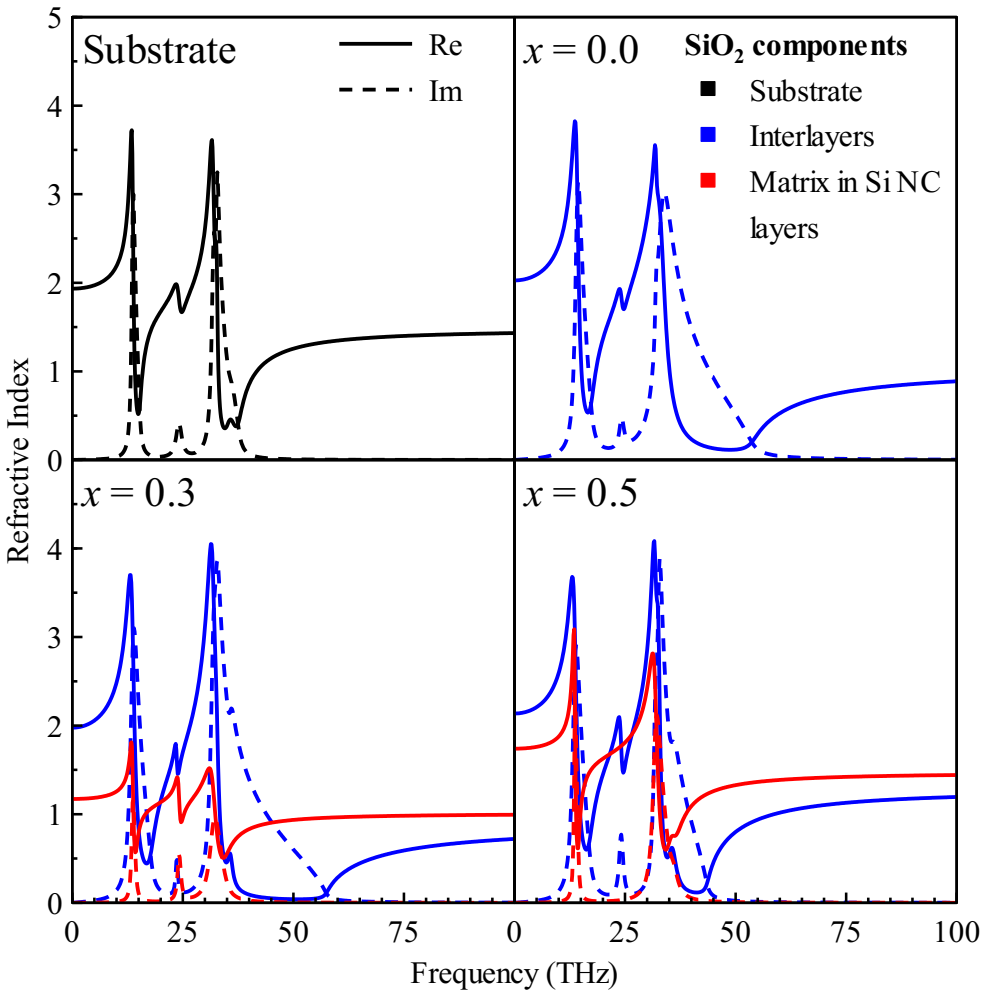

Figure 32. Dispersion of n_{SiO2} of the substrate and its change in the fused silica components of the samples. Note that SiO_2 matrix surrounding Si NCs features essentially an additional broadening of the vibration modes.

We measured also steady-state spectra of the samples by means of the multi-THz – mid-infrared pulsed spectroscopy technique using experimental setup described in section 3.3 (without introducing the pump beam for the sample photoexcitation). We compared these results to the spectra measured with the FTIR spectrometer in order to check the performance and spectral resolution of the multi-THz – mid-infrared technique. A significant difference between the corresponding curves can be clearly observed in figure 33(a,b). This brought us to a conclusion that the spectrogram measured by the multi-THz – mid-infrared method has a worse spectral resolution, i.e., it is broadened by an instrumental function. Such a broadening needs to be considered for the analysis and fitting of the pump-probe spectra.

By comparing both sets of the data we found that a Gaussian is a suitable instrumental spectral convolution function; its time-domain counterpart, f_{conv}, is shown in the inset of figure 33c and corresponds to a spectral broadening by 2.2 THz. Figure 33c shows the FTIR spectra after their convolution with the instrumental function; they are in a good agreement with the multi-THz measurements. We use this convolution function for any subsequent analysis of the pump-probe spectra: the spectra obtained by a theoretical calculation are transformed to the

time domain, multiplied by f_{conv} and transformed back. Only after this convolution step they are compared (fitted) to the experimental ones.

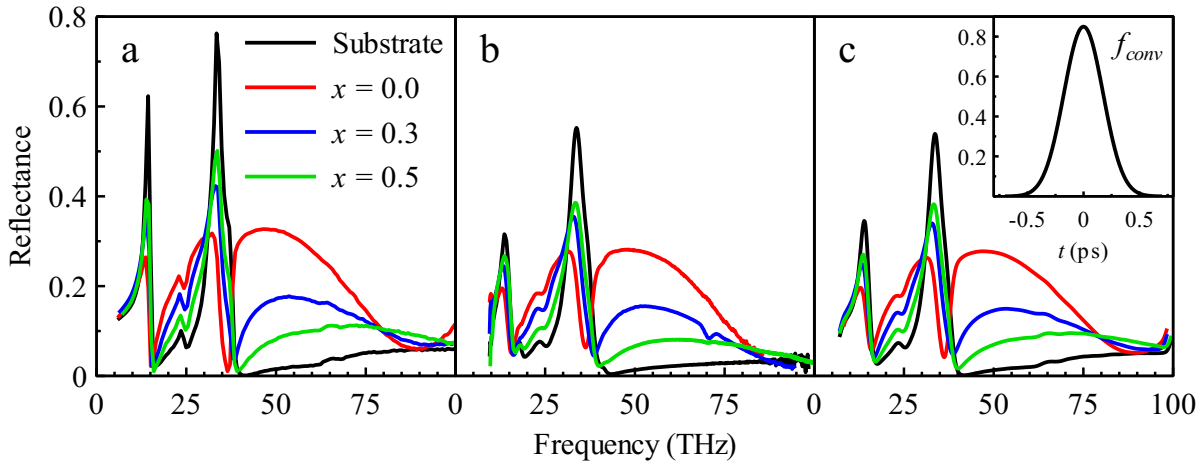

Figure 33. Spectra of the samples (x = 0.0, 0.3 and 0.5) and of SiO_2 substrate in the ground state measured by (a) FTIR spectrometer Bruker and (b) multi-THz technique. Figure (c) shows the FTIR spectra from panel (a) convoluted with an ad hoc spectral instrumental function f_{conv}.

4.4.2. Pump-probe measurements

Multi-THz –mid-Infrared photoconductivity in the Si NC networks was measured using the experimental setup described in section 3.3. The samples were optically excited from the substrate side; the optical pump at 388 nm (second harmonic of the fundamental beam) propagated through the substrate before exciting the Si NC multilayer on the opposite side. The fluence density was controlled by a set of neutral density filters inserted into the beam at the fundamental frequency. The multi-THz probing was set up in a reflection geometry (reflection at the front side of the sample) under normal incidence. Measurements were done at room temperature.

The measured transient spectra are shown in figure 34; the results are presented in the form of the transient power reflectance:

$$|R_{ex}|^2 = \frac{|E_r^{ex}/E_{inc}|^2}{|E_r/E_{inc}|^2} = \frac{|E_r^{ex}|^2}{|E_r|^2}, \tag{4.5}$$

where $E_r^{ex} = E_r + \Delta E_r$ is the reflected field on the photoexcited sample and E_{inc} is the incident field. Note that R_{ex} is not a differential quantity.

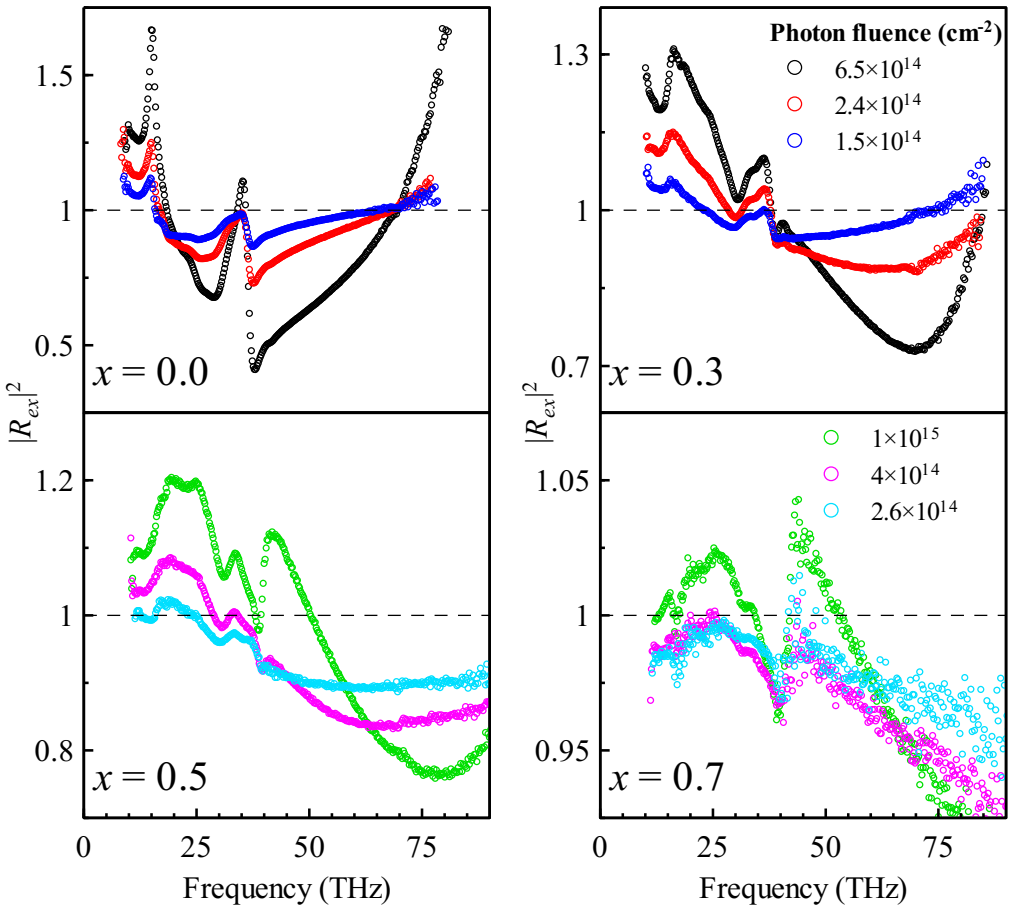

Figure 34. OPMIP reflectance spectra of the samples measured 10 ps after photoexcitation using 388 nm excitation wavelength.

It is quite hard to identify the conductivity resonance(s) by inspecting the experimental curves in figure 34 just by the eye. This is due to an interplay of the phenomena discussed above, namely due to an interaction with phonons in SiO_2 and due to an interference on the multilayer. However, we can make a few qualified comments based on the knowledge of steady-state spectra and on some model calculations. Such discussion is presented in the next paragraph.

4.4.3. Illustration using a simplified model system

Several model spectra are shown in figure 35; the left panel represents the steady-state power reflectance and the right panel shows the transient power reflectance. Here we consider sample $x = 0.0$, a homogeneous photoexcitation (i.e., homogeneous photoconductivity of NC Si layers along z), and we apply several simplified models of the substrate and of the NC layer. The conductivity spectra were calculated using the quantum mechanical approach for two different NC sizes d providing the resonances at significantly different frequencies (figure 35h,l).

In panel (a) showing unexcited Si layer on top of non-dispersive substrate we observe merely Fabry-Pérot interferences on the Si layer. To interpret the spectrum in panel (e) we must keep in mind that the photoconductivity provides a negative contribution to the refractive index of Si [$\mathrm{Im}\,\sigma > 0$ in panel (h)] thus making the period of spectral interferences larger. The

sequence of spectral maximum and minimum between 50 and 70 THz in panel (e) then corresponds to an effective shift of the interference minimum to the higher frequency. In general, a minimum in a steady-state spectrum can be shifted upon photoexcitation: a sequence maximum-minimum is then observed in the spectrum of $|R_{ex}|^2$ in the case of a blue shift and a sequence minimum-maximum is observed in the case of a red shift. The low-frequency feature in panel (e) is a result of the charge carrier confinement. In panel (i) the interference minimum approximately coincides with the conductivity peak, which is at the origin of an increased reflectance near 60 THz; the side minima are due to an interplay of the interference pattern and the resonant dispersion.

The spectra in panels (b) and (c) contain the phonons of SiO_2; namely influence of the substrate leads to a very sharp phonon features as observed in panel (c). The parts of the spectra of $|R_{ex}|^2$ will then exhibit a large experimental error in the close vicinity of the sharp dips (i.e., the fits of the experimental data are not required to be very precise close to such sharp features). The panels (f) and (g) show sequences of maximum-minimum pairs which express a shift at the phonon (~ 32 THz) and interference (~ 87 THz) features. Finally, the panels (j) and (k) demonstrate how deeply the reflectance spectra change when we insert small NCs into the Si layers.

From this brief analysis it follows that the particular form of the reflectance dispersion above the SiO_2 phonons (> 32 THz) is very important for small NCs, while larger NCs will mainly influence the dispersion below the phonon modes or partly overlap with the phonon region. The phonon region is influenced by an interplay of the conductivity of both large and small NCs; however, this is a spectral region with larger experimental error.

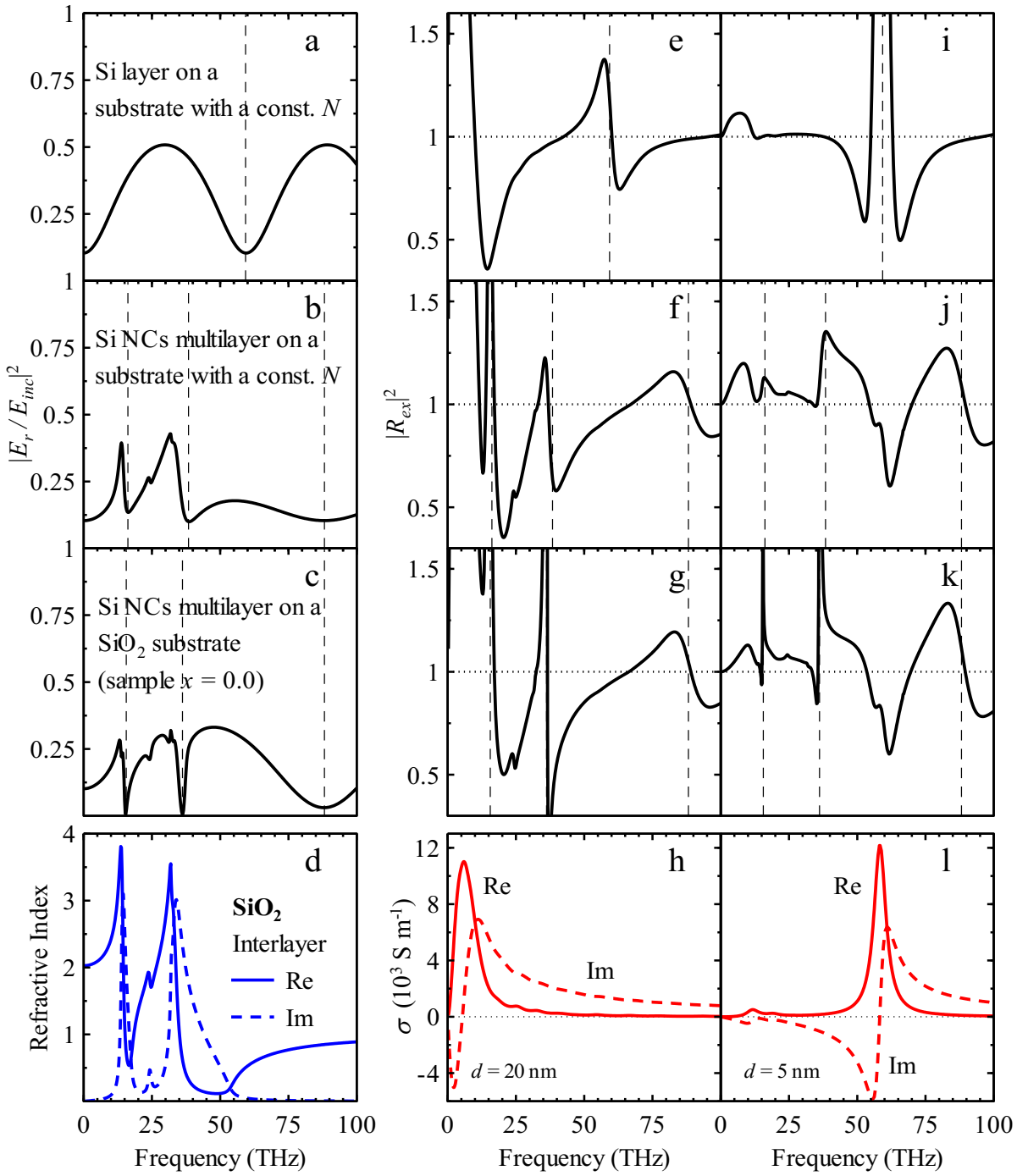

Figure 35. Power reflectance spectra calculated for a homogeneous 740 nm thick layer (which simulates the Si-NC/SiO_2 multilayer) on a substrate. (a-c) unexcited Si (steady-state spectra); (e-g,i-k) photoexcited Si NCs (transient but not differential spectra), where the conductivity σ calculated using the quantum mechanical theory for NCs with size $d = 20$ nm (panel h) is used for panels (e-g) and with size $d = 5$ nm (panel l) is used for panels (i-k). *Meaning of rows*. First row (a,e,i): 740 nm thick Si layer ($n_{\mathrm{Si}} = 3.41$ for unexcited Si) on a transparent non-dispersive substrate (n_{sub} = 1.95). Second row (b,f,j): Effective medium approximation of an Si-NC/SiO_2 multilayer on non-dispersive substrate; the refractive index of SiO_2 interlayers is shown in (d). Third row (c,g,k): Same as previous but with SiO_2 substrate. Dashed vertical lines indicate minima of the power reflectance.

4.4.4. Transient multi-THz – mid-infrared reflectance

In analogy with the previous THz investigations, we take into account the distribution of NC sizes in the samples using the integral:

$$E_r^{ex} = \frac{\int_{d1}^{d2} E_r^{ex}(d) w(d)\, \mathrm{d}d}{\int_{d1}^{d2} w(d)\, \mathrm{d}d}, \tag{4.6}$$

where we integrate over the variable d which controls E_r^{ex} through the carrier confinement encoded into the carrier mobility. Based on the experimental geometry, the field reflected on a photoexcited sample E_r^{ex} can be calculated using equations 2.50 and 2.51. Alternatively, a full numerical approach can be employed to solve the wave equation 2.7. In practice, since we should ensure the validity of the calculation over ultrabroad spectral range, we applied the fully numerical approach.

Now, the presence of the instrumental function in OPMIP measurements implies applying the convolution function f_{conv} separately to the calculated quantities $|E_r^{ex}/E_{inc}\,|^2$ and $|E_r/E_{inc}|^2$ in order to be consistent with the experimental procedure. Finally, we obtain the sought theoretical value of the quantity $|R_{ex}|^2$ from the convoluted spectra using equation 4.5.

4.4.5. Fitting model

Again, we consider a continuous distribution of NC sizes described by the log-normal law (equation 4.4). However, since the spectra in the whole multi-THz range are available now, we expect that the photoconductive contribution of the NCs of nearly all sizes may be experimentally detected. Therefore, we consider here a sum of two log-normal distribution functions, i.e., for the small ($f_{LN}^{small}(d)$) and large ($f_{LN}(d)$) nanocrystals. We relate the first one to sizes of single (electrically) isolated NCs whereas the second one corresponds to NCs conductively connected to clusters. Thus, we define the volumic density of NCs as follows:

$$w(d) = a\, d^2 f_{LN}^{small}(d) + b\, d^2 f_{LN}(d), \tag{4.7}$$

where the coefficients a and b are related to the filling fractions of small and large NCs s_{coh}^{small} and s_{coh} respectively through the volumes:

$$\frac{s_{coh}^{small}}{s_{coh}} = \frac{a \int_{d1}^{d2} d^2 f_{LN}^{small}(d)\, \mathrm{d}d}{b \int_{d1}^{d2} d^2 f_{LN}(d)\, \mathrm{d}d}. \tag{4.8}$$

The ratio of two integrals corresponds to a ratio of Si volumes related to the large and small NCs; the out-off-plane dimension (height) of the crystals is assumed to be fixed by the thickness of the layers. Thus, a/b can be understood as a proportion of the number of small NCs to the number of NC clusters.

Following the same procedure as it was done in the THz investigation of NCs (section 4.2.3), the mobility data for NC sizes between $d_1 = 4$ nm and $d_2 = 100$ nm were interpolated to obtain quasi-continues series of data as required for the fitting with integral equation 4.6.

The quasi-continuous database of $\mu(\omega)$, was prepared using the quantum mechanical approach (section 2.2.4) for 300 K and the dephasing time $1/\gamma$ = 60 fs.

As it was discussed in paragraph 4.4.1, the current investigation involving MIR frequencies is more sensitive to the thickness of the multilayers than previous investigation based on the classical THz spectroscopy. Therefore, EMT analysis of the steady-state measurements provides not only the refractive indices of the SiO_2 components n'_{SiO2}, n''_{SiO2} in the samples (figure 32) but also the average thickness of the Si rich and SiO_2 layers. In addition, average value of the MG shape factor K_{MG} and Si total filling fraction s in each sample were estimated quite carefully from the MIR steady-state spectra (in fact the importance of the shape factor becomes significant namely at higher frequencies). The relevant parameters obtained from the steady-state IR measurements are summarized in table 5. (Note that the values of K_{MG} are very close to the values of K_{coh} obtained from the THz experiment and shown in table 4).

Sample x:	s	K_{MG}	Averaged thickness of Si NCs layer (nm)	Averaged thickness of SiO_2 layer (nm)
0.0	0.99	2	3.1	4.3
0.3	0.84	1.5	4.05	4.0
0.5	0.42	2.0	4.5	4.0

Table 5. Samples parameters obtained by the fit of the steady-state IR measurements based on the MG and parallel capacitor EMT approach.

All the parameters provided by the steady-state analysis of the samples were fixed during the subsequent fitting of the transient OPMIP data. In addition, the parameters corresponding to the incoherent component of the conductivity ($\mu_{RT}, s_{inc}, K_{inc}$) were taken from the THz experiment (see table 4). Indeed, this part of the photoconductive response was described by the model of constant mobility; therefore, we consider its even contribution in the THz and multi-THz – mid-infrared ranges. Hence, we can also estimate the total volumetric filling fraction of the NCs exhibiting the coherent carrier motion as follows:

$$s_{coh}^{total} = s - s_{inc.} \tag{4.9}$$

As a result, analysis of the OPMIP spectra involves only two fitting parameters for each distribution function (i.e., $d_0, \delta, d_0^{small}, \delta^{small}$) and the ratio a/b introduced in equation 4.8. The parameters B and D of the effective medium model are related to the sample morphology and they are defined by formulas 2.42.

The optical parameters of pure silicon were taken from [113]: $\alpha_{Si}^{388nm} = 2 \times 10^5\ cm^{-1}$, $n_{Si}^{388nm} = 6.06$. We infer the effective absorption coefficient α from the measured absorbance data shown in figure 23. This is an approximation since these measurements were performed down to 405 nm while our excitation wavelength in OPMIP experiments was 388 nm. We are aware that in this spectral range the change of the extinction coefficient may be

non-negligible. However, taking into account the experimental error in the pump pulse fluence measurements, this represents a good approximation in our view.

4.4.6. Results and Discussion

The model expressed by equation 4.6 was used to fit the OPMIP experimental spectra, and the comparison of the model and experimental data for the samples x = 0.0 and x = 0.3 is shown in figure 36. The corresponding distribution functions are presented in figure 37 and the obtained values of the filling fractions s_{coh} and s_{coh}^{small} are given in table 6.

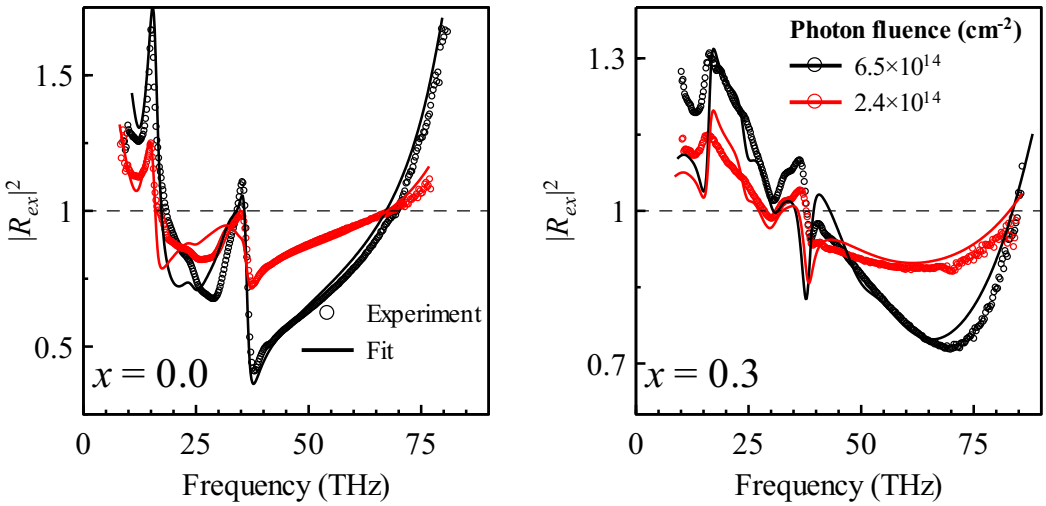

Figure 36. OPMIP spectra of the samples with x = 0.0 and x = 0.3. Circles: experimental data, lines: fits of the data by equation 4.6.

There is a good agreement between the results of the THz and multi-THz – MIR investigations for the sample with x = 0.0. Indeed, the distribution functions f_{LN} describing large NCs obtained via THz and multi-THz – MIR experiments (black and red lines in figure 37a) are comparable as well as values of the volumetric filling fraction s_{coh} related to the large NCs (blue columns in table 6). A result for the coefficients a and b implies that there are about 30 small (individual) NCs per each large one (NC aggregate) in the sample.

In the case of the sample with x = 0.3, we also have reasonable agreement of the functions f_{LN} extracted from the OPTP and OPMIP data (peak position of the black and red lines in figure 37b). However, the value of s_{coh} evaluated from the multi-THz – mid-infrared measurements is considerably lower compared to the results of the THz investigation (10% compared to 50%) suggesting about 35 small NCs per each NC cluster. Thus, significant amount of the silicon volume forms small NCs described by f_{LN}^{small} in this sample. This discrepancy may be explained by the decrease in the sensitivity of the experiment in the THz spectral range with the decrease of the NCs size in the sample (see figure 27) compared to the sample with x = 0.0.

Sample	a/b	$s_{coh}^{total}(\%)$ (from OPTP)	$s_{coh}(\%)$		$s_{coh}^{small}(\%)$ (from OPMIP)
			(from OPTP)	(from OPMIP)	
$x = 0.0$	30	82	36	30	52
$x = 0.3$	35	66	50	10	56

Table 6. The volumetric filling fractions of the NCs with coherent motion of the electron carriers obtained from the fit of the OPTP and OPMIP experimental spectra.

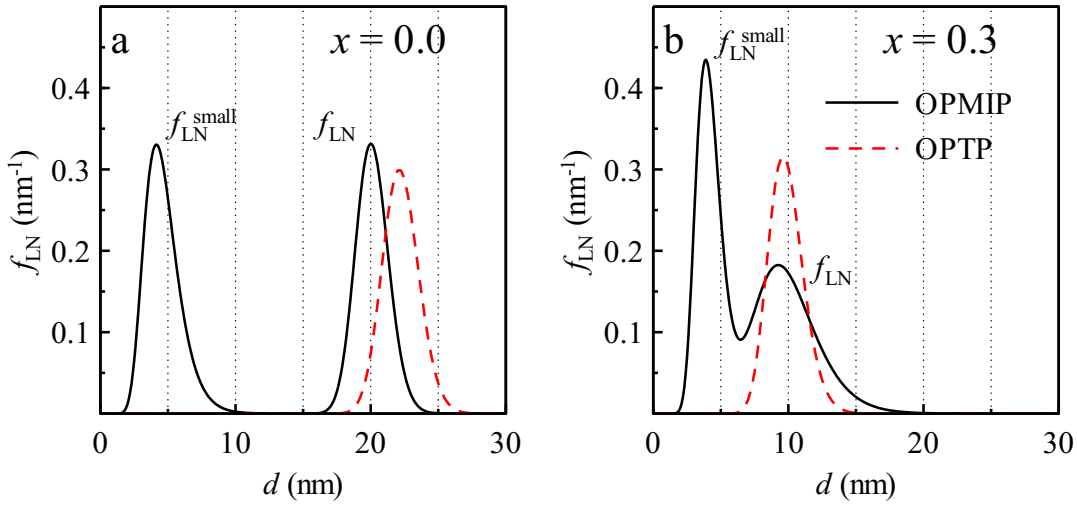

Figure 37. Size distribution of NCs for the samples with $x = 0.0$ and $x = 0.3$. Black lines: results of the current OPMIP study, red lines: results of the previous OPTP investigation (section 4.3).

According to the results for the samples with $x = 0.0$ and $x = 0.3$, the average size of the small NCs also slightly decreases with the decrease of silicon amount in SiO_x layers. In spite of the relatively small change, compared to the shift of f_{LN} for the large structures, it may significantly influence the outcome of the study: indeed, following the quantum model, for such small NCs the conductivity resonance may shift even out of the range of OPMIP sensitivity in this case. Therefore, OPMIP spectra of the samples with higher values of x could hardly be fitted in the current state of the analysis. This seems surprising considering the results of the THz investigation (sections 4.2 and 4.3), where the employed model provided a reasonable fit of the conductivity spectra for the samples with, among others, $x = 0.5$ and $x = 0.7$. However, unlike in the THz spectroscopy, the ultra-broad frequency range covers a number of overlapping phenomena discussed in this chapter. Therefore, since the OPMIP sensitivity significantly decreases for NCs smaller than 4 nm, a correct interpretation of the sample response becomes more difficult and would require more precise information about the geometry of NCs in order to evaluate properly the microscopic mobility. In the case of the THz spectroscopy, on the other hand, the reduced sensitivity may result in overestimation of some parameters while still providing reasonable agreement between experimental and calculated curves, as it is shown for the sample with $x = 0.3$, where the filling fraction s_{coh} was found to be five times larger compared to the results of the OPMIP investigation.

4.5. Conclusion

We successfully applied our approach, based on the solution of the wave equation for the electromagnetic waves in the photoexcited media with mixed dielectric properties, to a photoconductive response of quasi-two-dimensional silicon NC networks in the THz – mid-infrared spectral range. The THz quantum mobility model (section 2.2.4) including the drift-diffusion current describes properly the charge carrier transport in the nanocrystals providing an opportunity to estimate electron confinement lengths in the samples: the concerted study by the time-resolved OPTP and OPMIP spectroscopies has shown that the samples indeed present the target 4-5 nm sized Si NCs (as suggested by TEM) but they also contain a non-negligible amount of larger NCs which may be interpreted as clusters of smaller nanocrystals merged during their growth. According to the OPMIP investigation, the proportion of individual NCs to clusters for the samples with $x = 0.0$ and $x = 0.3$ is approximately defined as thirty to one. The clusters dominate the THz photo-conductivity spectra. Their size decreases with decreasing amount of silicon in Si-rich SiO_x layers; this correlates with a better NC size control technologically achieved for samples with smaller amount of Si.

We have shown that our comprehensive approach is a powerful tool that allows to disentangle and evaluate a number of phenomena primarily responsible for the measured response at given probing frequencies, in particular, phonons in the fused silica components of the samples, optical interference of the mid-infrared wave within the multilayer, quantum confinement of the photo-carriers within NCs and the localized plasmon resonance. Nevertheless, there is still a lack of in-depth understanding of the photocarrier properties related to the disordered structure of the samples. Namely, both THz and multi-THz – mid-infrared study yield the picture of a percolated Si layer with a confined response of the photocarriers for the sample with the highest amount of silicon ($x = 0.0$) suggesting some kind of energy barriers among the ~20 nm-sized clusters of NCs. This makes the assumption of the infinite depth of the potential wall in the quantum mobility calculations not entirely justified. The barriers ought to depend on the conditions of NC interfaces and may also determine the contribution to the conductivity interpreted here as incoherent electron motion. However, any reasonable assessment of NC interface properties is hindered by the complex sample morphology. We are hardly able to describe the exact dispersion of SiO_2 in both isolating layers and in NCs layers where it plays a role of the matrix in the effective medium approach. An observed significant modification of SiO_2 spectra (figure 32), caused by the strains in thin films and by structural and stoichiometric defects, suggests also a significant modification of surface properties of the silicon nanocrystals. Moreover, the approximation of two continuous size distribution function is a rather rough estimation of the real NC size distribution in the samples. Thus, accurate evaluation of the NC band potentials defining charge carrier confinement is practically impossible.

We were able to extract from the data valuable information about the samples' conductive properties. This information, nevertheless, remains only limited. Therefore, even though the superlattice approach [3] using nitrogen-free PECVD [100,101] is an advanced technique for the nanocrystal size and quality control, it is not able to provide the size regularity required for the determination of the electron mobility in a single nanocrystal without

significant averaging effects. This conclusion inspired us to employ lithographic techniques of the sample preparation in order to apply our analytical approach to perfectly ordered regular nanostructures described in the following chapter.

5. Charge transport in single-crystalline GaAs nanobars.

This chapter is devoted to our research of arrays of ultimate-quality single-crystalline GaAs nanobars prepared by electron-beam lithography in a molecular-beam-epitaxy-grown GaAs layer transferred onto an electrically insulating and optically and terahertz transparent sapphire substrate. Such a highly ordered structure constitutes a promising system for analysis of the carrier confinement and of the depolarization field effect in the THz frequency range.

Measurements of ultrafast terahertz photoconductivity at 300 and 20 K in an array of such aligned nanobars by time-resolved terahertz and multi-terahertz spectroscopy and by time-resolved terahertz scanning near-field microscopy allowed an in-depth understanding of the nanoscale electron motion inside the nanobars. A detailed analysis was performed in terms of quantum mechanical calculations of the mobility of carriers and in terms of plasmonic resonance controlled by photocarrier density. Apart from the careful evaluation of sample morphological properties, our investigations reveal a band bending close to the nanobar surfaces and its prominent effects on the picosecond charge carrier dynamics, leading to an enhanced localization of electrons at longer times. We thus demonstrate that terahertz spectroscopy proves to become an important tool for the investigation of the role of nanostructure surfaces.

Indeed, band-bending strongly influences charge transport properties of semiconductors, and it stays at the origin of the functionality of many fundamental electronic components like diodes or transistors. The profile and extent of the band-bending are inherently controlled by the state of the semiconductor surface and its vicinity. Direct electronic probing of the band-bending profile and its impact on the charge transport is a great challenge, since attachment of probing electrodes inevitably modifies the properties of the semiconductor surface. Details of the band-bending are even more important in nanostructures since the surface to volume ratio increases with decreasing nanostructure size.

Section 5.1 gives details on the sample preparation procedure and sample morphological properties provided by microscopy techniques. Section 5.2 is devoted to the investigation of the THz photoconductive response of the structures combining several experimental approaches. The corresponding results were summarized and published in [5].

5.1. Sample

Our aim was to fabricate and study a regular array of nanobars with well-defined material properties and morphology. We expected that in highly ordered samples and by performing experiments with variable temperature and variable pump power, one can disentangle the effects due to the localization of charges inside nanostructures and the depolarization effects due to spatial separation of charges in inhomogeneous samples. One of crucial requirements was imposed on the substrate properties: it should be free of background conductivity and photoconductivity. In other words, the substrate should be electrically

insulating (undoped) and also transparent for optical and THz radiation (no doping by photoexcitation).

5.1.1. Failure of $In_{0.53}Ga_{0.47}As$ on semiconductor substrate

Our initial attempt was to investigate the respective role of the depolarization fields and of the localization of carriers inside the $In_{0.53}Ga_{0.47}As$ nanobars on high-resistivity InP substrate. $In_{0.53}Ga_{0.47}As$ is a technologically important semiconductor with the energy bandgap of $E_g = 0.74$ eV exhibiting low dark current and a high electron mobility at room temperature. InP was selected as substrate since $In_{0.53}Ga_{0.47}As$ / InP is a commercially available structure and since its larger energy gap of $E_g = 1.34$ eV should allow avoiding the photogeneration of free carriers inside the substrate. 400 nm thick film of $In_{0.53}Ga_{0.47}As$ on InP substrate was purchased from MTI corporation (film grown by MOCVD). The nanostructures were prepared by etching of the $In_{0.53}Ga_{0.47}As$ layer using electron beam lithography. The resulting structures consisted of regular trapezoidal nanobars with the following parameters of the cross section: height – 400 nm, bottom base – 550 nm, top base – 130 nm (figure 39). The fabrication protocol allowed us to prepare perfectly aligned structures covering an area 1.5×1.5 mm^2.

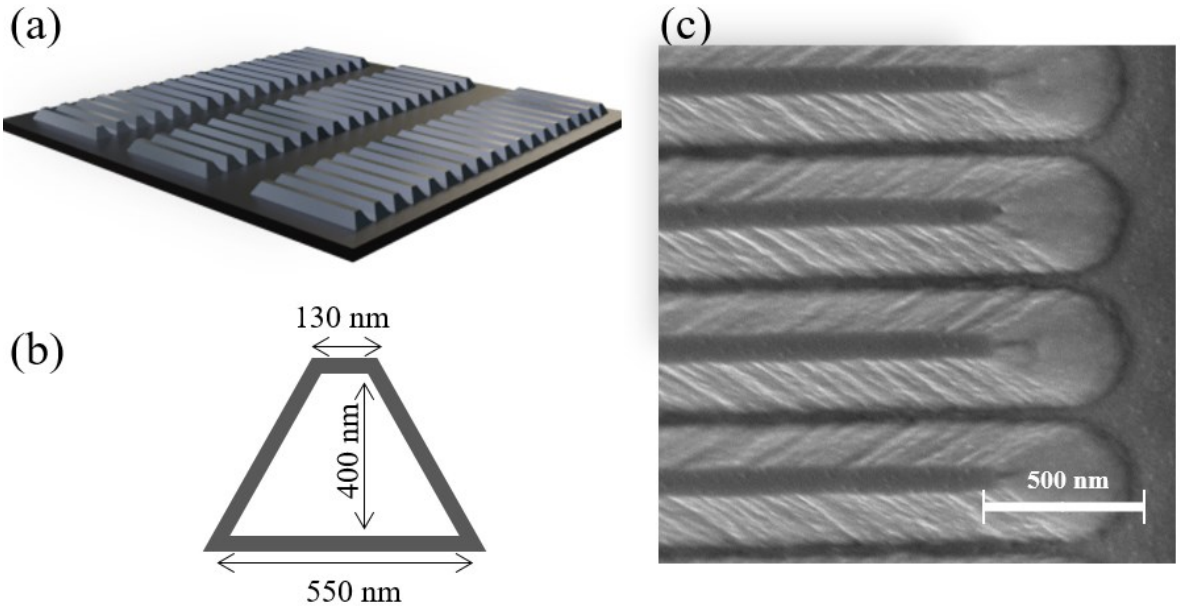

Figure 38. $In_{0.53}Ga_{0.47}As$ structures on InP substrate. a) Scheme of the nanobars array. b) Sizes of nanobar cross section. c) SEM image of the structures.

We expected to measure THz response of non-percolated nanostructures photoexcited by near-infrared pulses at 1.27 μm wavelength. Indeed, with the corresponding photon energy of ~ 0.98 eV does not reach the width of the bandgap of InP. However, a number of experiments (at both 300 K and 20 K temperatures) revealed unavoidable photoexcitation of the substrate via two-photon absorption process leading to a strong electrical percolation among the nanobars. The measured transient THz spectra (figure 39) were thus dominated by a Drude response of electrons in the conduction band of InP. The increase of ΔT_{norm} with the incident photon fluence indicates a nonlinear (two-photon) absorption process. Note also in figure 39 the large magnitude of the measured signal compared to the one obtained later with good

quality GaAs nanobarns (figure 45); this is a strong indication that the signal comes here essentially from the bulk part of the sample (InP substrate).

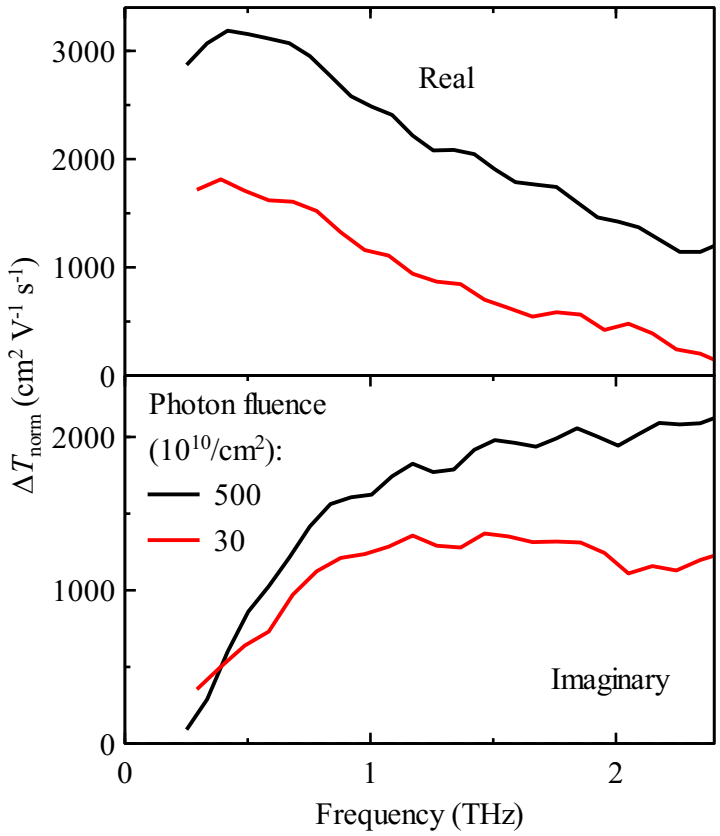

Figure 39. Normalized transient transmission ΔT_{norm} of the $In_{0.53}Ga_{0.47}As$ / InP sample measured 10 ps after photoexcitation at room temperature for THz polarization across the nanobars.

5.1.2. GaAs structure transferred on sapphire substrate

Here we combined the growth of a homogeneous thin GaAs film by molecular beam epitaxy (MBE), its subsequent transfer onto sapphire substrate and, finally, its structuring by electron beam lithography. The physical properties of the nanoelements are inherited from the well-defined properties of the pristine film; its quality is evidenced by DC electron mobilities as high as ~10^5 cm^2/Vs at low temperatures, see e.g. [114] where the data were reported for similar grown films.

The crucial step for our study is a transfer of the as-grown GaAs layer onto sapphire substrate prior to the electron beam lithography.

Figure 40 represents some important technological steps of the sample preparation. First, MBE technique was employed to deposit a series of layers on top of a (001) GaAs substrate in the following order: 100 nm thick GaAs buffer layer, 100 nm thick interlayer of AlAs and 700 nm thick layer of GaAs (the target sample layer). In this arrangement, however, the optical excitation beam would be absorbed not only in the sample GaAs layer, but also in the GaAs substrate where, in such a case, the photoconductivity signal would exceed the one expected in the nanobars. Indeed, the THz mobility of carriers in the homogeneous bulk is typically significantly higher than the one in nanostructures [84]. For this reason, the sample

layer was transferred onto a terahertz and optically transparent substrate, (0001)-oriented Al_2O_3 wafer, where free carriers are not generated upon illumination by our laser pulses. The transfer procedure, which we followed, was previously described by E. Yablonovitch et al. [115]. The top GaAs layer was covered by a drop of wax (Apiezon W dissolved in trichloroethylene), which was subsequently air dried (figure 40a). Next, the AlAs interlayer accessible from the sides was etched in a solution of 10% hydrofluoric acid for 8 to 12 hours, thus disconnecting the wax-stabilized GaAs film from the GaAs substrate (figure 40b). Subsequently, the GaAs film was transferred onto the top of the Al_2O_3 substrate where it adhered due to van der Waals forces (figure 40c). The sample was then rinsed with trichloroethylene to remove the wax (figure 40d). In the final stage, an array of nanobars (covering an area of 3×3 mm^2 on top of Al_2O_3) was made from the continuous GaAs film by means of electron-beam lithography (figure 40e).

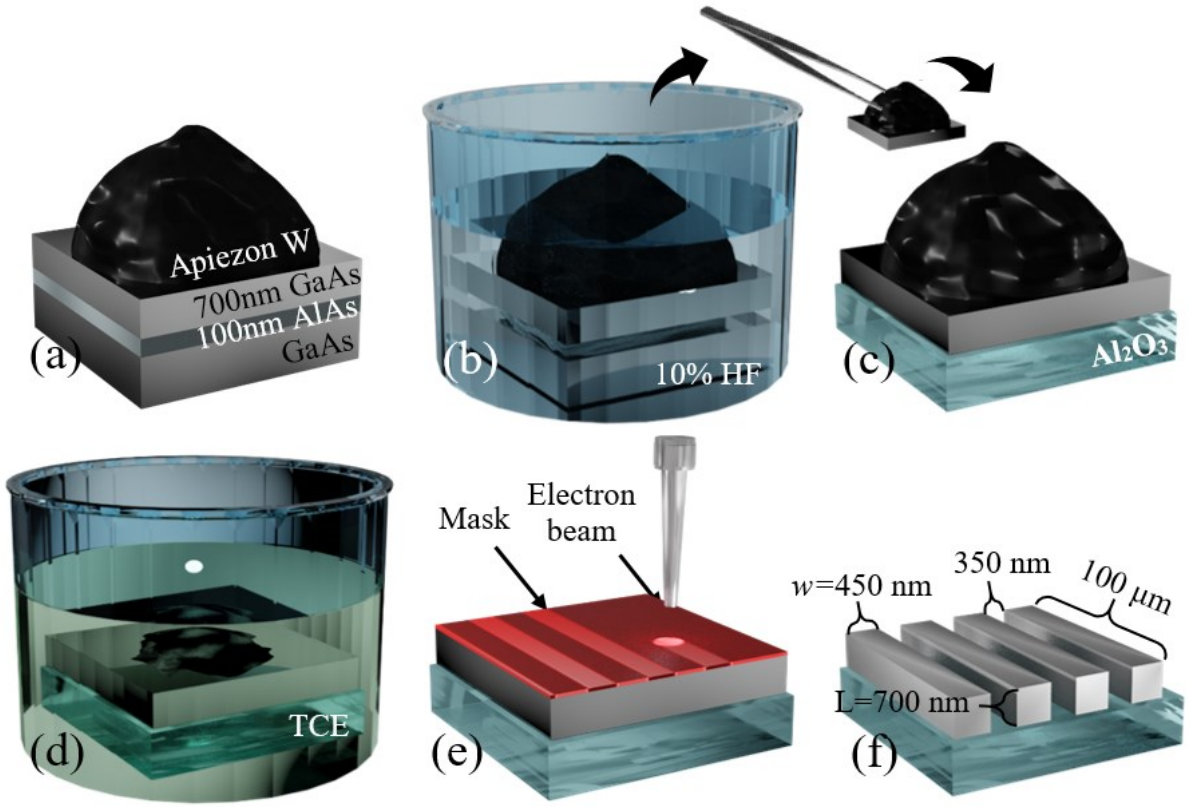

Figure 40: Schematic representation of the sample preparation procedure: (a) wax drop attached on top of the initial structure as deposited by MBE (700 nm GaAs / 100 nm AlAs / 100 nm GaAs buffer / GaAs substrate); (b) etching of the AlAs interlayer and (c) transfer of the GaAs film on an optically transparent substrate; (d) washing out of the "cup" in trichloroethylene (TCE); (e) electron beam lithography of the GaAs film and formation of nanobars; (f) final dimensions and geometry of nanobars.

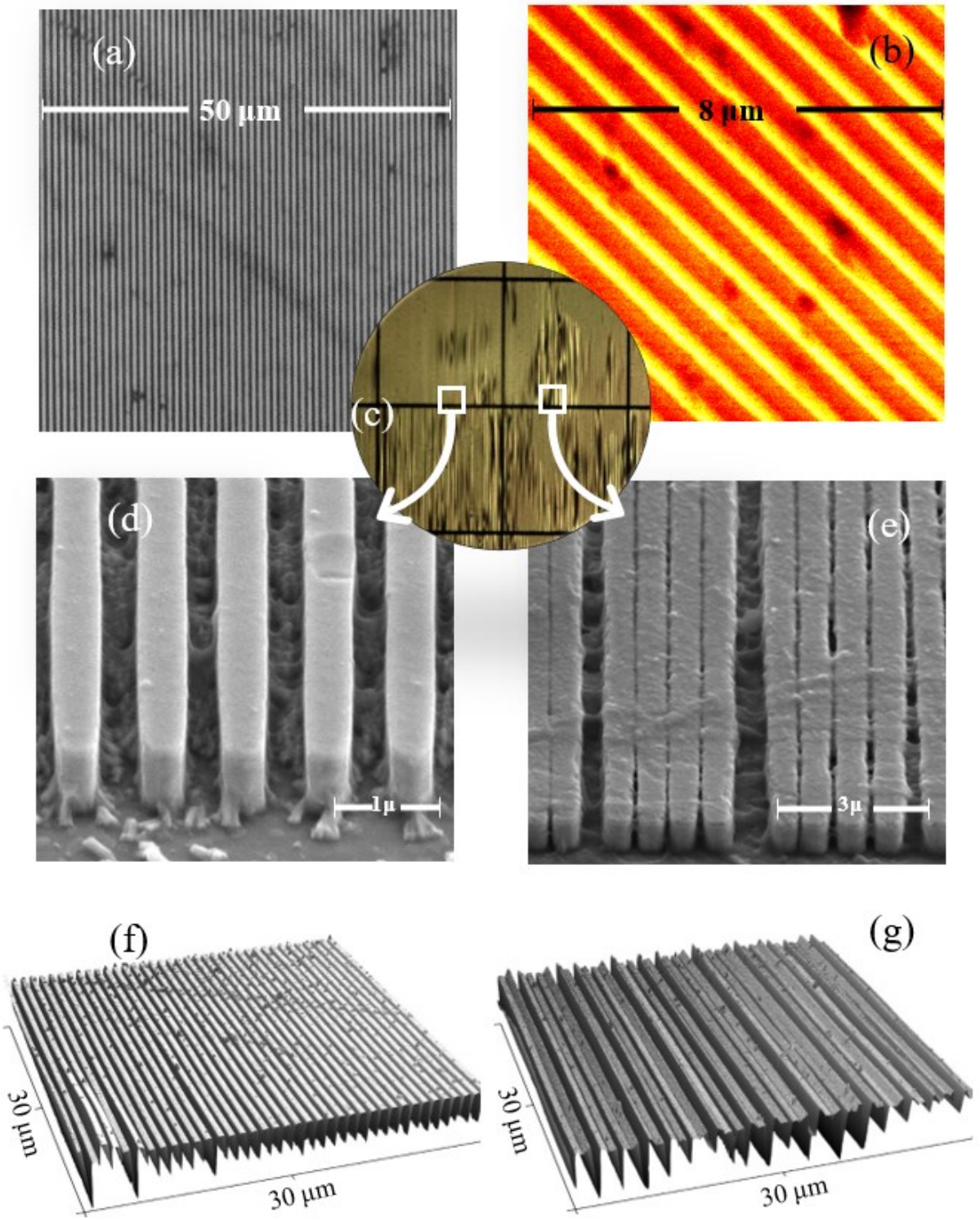

Figure 41. Images of investigated GaAs structures on sapphire substrate. (a,c) Optical microscope images: at smaller magnification (c), perfectly ordered nanobars appear as uniform areas whereas the areas with the slid and merged nanobars contain contrasted features. (b) near-field image obtained by THz-SNOM: the yellow areas correspond to the gaps between the bars. (d,e) scanning electron microscope (SEM) images of perfectly ordered (d) and bunched (e) GaAs nanobars on the sapphire substrate. (f,g) AFM images of perfectly ordered (d) and bunched (e) GaAs nanobars on the sapphire substrate.

The final structure consisted of a series of 700 nm high, 450 nm wide and about 100 μm long nanobars attached to the sapphire substrate by van der Waals interactions; the gap between individual nanobars was 350 nm. These nanostructures formed 100×100 μm^2 squares and the whole 3×3 mm^2 sample was paved by these squares with their spacing of about 1 μm (see figure 40 summarizing the dimensions and figure 41 showing also SEM, AFM, SNOM and optical microscope images). At some places the sample was very nicely ordered exhibiting the nominal periodicity of 800 nm (figure 41a,d,f); however, at some places the contact between the nanobars and the substrate was worse and individual nanobars or groups of nanobars slid along the surface of the substrate forming wider and/or partially percolated structures (figure 41e,g). This was probably due to the tensions in the GaAs film built up during the transfer, which could significantly reduce the van der Waals adhesion to the substrate.

In the case of nanostructures, it is an advantage to have support by microscopy techniques for an investigation of carrier conductivity. In our study the optical microscopy of the sample can provide only overall information about sample morphology due to the specific dimensions of the structures, i.e., width of the individual nanobars is comparable to the wavelengths of the visible light. Therefore, the atomic force microscopy (AFM) was employed. However, precise measurements of the sample morphology via the AFM technique are prevented to the certain extent due to the relatively narrow and deep gaps between the structures with respect to the dimensions of the AFM tip. Despite of that, the measurements allowed us to verify the height and the period of the aligned nanobars as well as to determine the presence and character of the bunched structures. Regarding the electron microscopy, there are fundamental obstacles related to the non-percolated character of the nanostructures and insulating substrate in our sample. Therefore, the whole front side (top) of the sample was covered by a ~5 nm thick carbon layer in order to perform SEM measurements. Obviously, this procedure inevitably causes a dramatic change in the conductive properties of the whole sample making it completely percolated. Considering an irreversible character of this change, we performed SEM investigation of the sample at the final stage of our study, i.e., when all the THz conductivity experiments were finished.

5.2. THz photoconductivity

We studied photoconductive response of the sample using both far- and near-field THz spectroscopy. In every case the photoexcitation of the sample was done at 800 nm wavelength that corresponds to a photon energy of about 1.55 eV. Considering the energy gap of GaAs (E_g =1.42 eV at room temperature [116] and 1.52 eV at 20 K [117]), the photocarriers in our structures are generated via single-photon absorption mechanism. Optical transmittance and reflectance of the sample upon photoexcitation was experimentally determined in order to evaluate the fluence of the pump pulse absorbed in the sample and the carrier concentration inside the nanobars. The grating-like form of the structure leads to diffraction and waveguiding effects in the optical range and to enhancement of the optical absorption that depends on orientation of the nanobars with respect to the polarization of the pumping beam. In particular, in the parallel configuration the value of an absorption coefficient of the sample at the chosen optical wavelength was determined as 2.7×10^6 m^{-1}. We denote this coefficient as α_{eff} as it corresponds to effective absorption in the structured sample. The local absorption coefficient

(i.e., the one determining the concentration of carriers inside GaAs nanobars) can be calculated using GaAs filling factor s as follows:

$$\alpha_{loc} = \frac{\alpha_{eff}}{s}. \tag{5.1}$$

From the microscopic images we can estimate s~0.55. Thus, the local absorption coefficient $\alpha_{loc} = 4.9\times10^6$ m^{-1}. Note that this value is more than three times higher than the bulk GaAs absorption coefficient ($\alpha_{\mathrm{GaAs}} = 1.4\times10^6$ m^{-1} [118]).

At the first stage, the THz photoconductivity was measured in a conventional OPTP experimental setup described in section 3.1. The pump beam at 800 nm was expanded by a diverging lens to ensure that the exposed part (2.5 mm in diameter) was photoexcited homogeneously. The pump-beam fluence was controlled over nearly three orders of magnitude using a combination of neutral density filters and a variable attenuator based on a thin film polarizer. Figure 42 shows the kinetics of the signal decay in the nanobars after photoexcitation at room temperature; the decay time is of 130 ps. The transient THz spectra were measured at 20 and 300 K at a pump-probe delay of 10 ps; the spectra are presented in the form of the normalized transmission function ΔT_{norm} (equation 2.48) as a function of the frequency and carrier density.

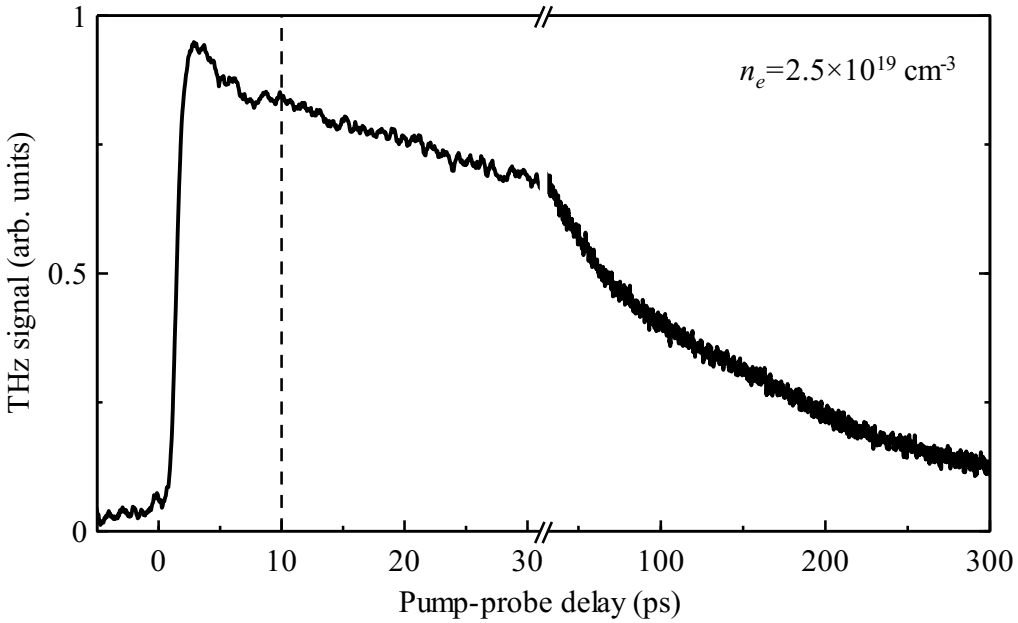

Figure 42. Dynamics of THz conductivity of photoexcited carriers in the GaAs nanobars measured at perpendicular arrangement of the bars with respect to the THz electric field vector. Dashed line corresponds to the pump-probe delay where the time-resolved THz spectra were subsequently measured.

It has been shown that in the case of a weak photoexcitation ($\Delta E \ll E$) and of a thin film sample (sample thickness L is much smaller than the probing wavelength) the solution of the wave equation 2.7 for the transient transmitted THz field (equation 2.16) is directly related to the sheet conductivity of the photoexcited film [68,103]:

$$\Delta T_{\mathrm{norm}} = \frac{1}{e_0 \phi} \int_0^L \Delta\sigma(z) dz. \tag{5.2}$$

In a spatially homogeneous film absorbing the entire excitation fluence, the right-hand side simplifies to the product of the quantum yield and mobility of photocarriers, i.e., it represents an average single-carrier response.

5.2.1. THz electric field parallel to the nanobars

For a basic characterization of the samples we measured the THz mobility of photocarriers in the as-grown GaAs film (figure 43) and the THz mobility component parallel to the nanobars in the patterned sample (figure 44). In both cases the fitting procedure was based on the Drude model of the carrier mobility (equation 2.18) providing a good agreement between the experimental and calculated curves (figures 43 and 44).

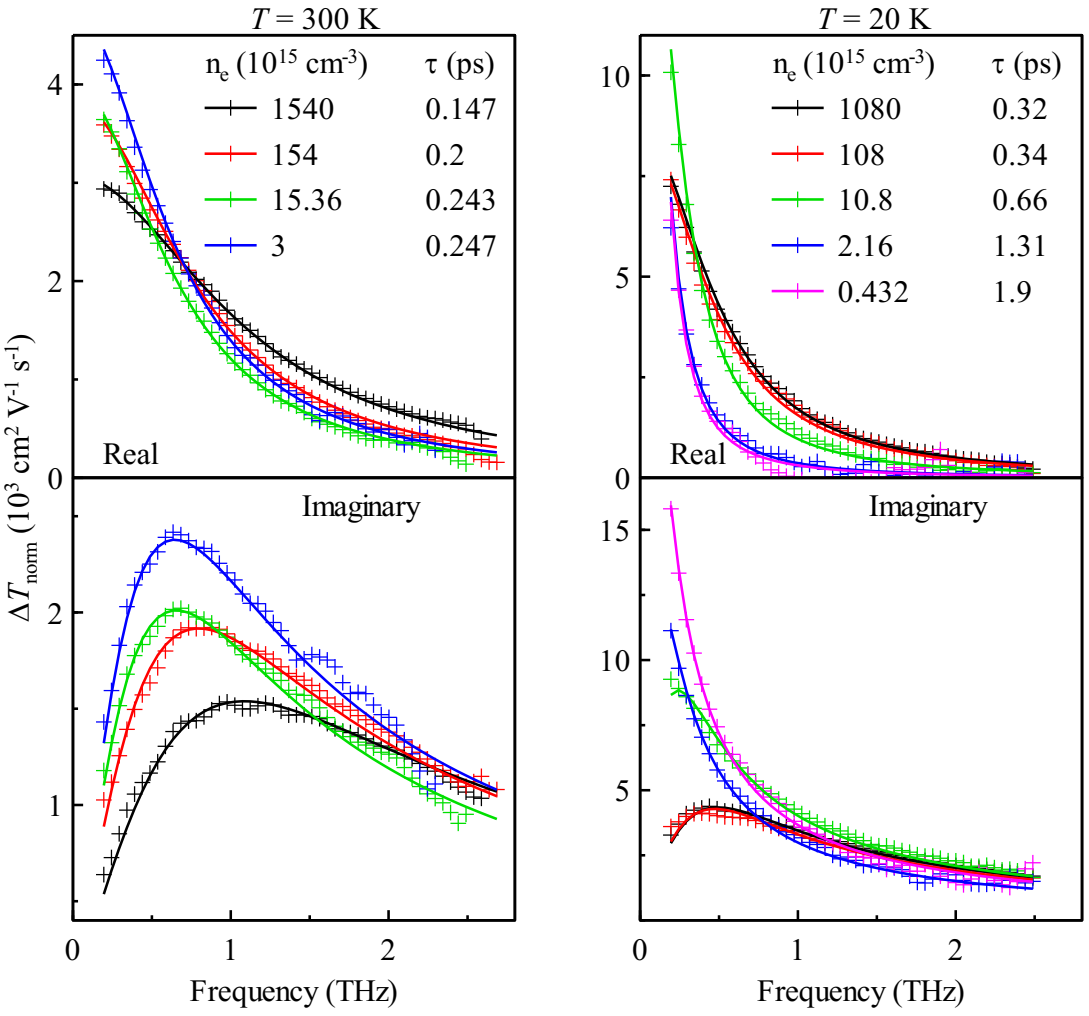

Figure 43. Normalized transient transmission ΔT_{norm} of the GaAs film (symbols: measurements 10 ps after photoexcitation; solid lines: fit of the data by the Drude model (equation 2.18)).

One can observe quantitative agreement in evolution of the scattering time τ measured in the film and nanobars. Under weak photoexcitation conditions we found the DC mobility

value of $\mu \approx 6.5 \times 10^3$ cm^{2}V^{-1}s^{-1} at room temperature (concentrations of photocarriers $n_e \approx 2 - 5 \times 10^{15}$ cm^{-3}) and $\mu \approx 5 \times 10^4$ cm^{2}V^{-1}s^{-1} at 20 K (concentration of photocarriers $n_e \approx 0.5 - 1 \times 10^{15}$ cm^{-3}) in both cases. We conclude that the films have a very good quality and that the transport properties are not deteriorated during all the manipulations related to the film transfer and pattering. In this respect, the resulting nanostructures are superior to many excellent advanced materials like InP nanowires grown by metalorganic vapor phase epitaxy on a patterned substrate where the growth process may considerably alter the material (e.g., introduce defects like stacking faults) [119,120].

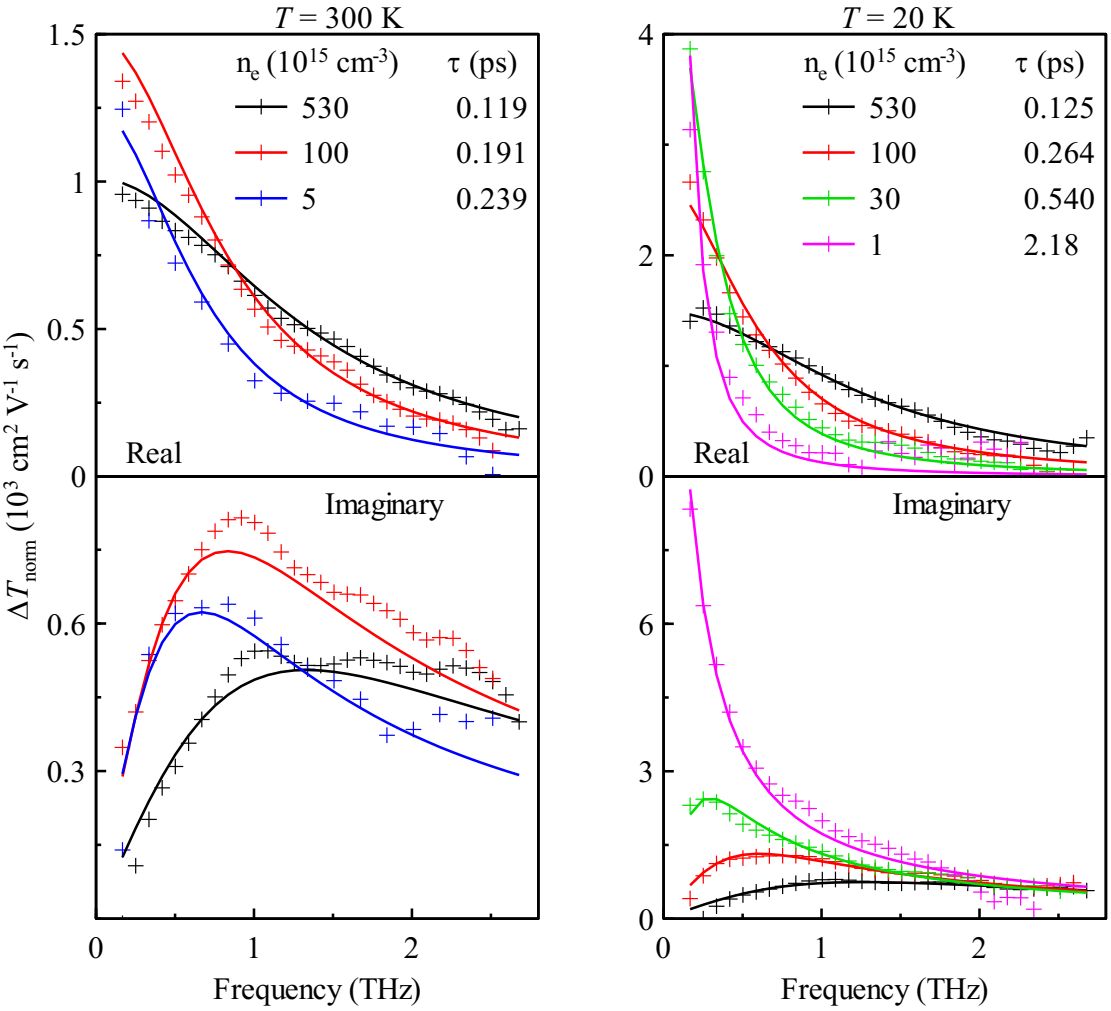

Figure 44. Normalized transient transmission ΔT_{norm} of the GaAs nanobars oriented in parallel to the polarization of the probing THz field (symbols: measurements 10 ps after photoexcitation; solid lines: fit of the data by the Drude model (equation 2.18)).

5.2.2. THz electric field perpendicular to the nanobars

All the subsequent far-field THz experiments were performed with the THz beam polarization (electric field vector) carefully adjusted perpendicular to the nanobars, i.e., the transport of charge carriers across the nanobars was probed. Figure 45 shows OPTP experimental spectra of the normalized transmission function ΔT_{norm}.

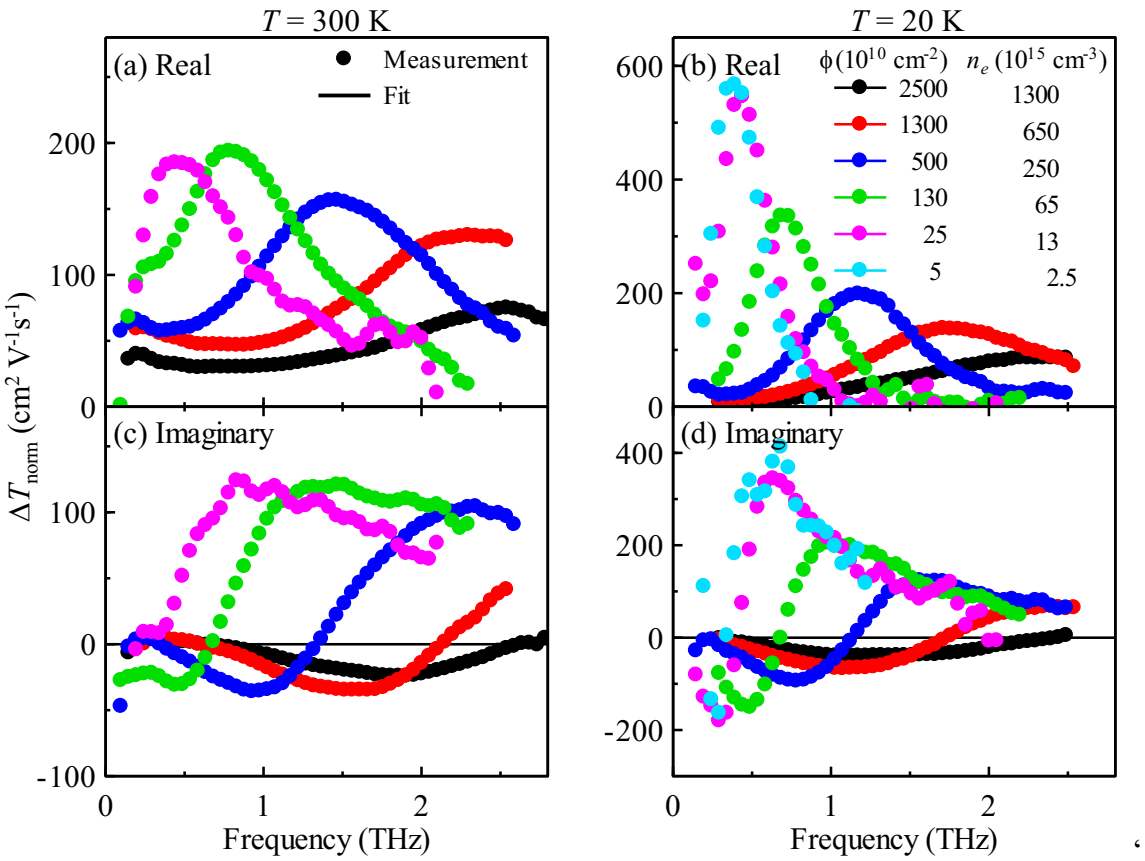

Figure 45. Normalized transient transmission ΔT_{norm} of the GaAs nanobars oriented perpendicular to the polarization of the probing THz field (measurements 10 ps after photoexitation).

The spectra feature a broad resonance peaking at a non-zero frequency; this is characteristic for the localized response of charge carriers. The observed blue-shift of the conductivity peak with increasing excitation power (i.e., carrier concentration) is a clear signature of the depolarization fields effect (localized plasmon resonance) [86]. Therefore, we perform our analysis of the sample photoconductive response in the framework of the effective medium theory, using our VBD EMT model (section 2.2.6) that allows accurate evaluation of this effect. For a homogeneous photoexcitation along z of the nanostructured film, equation 5.2 with an effective conductivity defined by VBD formula (2.41) yields

$$\Delta T_{\mathrm{norm}}(\omega) = \alpha_{loc} L\, \mu(\omega) \left[V + \frac{B}{1 + iD \frac{e_0 n_e}{\varepsilon_0 \omega} \mu(\omega)} \right], \tag{5.3}$$

where $n_e = \alpha_{loc} \phi$ is the carrier concentration inside the nanobar. In nanostructured samples the right-hand-side of equation 5.3 approaches the microscopic mobility (or, more precisely, $\alpha_{loc} L\, \mu(V + B)$) at very low pump fluences. At higher fluences, it reflects the depolarization fields of the inhomogeneous structure quantified by D.

In partly disordered structures, which we encounter in the studied samples, a distribution of the D parameter representing the distribution of morphological properties needs to be considered. For this purpose, equation 5.3 can be generalized using the integral

$$\Delta T_{\mathrm{norm}}(\omega) = \alpha_{loc} L\, \mu(\omega) \left[V + B \int \frac{f_G(D)\, dD}{1 + iD \frac{e_0 n_e}{\varepsilon_0 \omega} \mu(\omega)} \right], \tag{5.4}$$

where $f_G(D)$ is a suitably chosen distribution function (with normalization $\int f_G(D) dD = 1$). Indeed, the experimentally observed broadening of the conductivity peak and the decrease of its amplitude (figure 45) upon increase of the excitation photon fluence are attributed to the distribution of the D parameter. This is demonstrated in figure 46 where we show model spectra calculated as a function of the pump fluence following equation 5.3 with a single value of parameter D (figure 46a,c) and following equation (5.4) with a distribution of D values (figure 46b,d). For simplicity, the spectra were calculated using a Drude mobility (equation 2.18 with $\tau = 250\ fs$) and a Gaussian distribution function $f_G(D)$ with the effective parameters related to our sample (fitting parameters in figure 48).

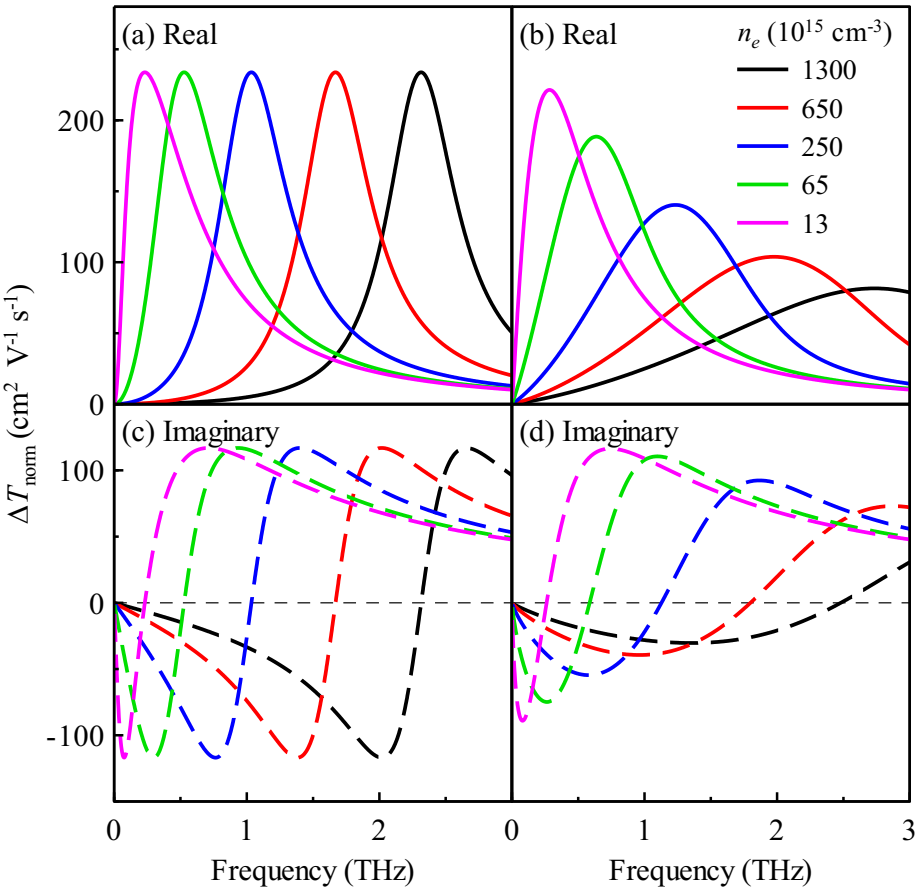

Figure 46. Examples of calculated model spectra of ΔT_{norm} as a function of the carrier concentration. The spectra are based on (a,c) the VBD model (equation 5.3) with a single value of the parameter D. (b,d) a model with the Gaussian distribution of morphological properties (equation 5.4). For simplicity we assumed in this illustration that the microscopic mobility $\mu(\omega)$ has the Drude behavior (equation 2.18).

5.2.2.1. Conductivity Peak at Weak Photoexcitation

It is important to emphasize that at 20 K, even at the lowest photoexcited carrier densities ($\phi = 5 \times 10^{-10}$ cm^{-2}, $n_e = 2.5 \times 10^{15}$ cm^{-3}, cyan curve in figure 45b,d), the frequency of the measured conductivity peak does not vanish, i.e., we still observe a clear deviation from the Drude-like behavior. However, under the low excitation conditions (and for negligible background doping of the nanobars), the depolarization field effects acting through the *D*-term in Equation (5.3) should be very small or even vanishing [68]; in other words, we expect that these experimental data should approach the true microscopic response $\mu(\omega)$ of the photocarriers.

In the case of the background doping (significant steady-state concentration of carriers) of the nanobars the peak in the transient response could a signature of a plasmon formed due to the cumulative effect of photocarriers and background charge carriers leading to an effective blue shift of the peak in $\mu(\omega)$.[121] A discussion of the influence of strong background doping on the photoconductivity spectra was also carried out in the case of InP nanowires where an increased mean thermal velocity due to an elevated Fermi level was assumed to be responsible for an observed blue shift in the conductivity peak. [120] However, we ruled out these possibilities via van der Pauw conductivity and Hall measurements of the unpatterned GaAs film: the room-temperature measurements on the verge of the DC-sensitivity revealed electron type of the background sheet conductivity ($\approx 3 \times 10^{-10}$ Ω^{-1}) with a carrier density of $n_e^{\mathrm{dark}} \approx 10^{10}$ cm^{-3}, which is several orders of magnitude lower than the estimated density ($\gtrsim 10^{16}$ cm^{-3}) required to shift the plasmonic resonance to the experimentally observed position.

Furthermore, we observe just a very tiny shift of the resonance position (by 0.05 THz) between the spectra obtained for the two lowest excitation densities at $T = 20$ K (magenta and cyan plots in figure 45b,d), while the experimental photocarrier density changes 5 times. This very weak dependence of ΔT_{norm} on the pump fluence further confirms that the *D* term in the denominator of Equation (5.3) is negligible.

We thus conclusively attribute the behavior at very low pump fluence to the confinement of photocarriers inside the nanobars [84]: the observed spectra coincide (except for the amplitude scaling factor) with the microscopic mobility $\mu(\omega)$.

5.2.2.2. Quantum Mobility Evaluation

In order to evaluate $\mu(\omega)$ in the equation 5.4 we employed quantum-mechanical approach described in section 2.2.4. In the initial calculations of the mobility, we considered an infinitely deep potential with a flat bottom as shown in figure 47a,b and with the nanobar width of 450 nm determined from the SEM images (figure 41d). However, this approach provides mobility spectra with the resonance at a significantly lower frequency than the observed one (figure 48b and inset of 48d).

Our explanation of the observed phenomenon is based on an increased confinement of charge carriers due to the band bending at GaAs surface [122] which may originate from surface defects (trapped electrons, strain relaxation) related to the preparation procedure, and the surface states associated with the lattice truncation. It was also previously observed that the

band bending in GaAs films grown on GaAlAs layer or AlAs/GaAsAs superlattices may extend over a few hundreds of nanometers [114].

In our quantum mechanical model, we accounted for the enhanced confinement effect by considering an additional parabolic potential inside the nanobar (figure 47c,d).The potential shape is thus assumed in the form $m^*\omega_0^2 x^2/2$, where the eigenfrequency ω_0 becomes an additional fitting parameter (m^* is the effective mass of electrons).

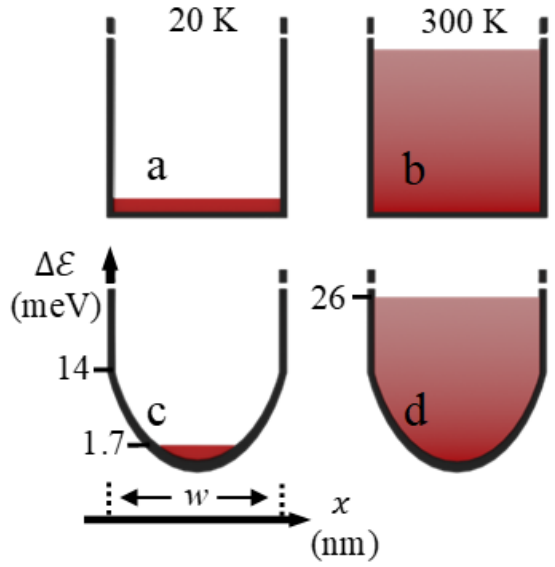

Figure 47. Scheme of the potential across the nanobars (potential wells). (a,b) Potential well with a flat bottom: the effective localization length would be independent of the temperature. (c) Potential well with parabolic bottom at low temperature: band bending concentrates the charges in a volume smaller than the one given by the geometrical width; the response is controlled by the curvature of the potential rather than by the geometrical width of the nanobar. (d) Potential well with parabolic bottom at an elevated temperature: charges gain an extra (thermal) kinetic energy and their confinement is again mostly determined by the geometrical width of the nanobar.

It is interesting to note that the parabolic nature of the confinement has no visible influence on the calculated mobility spectra at 300 K (the curves in figure 48a are undistinguishable from each other). From the fitted value of the eigenfrequency of the potential $\omega_0/2\pi \approx 0.33$ THz, we can evaluate the depth of the parabola, $\Delta\mathcal{E} = m^*\omega_0^2\, w^2/8 \approx 14$ meV ($w = 450$ nm is the nanobar width). Since the electrons at room temperature have a higher kinetic energy ($k_B T = 26$ meV), they can move over the full extent of the potential well and their motion is limited mainly by the physical size of the nanobar (figure 47d). At low temperature, the small thermal energy of electrons ($k_B T = 1.7$ meV) prevents them from reaching the surface of the nanobar; instead, they rapidly thermalize into the center of the nanobar and their response is controlled by the corresponding potential curvature (figure 47c). The electrons at low temperature are thus localized on distances of about 160 nm, quite far from the surface.

The real profile of the band bending likely differs from the very simple parabolic well. However, we verified that the peak frequency in the THz conductivity spectrum is controlled mainly by the extent of the region where the potential is smaller than approximately $k_B T$ and the exact shape of the potential has a little influence on the shape of the spectrum. The localization length of 160 nm at low temperature is thus a reliable number insensitive to the model chosen, while the value for the depth $\Delta\mathcal{E}$ constitutes an order of magnitude estimate.

5.2.2.3. Fitting Model

In order to account for the observed imperfections of the investigated sample, we assumed a Gaussian distribution of the D factors,

$$f_{\mathrm{G}}(D) = \frac{1}{\delta\sqrt{2\pi}} \exp\left(-\frac{(D - D_0)^2}{2\delta^2}\right), \tag{5.5}$$

where the parameters δ and D_0 are the standard deviation and the mean of the distribution. The fitting model for ΔT_{norm} based on equation 5.4 is thus completed; the fitting strategy involves a simultaneous fit of complex ΔT_{norm} spectra measured at 20 and 300 K and at several excitation powers (11 complex curves in total). This allows us to keep the number of unknown (adjustable) parameters at the very minimum: two parameters represent the electron scattering times τ at 20 and 300 K, four parameters represent effective medium coefficients (V, B, D_0, and δ) and, in addition, we consider the potential eigenfrequency ω_0.

Note that the room temperature spectra exhibit a small non-zero conductivity contribution at low frequencies (figure 48c), implying small contribution of the long-range carrier transport. Since the substrate is insulating, this can be explained only by a certain degree of electrical connectivity among the nanobars; such connections are in principle possible in more disordered areas of slid nanobars. At the same time, no sign of long-range transport was observed at 20 K (the photoconductivity drops to zero at low frequencies). These phenomena are encoded in the (fitting) parameter V which expresses the fraction of the structure percolated or close to the percolation. Since, at low temperature, the low-frequency photoconductivity drops to zero, $V = 0$ (no percolation is observed). Nevertheless, such a change of morphology with temperature is only minor, therefore the remaining effective medium parameters (B, δ, and D_0) are supposed to be temperature independent.

The percolation considerations are fully consistent with the evaluation of quantum-mechanical mobility in the previous section. At low temperatures, electrons are localized deeply inside the nanobars and therefore no long-range percolation may exist. At room temperature, due to the thermal excitation, electrons can fill some states at the nanobar surfaces, therefore their transport among nanobars may occur when the nanobars touch each other; this is represented by the non-zero V parameter.

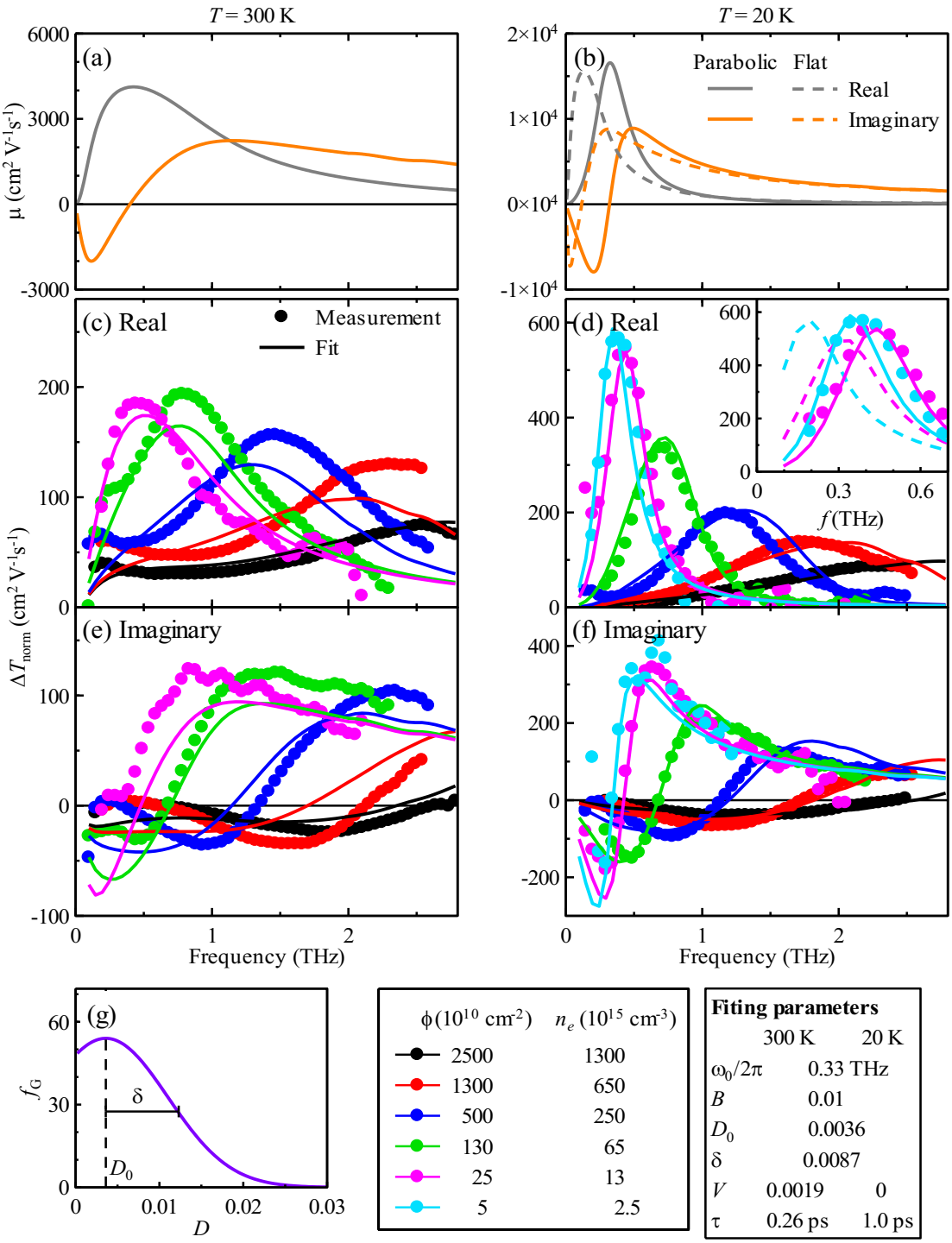

Figure 48. (a,b) Calculated microscopic mobility spectra μ of electrons in a flat and parabolic potential well. These spectra are undistinguishable in panel (a). (d–f) Normalized transient transmission ΔT_{norm} of the sample (symbols: measurements 10 ps after photoexitation; solid lines: calculations with the parabolic potential well. Inset: comparison of the fits of the lowest-carrier-concentration real conductivity spectra at 20 K for the two potentials: dashed lines: flat potential, solid line: parabolic confinement potential. (g) Gaussian distribution of the parameter D obtained from the fit. Inset: comparison of the fits of the real photoconductivity spectra at lowest carrier concentrations at 20 K for the two considered potentials: dashed lines: flat potential, solid line: parabolic confinement potential.

The fits of experimental data rely only on "global" parameters, which are independent of the pump fluence and the majority of them is also temperature independent. The fit values are summarized at the bottom of figure 48. The quality of the fits involving quantum calculations of the mobility in a parabolic potential well is excellent at 20 K and slightly worse but still quite reasonable at 300 K (figure 48). This difference may indicate that some additional thermally activated processes start to become effective at room temperature. We estimate that the error of the measured excitation fluence can reach 20%: this directly affects the amplitudes of individual spectra, but it can also lead to a shift in the peak positions (the peak position scales with $\sqrt{\phi}$ for moderate and high excitation fluences, therefore its frequency may easily differ by 10%). Finally, the Gaussian distribution of the D factor is likely to be just a rough approximation neglecting any fine details of the real structure.

5.2.2.4. Multi-THz Spectra

In order to further support the picture obtained from the THz spectroscopy, we extended the spectral range up to 8 THz by using time-resolved multi-THz spectroscopy (section 3.2). In our sample the multi-THz spectral range is limited by the transparency window of the Al_2O_3 substrate. The spectrum measured at 300 K and 10 ps after photoexcitation is shown in figure 49 along with the theoretical one. The theoretical spectrum was calculated using the fit parameter values obtained from the THz spectra as discussed in the previous paragraph. No adjustable coefficient was used. One can see a very good agreement in the amplitude and peak position between the measured and calculated data. Here we are left with just a single excitation fluence since the signal-to-noise ratio as well as the long-term stability of the setup is considerably worse than in the case of the conventional THz spectroscopy (acquisition of the presented spectrum took up to 25 hours to reach a sufficient signal-to-noise ratio).

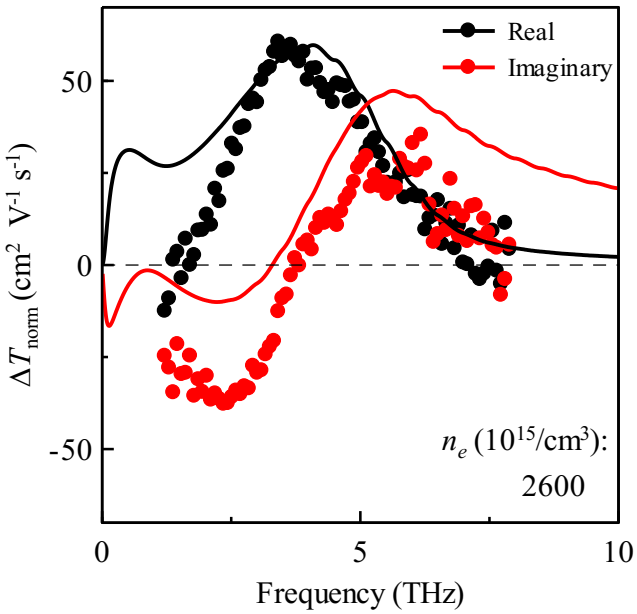

Figure 49. Real and imaginary parts of the normalized transient transmission spectrum ΔT_{norm} in the multi-THz spectral range. Symbols: measured data, lines: spectrum calculated using the fitting parameters obtained from the conventional THz spectroscopy (no additional degree of freedom).

5.2.3. THz Near-Field Investigations

So far, we have been examining the response of electrons in the lateral direction, averaged over a large ensemble of nanobars; the observed band bending thus applies to the vertical nanobar walls. However, despite certain possible differences in the character of the vertical walls (produced by etching) and top surface (formed upon the molecular beam epitaxy growth), one would expect that the band-bending effect should exist also in the normal direction to the sample surface. Despite the lack of experimental techniques that can directly measure the shape of the band potential in our structures, the presence of the band-banding effect has been confirmed in this study by means of the local THz measurement on THz-SNOM (section 3.4).

The tip of the THz-SNOM (section 3.4) was positioned in the lateral direction above the center of a nanobar, the THz sampling pulse timing was set to detect the field at the main maximum of the THz waveform. Second harmonic of the fundamental fiber laser output served for the photoexcitation of the sample at 780 nm. The measured THz SNOM signal with the pump beam blocked was identified with the zero-signal level. Subsequently, the pump beam was unblocked, and the pump-probe delay was scanned yielding an evolution of the average near-field THz response to the photoexcitation.

The optical pump – near-field THz probe dynamics are shown in figure 50. Here the THz-SNOM tip is sensing photocarriers in a single nanobar and the output signals obtained from the lock-in detection at different harmonics of the fundamental tip tapping frequency (ω_{tip}) represent the response of the carriers probed over different depths from the top surface of the nanobar. It is generally considered [123], and we show in more detail in the next section (5.2.3.1), that higher harmonics are more sensitive to the response in smaller depths. The kinetics in figure 50 thus indicate that carriers observed in a thinner layer close to the surface (sensed, e.g., by the 4$^{\mathrm{th}}$ harmonic) disappear significantly faster than those detected in a thicker surface layer (through the signal of the 1$^{\mathrm{st}}$ harmonic). Note also that there is no significant decay on the relevant time scale of the conductivity measured in far-field measurements, which represents the conductivity averaged over the entire thickness of the nanobar layer. This far-field measurement proves that the total carrier population is practically conserved up to several tens of picoseconds. The near-field results can thus be explained only by an ultrafast escape of the carriers from the top surface towards deeper parts. We observe a progressive and monotonous decrease of the signal decay time when passing from the first up to fourth harmonic, which means that the very top layer depopulates more rapidly than slightly deeper layers.

Analogous effect in the change of the speed of the pump-probe dynamics in InAs nanowires was observed by Eisele et al. in [124], where the probing depth was controlled via changes of the AFM tip tapping amplitude; the authors came to similar conclusions attributing the fast initial decay of the pump-induced resonance to formation of the depletion surface layer.

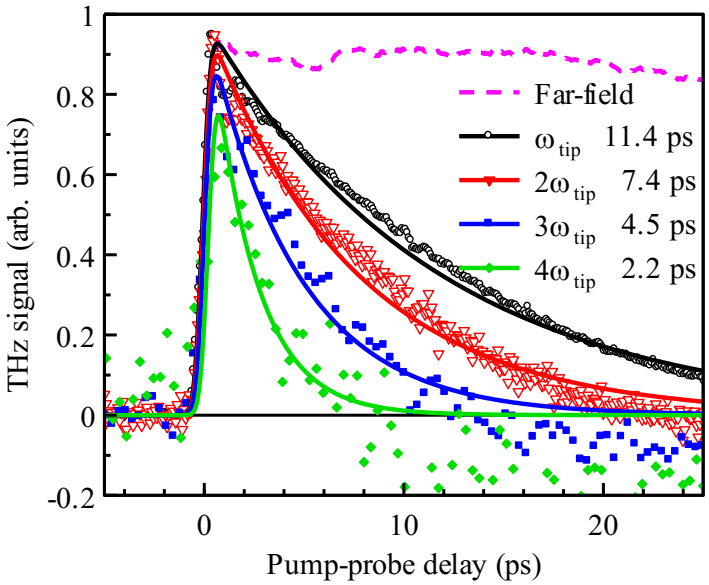

Figure 50. Dynamics of THz conductivity of photoexcited carriers observed at various harmonics of the tip vibration frequency in THz-SNOM. Symbols: experimental data, lines: fits by a single exponential function convoluted with a Gaussian instrumental response. The peak values of the bare exponential are normalized to unity. Dashed line: dynamics of the conductivity measured in the conventional far-field THz experiment. The fitted decay times as indicated in the legend.

We will now show that the observed decay times are compatible with the confinement due to the band bending deduced from the far-field measurements. Assuming the same parabolic potential $\Delta\mathcal{E}(z) = m\omega_0^2(z - L/2)^2/2$, the corresponding acceleration of electrons at the top of the nanobar is $a = \omega_0^2 L/2$ where $L = 700$ nm is the height of the nanobars and z is the distance from the top of the nanobar. The distance travelled by the electron during the mean scattering time τ is then $d = a\tau^2/2$ resulting in the mean travelling velocity $\langle v\rangle = d/\tau = \omega_0^2 L\tau/4$. For the scattering time $\tau = 260$ fs and $\omega_0/2\pi = 0.33$ THz deduced from the far-field experiments, we obtain $\langle v\rangle$~200 nm ps^{-1}. In the experiments, the smallest depth probed by the SNOM tip should be comparable to the tip diameter (~80 nm); combined with the decay time of 2.2 ps we arrive at a velocity ~ 40 nm ps^{-1}. This value itself is in a very good agreement with the theoretically estimated values (given the extreme simplicity of the model). Furthermore, we expect that the decay time of the 4th harmonic is still not the ultimately shortest one, and therefore the velocity is in reality higher than 40 nm ps^{-1}. The SNOM measurements thus strongly support the hypothesis that band-bending plays a crucial role in the dynamics and response of electrons in nanostructures.

5.2.3.1. Depth-dependence of the SNOM signal

This problem was deeply discussed within our group. Below, I provide a simple model proposed by H. Němec.

We assume that the part of the collected signal $S(b, z)$ scattered due to the presence of the SNOM tip and coming from the depth z below the sample surface, depends on the surface-

tip distance b which is modulated at angular frequency ω_{tip}, $b = b_0 + \Delta b \sin \omega_{\text{tip}} t$ (figure 51).This signal is thus described by the function

$$S(b, z) = S\big(b_0 + \Delta b \sin \omega_{\text{tip}} t\,, z\big). \tag{5.6}$$

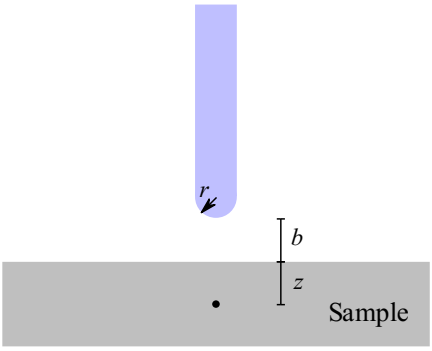

Figure 51. Scheme of the SNOM geometry.

This function is periodic in time, therefore it can be expanded into the harmonic series

$$S(z) = s_0(z) + \sum_{k=1,3,5,\ldots}^{\infty} s_k(z)\sin(k\omega_{\text{tip}} t) + \sum_{k=2,4,6,\ldots}^{\infty} s_k(z)\cos\big(k\omega_{\text{tip}} t\big)\,. \tag{5.7}$$

It should be stressed that the expansion coefficients s_k depend on the depth z from which the contribution to the signal originates. In fact, it is this dependence that is responsible for the different depth sensitivity of different collected harmonics. To quantify this behavior further, we evaluate the mean depth probed by the k-th harmonics expressed as

$$\langle z \rangle_k = \frac{\int_0^\infty z s_k(z) dz}{\int_0^\infty s_k(z) dz}. \tag{5.8}$$

The tip acts roughly as a dipolar source; we will assume the simplest behavior, for which the near field decreases with the third power of the distance. The interaction function is then proportional to

$$S(b, z) \propto \frac{1}{(z + b)^3}. \tag{5.9}$$

With this particular function, we illustrate in figure 52a that the higher is the demodulation harmonic, the faster the signal $s_k(z)$ decays with the depth z. This validates the statement that higher harmonics are more sensitive to processes in shallower depths. This is also reflected in the mean probe depth, which, following equation 5.8, decreases with the order of the harmonic (figure 52b). Within the presented model, we observe that the mean probed depth is of the order of the minimum tip-sample distance, $b_0 - \Delta b$. In practice, the tip is almost in contact with the sample and therefore the mean characteristic probed depth would be comparable rather with the tip radius.

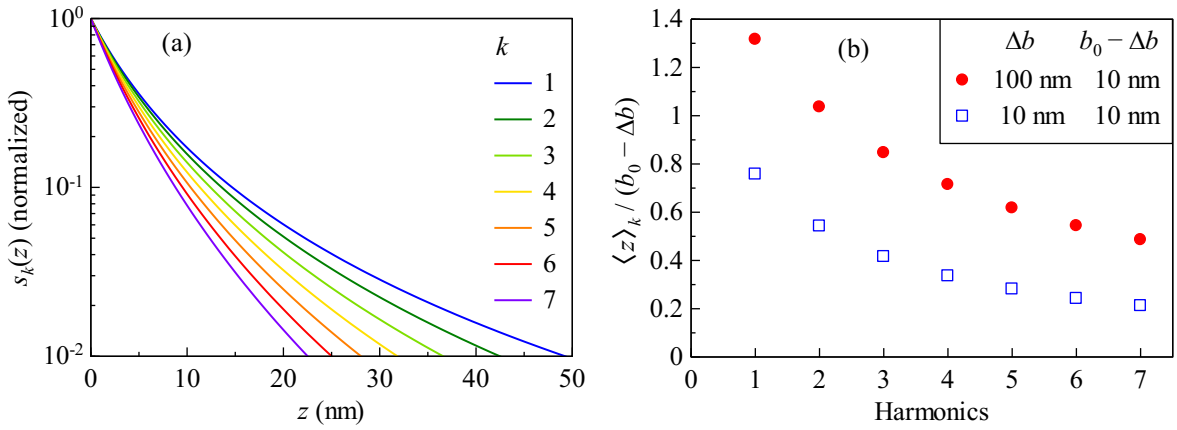

Figure 52. (a) Depth dependence of the scattered signal collected at k^{th} harmonic (curves are normalized to 1). (b) The mean probe depth $\langle z \rangle$ normalized by the minimum tip-surface distance $(b_0 - \Delta b)$ for a few lowest harmonics.

For a more detailed understanding of this behavior on the analytical level, we expand (S1) into the Taylor series with respect to the variable b:

$$S(b,z) = S(b_0,z) + \sum_{n=1}^{\infty} \frac{\left(\Delta b \sin \omega_{\text{tip}} t\right)^n}{n!} \frac{d^n S(b,z)}{db^n}\bigg|_{b=b_0}. \tag{5.10}$$

Using the binomial theorem for the expansion of sine function, we can easily find the coefficients $s_k(z)$; for example, for the coefficients of the cosine expansion we obtain

$$s_{2k}(z) = (-1)^k \sum_{n=k}^{\infty} \frac{\Delta b^{2n}}{2^{2n-1}(n-k)!\,(n+k)!} \frac{d^{2n} S(b,z)}{db^{2n}}\bigg|_{b=b_0}. \tag{5.11}$$

This expression has several important implications. Firstly, the signal on the k^{th} harmonics is controlled only by derivatives of the order of $2k$ and higher of the function S. This means that the higher is the detected harmonic, the subtler nuances of the particular form of the interaction function will control the detected signal. A more advanced debate will thus be needed in the future to link quantitatively the order of the harmonics and the characteristic probed depth of the sample.

5.3. Conclusion

Photoconductivity in an array of high-quality single-crystalline GaAs nanobars was measured by time-resolved terahertz spectroscopy at 300 and 20 K. For both temperatures, the spectra are dominated by a plasmonic resonance which blue-shifts with the excitation fluence over the entire THz range, thus reflecting the non-percolated nature of the array of the nanobars. Quantum mechanical calculations revealed that at low temperature, electrons are localized on distances smaller than the geometrical size of the nanobars; this behavior was attributed to the band bending due to surface states. While band bending is smaller than the thermal electron

energy at room temperature and therefore it has no significant effect on the photoconductive response, it still leads to a depopulation of the top layer of the nanobars on the picosecond time scale as evidenced by scanning near-field terahertz microscopy. The presented results thus demonstrate that band bending may have a prominent effect on the charge transport: both on the response function and dynamics of electrons. Essential ingredients for revealing such effects and understanding them quantitatively are well defined nanostructures, comparative measurements at high and low temperatures and for a large range of carrier concentrations, and a support by near-field spectroscopic techniques.

Conclusion

The main theme of this work was an in-depth analysis of the electron confinement effects from ultrafast THz photoconductivity spectra of inhomogeneous nanostructured materials. Relevant physical properties of nanomaterials (such as size, shape and connectivity of nanocrystals or, e.g., the defect concentration) frequently exhibit a significant variation from nanocrystal to nanocrystal. This rises a significant challenge for detailed studies of local charge carrier properties: the interpretation based on microscopic models is often not straightforward. In order to probe the conductivity resonances in nanostructures of various shapes and sizes at controlled (and varied) carrier concentrations, I have performed a number of time-resolved THz experiments extended to far- and mid-infrared range (Multi-THz and Multi-THz – mid-infrared pulsed spectroscopies described in chapter 3). In addition, near-field THz measurements were employed providing a valuable insight into local carrier properties.

The VBD effective medium model (section 2.2.6) was chosen as the basis for disentangling the phenomena due to depolarization fields in photoexcited nanoparticles and due to carrier localization (i.e., single carrier mobility). There is no doubt that significant advances in evaluating the mobility of confined electrons were made due to development of the quantum model of the THz conductivity (section 2.2.4). The model has been successfully introduced to the analysis of my original experimental results; it complemented far-field and near-field experimental results to prove the enhanced confinement of electrons due to band bending in GaAs nanobars.

The original part of this work consists of two investigations:

1. THz photoconductivity in networks of Si nanocrystals in SiO_2 matrix prepared by thermal decomposition in a superlattice geometry was studied at 300 and 20 K. The sample preparation technique aims towards fine control of NC size in quasi-two-dimensional layers, which was confirmed by electron microscopy. However, THz measurements revealed the presence of relatively large photoconductive objects compared to the picture suggested by TEM images (~ 4.5 nm). The result can be explained by clustering of the small NCs during crystallization process and such clusters dominantly contribute to the THz conductivity. A careful analysis of the measured spectra within the framework of the quantum electron confinement provided their size distribution that varies with Si content in the samples.

   Photoconductivity of the samples was subsequently probed via Multi-THz – mid-Infrared pulsed spectroscopy that confirmed a presence of the target 4-5 nm sized NCs (which are more numerous in number but not necessarily in volume) besides larger aggregates observed by the THz measurements. Note that many spectral fingerprints (mobility of confined electrons, plasmon resonances, optical interferences in the multilayer, and phonons in various SiO_2 components) mix in the broad experimental frequency range and our advanced analysis allowed to identify them. We also determined the ratio between the

numbers of small and large nanocrystals providing complementary information to TEM images. We also showed that the distribution of nanocrystal sizes in the samples inevitably decreases the degree of accuracy of the electron mobility determination.

2. THz photoconductivity in an array of ultimate-quality single crystalline GaAs nanobars was measured at 300 and 20 K. The structures were prepared via electron-beam lithography performed on a molecular-beam-epitaxy-grown GaAs layer transferred onto a sapphire substrate. A careful analysis of the THz spectra based on the quantum mechanical calculations revealed that at low temperature the electron confinement length is smaller than the physical dimension of the nanobars. We attribute the origin of this phenomenon to electronic states at the nanobar surface resulting in band bending. This has been supported by means of time-resolved scanning near-field terahertz microscopy that detected depopulation of the top layer of the nanostructures on the picosecond time scale.

An important conclusion of my original investigations is that although modern sample deposition techniques are able to provide certain control of nanostructure geometry, in some cases it may not be sufficient to resolve pertinent electronic properties of charge carriers in a single nanostructure. In order to quantitatively evaluate these properties with great accuracy, well defined nanostructures are really required.

We have proven that THz spectroscopy is a powerful tool for the contactless probing of the electron confinement in semiconductor nanostructures. Furthermore, I think that it is fair to say that our effective medium model combined with the cutting-edge quantum calculations represents a state-of-the-art analysis of charge carrier transport in inhomogeneous materials.

In regard to my personal contribution to this work, I would highlight the following:

- Experimental measurements of all the original spectra presented in the study except optical absorbance measurements used in section 4.1 (figure 23).
- Participation in all the microscopic measurements of the GaAs nanobars presented in section 5.1.2 (figure 41).
- Calculation of the analytical solution of the wave equation for the transient reflection function ΔR in the general case of effective sample response (described by VBD model) and for the specific photoconductivity profile (section 2.3.2).
- Fitting and interpretation of the experimental spectra using the VBD model developed in our group and generalizing the model by introducing integration over specific parameters.
- Participation in the preparation of the GaAs sample, namely in transfer of the GaAs film onto the sapphire substrate.

Bibliography

[1] V. Skoromets, H. Němec, J. Kopeček, and P. Kužel, K. Peters, D. Fattakhova-Rohlfing, A. Vetushka, M. Müller, K. Ganzerová, and A. Fejfar, J. Phys. Chem. C, 119, pp. 19485−19495 (2015).

[2] H. Němec, V. Zajac, I. Rychetský, D. Fattakhova-Rohlfing, B. Mandlmeier, T. Bein, Z. Mics, and P. Kužel, IEEE Trans. Terahertz Sci. Technol., 3, 302 (2013).

[3] M. Zacharias, J. Heitmann, R. Scholz, U. Kahler, M. Schmidt and J. Bläsing, Appl. Phys. Lett., 80, pp. 661-663 (2002).

[4] V. Pushkarev, T. Ostatnický, H. Němec, T. Chlouba, F. Trojánek, P. Malý, M. Zacharias, S. Gutsch, D. Hiller, and P. Kužel, Phys. Rev. B, 95, 125424 (2017).

[5] V. Pushkarev, H. Němec, V. C. Paingad, J. Maňák, V. Jurka, V. Novák, T. Ostatnický, and P. Kužel, Adv. Funct. Mater., 32, 2107403 (2022).

[6] J. Braine and D.H. Hughes, Astron. Astrophys., 344, 779 (1999).

[7] C. Kulesa, IEEE Transactions on Terahertz Science and Technology, 1, pp. 232-240 (2011).

[8] J. C. Pearson, B. J. Drouin, K. B. Cooper, and R. A. Stachnik, 20th International Symposium on Space Terahertz Technology, Charlottesville, (2009).

[9] P. Hamm and J. Savolainen, J. Chem. Phys. 136, 094516 (2012).

[10] Y. Watanabe, K. Kawase, T. Ikari, H. Ito, Y. Ishikawa, H. Minamide, Optics Communications, 234, pp. 125-129 (2004).

[11] T. Löffler, K. Siebert, S. Czasch, T. Bauer and H. G. Roskos, Phys. Med. Biol. 47 pp. 3847–3852 (2002).

[12] R. M. Woodward, B. E. Cole, V. P. Wallace, R. J. Pye, D. D. Arnone, E. H. Linfield, and M. Pepper, Phys. Med. Biol. 47, pp. 3853-3863 (2002).

[13] S. Nakajima, H. Hoshina, M. Yamashita, C. Otani and N. Miyoshi, Appl. Phys. Lett. 90, 041102 (2007).

[14] H. Li, K. Zhang, Q. Zhou, W.Mao, P. Dong, F. Tian, Int J Clin Exp Med, 10, pp. 3766-3773 (2017).

[15] R. Ulbricht, E. Hendry, J. Shan, T. F. Heinz, M. Bonn, Rev. Mod. Phys., 83 (2011).

[16] J. Lloyd-Hughes, Tae-In Jeon, J Infrared Milli Terahz Waves, 33, pp. 871–925 (2012).

[17] J.-Y. Kim, B. J. Kang, Y.-M. Bahk, Y. S. Kim, J. Park, W. T. Kim, J. Rhie, S. Han, H. Jeon, C.-H. Park, F. Rotermund and D.-S. Kim, Sci. Rep., 6, 29103, (2016).

[18] Y.-M. Bahk, B. J. Kang, Y. S. Kim, J.-Y. Kim, W. T. Kim, T. Y. Kim, T. Kang, J. Rhie, S. Han, C.-H. Park, F. Rotermund and D.-S. Kim, Phys. Rev. Lett., 115, 125501 (2015).

[19] M. Schall, M. Walther, C. Winnewisser, H. Helm, and P. U. Jepsen, Terahertz Spectroscopy and Applications II edited by J. M. Chamberlain, 3828, pp. 220-227, (1999).

[20] E. Hendry, M. Koeberg, J. Pijpers, and M. Bonn, Phys. Rev. B., 75, 233202 (2007).

[21] J. J. H. Pijpers, R. Ulbricht, K. J. Tielrooij, A. Osherov, Y. Golan, C. Delerue, G. Allan and M. Bonn, Nature Physics, 5, pp. 811–814 (2009).

[22] R. A. Kaindl, D. Hägele, M. A. Carnahan, and D. S. Chemla, Lawrence Berkeley National Laboratory (LBNL-997E), (2012).

[23] T. Timusk, Phys. Rev. B., 13, pp. 3511-3514 (1976).

[24] H. Němec, V. Zajac, P. Kužel, P. Malý, S. Gutsch, D. Hiller, and M. Zacharias, Phys. Rev.B, 91, 195443 (2015).

[25] B. P. Clayman and R.F. Frindt, Solid State Commun., 9, pp. 1881-1884 (1971).

[26] A. V. Pronin, M. Dressel, A. Pimenov, and A. Loidl, Phys. Rev. B, 57, 14416, (1997).

[27] T. Hong, K. Choi, K. Ik Sim, T. Ha, B. C. Park, H. Yamamori, and J. H. Kim, J. Appl. Phys., 114, 243905 (2013).

[28] D. Nuzhnyy, J. Petzelt, S. Kamba, P. Kužel, C. Kadlec, V. Bovtun, M. Kempa, J. Schubert, C. M. Brooks, and D. G. Schlom, Appl. Phys. Lett., 95, 232902 (2009).

[29] S. Kojima and T. Mori, Ferroelectrics, 500, pp. 183–202 (2016).

[30] K. Fukunaga, THz Technology Applied to Cultural Heritage in Practice. Cultural Heritage Science (Springer), (2016).

[31] J. F. Federici, B. Schulkin, F. Huang, D. Gary, R. Barat, F. Oliveira and D. Zimdars, Semicond. Sci. Technol., 20, pp. 266-280 (2005).

[32] G. Kozlov and A. Volkov, Millimeter and Submillimeter Wave Spectroscopy of Solids edited by G. Grüner, (Springer), (1998).

[33] M. C. Nuss and J. Orenstein, Millimeter and Submillimeter Wave Spectroscopy of Solids edited by G. Grüner, (Springer), (1998).

[34] G. P. Williams, Review of Scientific Instruments, 73, pp. 1461-1463, (2002).

[35] G. P. Williams, IOP Publishing, 69, 301-326, (2006).

[36] J. Barros, C. Evain, L. Manceron, J.-B. Brubach, M.-A. Tordeux, P. Brunelle, L. Nadolski, A. Loulergue, M.-E. Couprie, S. Bielawski, C. Szwaj, and P. Roy, Review of Scientific Instruments, 84, 033102 (2013).

[37] S. A. Zvyagin, M. Ozerov, E. Čižmár, D. Kamenskyi, S. Zherlitsyn, T. Herrmannsdorfer, and J. Wosnitza, Rev. Sci. Instrum., 80, 073102 (2009).

[38] N. Vinokurov, J. Infrared Milli. Terahz. Waves, 32, pp. 1123–1143, (2011).

[39] J. Faist, F. Capasso, D. L. Sivco, C. Sirtori, A. L. Hutchinson, A. Y. Cho, Science, 264, pp. 553-556 (1994).

[40] R. Köhler, A. Tredicucci, F. Beltram, H. E. Beere, E. H. Linfield, A. G. Davies, D. A. Ritchie, R. C. Iotti and F. Rossi, Nature, 417, pp. 156-159 (2002).

[41] B. S. Williams, Nature photonics, 1, pp. 518-525 (2007).

[42] M. Bass, P. A. Franken, J. F. Ward, and G. Weinreich, Phys. Rev. Lett., 9, 446 (1962).

[43] D. H. Auston, Appl. Phys. Lett., 43, (1983).

[44] D. H. Auston, K. P. Cheung, J. A. Valdmanis, and D. A. Kleinman, Phys. Rev. Lett., 53, (1984).

[45] D. H. Auston, Appl. Phys. Lett., 26, pp. 101-103 (1975).

[46] G. Mourou, C. V. Stancampiano, A. Antonetti, and A. Orszag, Appl. Phys. Lett., 39, pp. 295-296 (1981).

[47] D. H. Auston, and P. R. Smith, Appl. Phys. Lett., 43, 631-633 (1983).

[48] N. M. Burford and M. O. El-Shenawee, Optical Engineering, 56, 010901 (2017).

[49] A. Nahata, D. H. Auston, T. F. Heinz, and C. Wu, Appl. Phys. Lett., 68, pp. 150-152 (1996).

[50] C. Winnewisser, P. U. Jepsen, M. Schall, V. Schyja, and H. Helm, Appl. Phys. Lett., 70, pp. 3069-3071 (1997).

[51] D. Grischkowsky, Søren Keiding, Martin van Exter, and Ch. Fattinger, J. Opt. Soc. Am. B, 7(10), pp. 2006-2015 (1990).

[52] N. Katzenellenbogen and D. Grischkowsky, Appl. Phys. Lett., 61, pp. 840-842 (1992).

[53] P. Kužel and J. Petzelt, Ferroelectrics, 239, pp. 79-86 (2000).

[54] R. A. Kaindl, M. A. Carnahan, J. Orenstein, and D. S. Chemla, Phys. Rev. Lett., 88, 027003 (2002).

[55] C. Kadlec, F. Kadlec, H. Němec, P. Kužel, J. Schubert and G. Panaitov, J. Phys.: Condens. Matter, 21, 115902 (2009).

[56] L. Fekete, P. Kužel, H. Němec, F. Kadlec, A. Dejneka, J. Stuchlík, and A. Fejfar, Phys. Rev. B, 79, 115306 (2009).

[57] M. C. Beard, G. M. Turner, and C. A. Schmuttenmaer, Nano Lett., 2, pp. 983-987 (2002).

[58] P. Parkinson, J. Lloyd-Hughes, Q. Gao, H. H. Tan, C. Jagadish, M. B. Johnston, and L. M. Herz, Nano Lett., 7, pp. 2162-2165 (2007).

[59] H. Němec, F. Kadlec, and P. Kužel, J. Chem. Phys., 117, pp. 8454-8466 (2002).

[60] P. Kužel, F. Kadlec, and H. Němec, J. Chem. Phys., 127, 024506 (2007).

[61] D. J. Cook and R. M. Hochstrasser, Optical Letters, 25, pp. 1210-1212, (2000).

[62] M. D. Thomson, M. Kreß, T. Loffler, and H. G. Roskos, Laser & Photon. Rev., 1, pp. 349-368 (2007).

[63] K. Y. Kim, J. H. Glownia, A. J. Taylor and G. Rodriguez, Optics Express, 15, pp. 4577-4584 (2007).

[64] N. Karpowicz, J. Dai, X. Lu, Y. Chen, M. Yamaguchi, H. Zhao, X.-C. Zhang, L. hang, C. Zhang, M. Price-Gallagher, C. Fletcher, O. Mamer, A. Lesimple, and K. Johnson, Appl. Phys. Lett., 92, 011131 (2008).

[65] X. Lu and X.-C. Zhang, Front. Optoelectron., 7, 121–155 (2014).

[66] M. D. Thomson, V. Blank and H. G. Roskos, Optic Express, 18, 23176 (2010).

[67] V. Blank, M. D. Thomson and H. G. Roskos, New journal of Physic, 15, 075023 (2013).

[68] P. Kužel and H. Němec, J. Phys. D: Appl. Phys., 47, 374005 (2014).

[69] F. D'Angelo, H. Němec, S. H. Parekh, P. Kužel, M. Bonn, and D. Turchinovich, Optics Express, 24, pp. 10157-10171 (2016).

[70] P. Drude, Annalen Der Physik, 306, pp. 566–613 (1900).

[71] P. Drude, Annalen Der Physik, 308, pp. 369–402 (1900).

[72] M. C. Beard, G. M. Turner, and C. A. Schmuttenmaer, Phys. Rev. B, 62, pp. 15764-15777 (2000).

[73] H. Němec, L. Fekete, F. Kadlec, P. Kužel, M. Martin, J. Mangeney, J. C. Delagnes, and P. Mounaix, Phys. Rev. B, 78, 235206 (2008).

[74] J. C. Delagnes, P. Mounaix, H. Němec, L. Fekete, F. Kadlec, P Kužel, M. Martin, and J. Mangeney, J. Phys. D: Appl. Phys., 42, 195103 (2009).

[75] S. Glasstone, K. Laidler, and H. Eyring, McGraw-Hill, New York, 611 (1941).

[76] J. C. Dyre, J. Appl. Phys. 64, pp. 2456 -2468 (1988).

[77] N. V. Smith, Phys. Lett. A, 26, pp. 126-127 (1968).

[78] N. V. Smith, Phys. Rev. B, 64, 155106 (2001).

[79] C.-S. Yang, C.-M. Chang, P.-H. Chen, P. Yu, and C.-L. Pan, Optics Express, 21, pp. 16670-16682 (2013).

[80] D. G. Cooke, A. N. MacDonald, A. Hryciw, J. Wang, Q. Li, A. Meldrum, and F. A. Hegmann, Phys. Rev. B., 73, 193311 (2006).

[81] H. Ahn, Y.-P. Ku, Y.-C. Wang, C.-H. Chuang, S. Gwo, and Ci-Ling Pan, Appl. Phys. Lett., 91, 163105 (2007).

[82] M. C. Beard, G. M. Turner, J. E. Murphy, O. I. Micic, M. C. Hanna, A. J. Nozik, and C. A. Schmuttenmaer, Nano Lett., 3, pp. 1695-1699 (2003).

[83] S. A. Jensen, Ro. Ulbricht, A. Narita, X. Feng, K. Müllen, T. Hertel, Dmitry Turchinovich, and M. Bonn, Nano Lett., 13, pp. 5925−5930 (2013).

[84] H. Němec, P. Kužel, and V. Sundström, Phys. Rev. B, 79, 115309 (2009).

[85] T. Ostatnický, V. Pushkarev, H. Němec and P. Kužel, Phys. Rev. B, 97, 085426 (2018).

[86] H-K. Nienhuis and V. Sundström, Appl. Phys. Lett., 87, pp. 012101 (2005).

[87] J. C. M. Garnett, Philos. Trans. R. Soc. Lond. Ser. A, Contain. Pap. Math. Phys. Character., 203, 385 (1904).

[88] J. C. M. Garnett, Philos. Trans. R. Soc. Lond. Ser. A, Contain. Pap. Math. Phys. Character, 205, 237 (1906).

[89] D. a. G. Bruggeman, Ann. Phys., 416, 665 (1935).

[90] D. J. Bergman, D. Stroud, in Solid State Physics, 46 (Eds: H. Ehrenreich, D. Turnbull), pp. 147–269 (1992).

[91] M. Abramowitz and I. A. Stegun, Handbook of Mathematical Functions with Formulas, Graphs and Mathematical Tables, pp. 556-566 (1972).

[92] L. Pavesi, and R. Turan, Silicon nanocrystals. Fundamentals, synthesis and applications, Wiley-VCH, Wienheim (2010).

[93] J. Bisquert, Nanostructured Energy Devices: Equilibrium Concepts and Kinetics, CRC Press, Taylor & Francis (2015).

[94] N. Koshida, Device Applications of Silicon Nanocrystals and Nanostructures, Springer Science+Business Media, New York (2009).

[95] A. Jane, R. Dronov, A. Hodges, and N. H. Voelcker, Trends Biotechnol., 27, 230 (2009).

[96] D. G. Cooke, A. N. MacDonald, A. Hryciw, A. Meldrum, J. Wang, Q. Li, and F. A. Hegmann, J. Mater. Sci.: Mater. Electron., 18, pp. 447-425 (2007).

[97] L. V. Titova, T. L. Cocker, D. G. Cooke, X. Wang, A. Meldrum, and F. A. Hegmann, Phys. Rev. B, 83, 085403 (2011).

[98] A. M. Hartel, D. Hiller, S. Gutsch, P. Löper, S. Estradé, F. Peiró, B. Garrido, and M. Zacharias, Thin Solid Films, 520, pp. 121-125 (2011).

[99] S. Gutsch, D. Hiller, J. Laube, M. Zacharias, and C. Kübel, Beilstein J. Nanotechnol., 6, pp. 964-970 (2015).

[100] J. Laube, S. Gutsch, D. Hiller, M. Bruns, C. Kübel, C. Weiss, and M. Zacharias, J. Appl. Phys., 116, 223501 (2014).

[101] J. Laube, S. Gutsch, D. Wang, C. Kübel, M. Zacharias, and D. Hiller, Appl. Phys. Lett., 108, 043106 (2016).

[102] M. A. Green and M. J. Keevers, Prog. Photovolt: Res. Appl., 3, 189 (1995).

[103] V. Zajac, H. Němec, C. Kadlec, K. Kůsová, I. Pelant, P. Kužel, New J. Phys., 16, 093013 (2014).

[104] F. L. Pedrotti and L. S. Pedrotti, Introduction to Optics, 2nd ed. Prentice Hall, Englewood Cliffs, (1993).

[105] I. H. Malitson, Journal of the Optical Society of America, 55, pp. 1205-1209 (1965).

[106] Dargys A. and J. Kundrotas, Handbook on Physical Properties of Ge, Si, GaAs and InP, Science and Encyclopedia Publishers, (1994).

[107] T. Suzuki and R. Shimano, Phys. Rev. Lett., 103, 057401 (2009).

[108] P. Pikna, V. Skoromets, C. Becker, A. Fejfar, and P. Kuzel, Appl. Phys. Lett., 107, 233901 (2015).

[109] C. Jacoboni, C. Canali, G. Ottaviani, and A. A. Quaranta, Solid-State Electronics, 20, pp. 77-89, (1977).

[110] M. D. Thomson, W. Zouaghi, F. Meng, M. M. Wiecha, K. Rabia, T. Heinlein, L. Hussein, D. Babu, S. Yadav, J. Engstler, J. J. Schneider, N. Nicoloso, I. Rychetský, P. Kužel, and H. Roskos, J. Phys. D: Appl. Phys., 51, 034004 (2018).

[111] F. A. Johnson, Proc. Phys. Soc., 73**,** pp. 265-272 (1959).

[112] P. Y. Yu and M. Cardona, Fundamentals of Semiconductors, Springer, pp. 289–295 (1996).

[113] D. E. Aspnes and A. A. Studna, Phys. Rev. B, 27, pp. 985-1009 (1983).

[114] L. Nádvorník, P. Němec, T. Janda, K. Olejník, V. Novák, V. Skoromets, H. Němec, P. Kužel, F. Trojánek, T. Jungwirth, J. Wunderlich, Sci. Rep., 6, 22901 (2016).

[115] E. Yablonovitch, D. M. Hwang, T. J. Gmitter, L. T. Florez, J. P, Harbison, Appl. Phys. Lett., 56, 2419 (1990).

[116] M. Levinshtein, S. Rumyantsev, Handbook Series on Semiconductor Parameters (1996).

[117] J. S. Blakemore, J. Appl. Phys., 53, R123 (1982).

[118] G. E. Jellison Jr., Optical Materials, 1, pp. 151-160 (1992).

[119] X. Su, X. Zeng, H. Němec, X. Zou, W. Zhang, M. Borgström, A. Yartsev, Nanoscale, 11, 18550 (2019).

[120] C. S. Ponseca, Jr., H. Němec, J. Wallentin, N. Anttu, J. P. Beech, A. Iqbal, M. Borgström, M.-E. Pistol, L. Samuelson, A. Yartsev, Phys. Rev. B, 90, 085405 (2014).

[121] H. J. Joyce, C. J. Docherty, Q. Gao, H. H. Tan, C. Jagadish, J. Lloyd-Hughes, L. M. Herz, M. B. Johnston, Nanotechnology, 24, 214006 (2013).

[122] J. Lloyd-Hughes, S. K. E. Merchant, L. Sirbu, I. M. Tiginyanu, M. B. Johnston, Phys. Rev. B, 78, 085320 (2008).

[123] C. Maissen, S. Chen, E. Nikulina, A. Govyadinov, R. Hillenbrand, ACS Photonics, 6, pp. 1279-1288 (2019).

[124] M. Eisele, T. L. Cocker, M. A. Huber, M. Plankl, L. Viti, D. Ercolani, L. Sorba, M. S. Vitiello and R. Huber, Nature Photonics, 8, pp. 841-845 (2014).

List of Abbreviations

ABCD	air-biased coherent detection
AFM	atomic force microscope/y
BBO	barium borate
DC	direct current
DS	Drude-Smith *model*
EF-TEM	energy-filtered transmission electron microscope/y
EMA	effective medium approximation
EMT	effective medium theory
FTIR	Fourier-transform infrared spectroscopy
LP	localized plasmon
MBE	molecular-beam epitaxy
MG	Maxwell-Garnett *effective medium theory*
NC	nanocrystal
OPMIP	optical pump – mid-infrared *spectroscopy, spectrum, method*
OPTP	optical pump – THz probe *spectroscopy, spectrum, method*
SEM	scanning electron microscope/y
SFG	sum-frequency generation
SNOM	scanning near-field optical microscope/y
TCE	trichloroethylene
TDS	time-domain spectroscopy
TEM	transmission electron microscope/y